

# CHAPTER 4

## Radar Waveforms

### 4.1 Introduction

A radar transmits a waveform typically modeled as

$$\bar{x}(t) = a(t) \sin[\Omega t + \theta(t)] \quad (4.1)$$

The term  $\Omega$  in the argument of the sine function is the carrier radar frequency (RF) in radians per second. The term  $a(t)$  represents amplitude modulation of the RF carrier; in a pulsed radar, this is typically just a rectangular function that pulses the waveform on and off. The term  $\theta(t)$  models any phase or frequency modulation of the carrier. It can be zero, a nonzero constant, or a nontrivial function. The overbar on  $\bar{x}(t)$  denotes that the signal is on a carrier, i.e., it has not yet been demodulated. Figure 4.1 illustrates three example waveform types common in pulsed radar. The simple pulse is simply a constant-amplitude burst at the RF frequency. The frequency of the *linear frequency modulated* (LFM) pulse increases at a constant rate during the time the pulse is on. LFM pulses can also have decreasing frequency during the pulse. The third example is a binary phase-coded pulse. In this waveform, the frequency is constant but the absolute phase of the waveform changes from zero to  $\pi$  radians several times within the pulse. That is, the value of  $\theta(t)$  changes between the constants zero and  $\pi$  at specific times within the pulse.

As discussed in Chap. 1, the real-valued waveform of Eq. (4.1) is more conveniently modeled by its complex equivalent

$$\bar{x}(t) = a(t) e^{j[\Omega t + \theta(t)]} \quad (4.2)$$

The portion of  $\bar{x}(t)$  other than the carrier term, or equivalently the complex baseband signal after demodulation, is called the *complex envelope* of the waveform

$$x(t) = a(t) e^{j\theta(t)} \quad (4.3)$$

It is this function that describes the amplitude and phase or frequency modulation applied to the RF carrier and is considered to be “the waveform” in this chapter.

Radar waveforms can be characterized in several ways. Perhaps first is whether the waveform is *continuous wave* (CW) or pulsed; sometimes variations such as “interrupted CW” are defined as well. Pulsed waveforms can be defined based on a single pulse, or “the waveform” can be considered to be a multipulse burst. Both pulsed and CW waveforms can be further categorized based on the presence or absence of frequency or phase modulation. If present, the modulation may be intrapulse (applied to individual pulses), interpulse (applied across the pulses of a multipulse waveform), or both. Phase modulation can be biphasic (two possible states) or polyphase (more than two phase states); frequency modulation can be linear or nonlinear. Intrapulse amplitude modulation may be used, but usually is not.

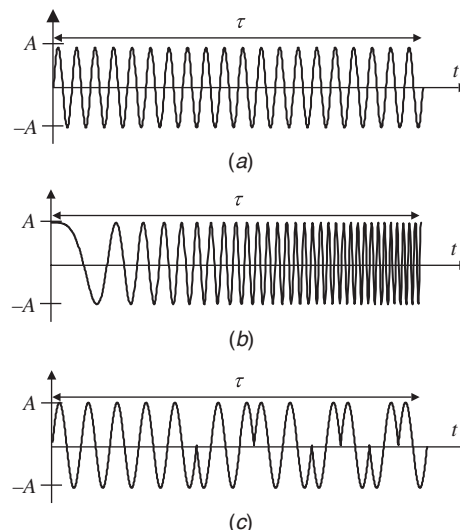


**FIGURE 4.1** Examples of common pulsed radar waveforms: (a) simple pulse, (b) linear frequency modulated (LFM) pulse, (c) binary phase-coded pulse.

The choice of waveform directly determines or is a major contributor to several fundamental radar system performance metrics. These include the *signal-to-noise ratio* (SNR)  $\chi$ , the range resolution  $\Delta R$ , the Doppler (velocity) resolution  $\Delta F_D$  ( $\Delta v$ ), ambiguities in range and Doppler, range and Doppler sidelobes, and range-Doppler coupling. These metrics are determined by such waveform attributes as the pulse duration, bandwidth, amplitude, and phase or frequency modulation. While all of these metrics are discussed, the primary emphasis is on SNR, range resolution, and Doppler resolution because these are the most fundamental drivers in choosing the waveform. As an example, the simple pulse of Fig. 4.1a has a duration of  $\tau$  seconds and an amplitude of  $A$  volts. The SNR will prove to be proportional to the waveform energy, which is the product  $A^2\tau$  of its power and duration. The range resolution of  $c\tau/2$  is proportional to the pulse duration. It will be shown shortly that both the waveform bandwidth and the Doppler resolution of the simple pulse are inversely proportional to the pulse length.

Two classic references on radar waveforms are Cook and Bernfeld (1993) and Rihaczek (1996). Most radar system books cover the fundamentals of radar waveforms (e.g., Nathanson, 1991; Peebles, 1998). A complete modern reference on radar waveforms is Levanon and Mozeson (2004), while good brief surveys of basic and advanced waveforms are in Keel (2010) and Keel and Baden (2012), respectively. In addition to covering the mainstream waveforms such as pulse bursts and LFM, this text covers the many developments in phase codes in recent decades. Another new text that focuses more on advanced waveforms and emerging applications is Gini et al. (2012).

## 4.2 The Waveform Matched Filter

### 4.2.1 The Matched Filter

So far, it has been implicitly assumed that the overall frequency response of the radar receiver is a bandpass characteristic with a bandwidth equal to or greater than that of the transmitted signal. Equivalently, once the carrier is demodulated out, the effective frequency response is

a lowpass filter with a bandwidth equal to that of the complex envelope. It will be shown in Chap. 6 that detection performance improves with increasing SNR. Thus, it is reasonable to ask what overall receiver frequency response  $H(\Omega)$  will maximize the SNR.

To answer this question, note that the spectrum of the receiver output,  $y(t)$ , will be  $Y(\Omega) = H(\Omega)X(\Omega)$ , where  $X(\Omega)$  is the spectrum of the waveform (and thus, except for a phase shift due to an overall delay, of a received target echo). Consider maximizing the SNR at a specific time  $T_M$ . The power of the signal component of the output at that instant is

$$|y(T_M)|^2 = \left| \frac{1}{2\pi} \int_{-\infty}^{\infty} X(\Omega)H(\Omega)e^{j\Omega T_M} d\Omega \right|^2 \quad (4.4)$$

To determine the output noise power, consider the case where the interference is white noise with power spectral density  $\sigma_w^2$  W/Hz. The noise power spectral density at the output of the receiver will be  $\sigma_w^2 |H(\Omega)|^2$  W/Hz. The total output noise power is then

$$n_p = \frac{\sigma_w^2}{2\pi} \int_{-\infty}^{\infty} |H(\Omega)|^2 d\Omega \quad (4.5)$$

and the SNR measured at time  $T_M$  is

$$\chi = \frac{|y(T_M)|^2}{n_p} = \frac{\left| (1/2\pi) \int_{-\infty}^{\infty} X(\Omega)H(\Omega)e^{j\Omega T_M} d\Omega \right|^2}{(\sigma_w^2/2\pi) \int_{-\infty}^{\infty} |H(\Omega)|^2 d\Omega} \quad (4.6)$$

Clearly,  $\chi$  depends on the receiver frequency response. The choice of  $H(\Omega)$  that will maximize  $\chi$  can be determined via the Schwarz inequality. One of many forms of the Schwarz inequality is

$$\left| \int A(\Omega)B(\Omega) d\Omega \right|^2 \leq \left\{ \int |A(\Omega)|^2 d\Omega \right\} \left\{ \int |B(\Omega)|^2 d\Omega \right\} \quad (4.7)$$

with equality if and only if  $B(\Omega) = \alpha A^*(\Omega)$ , with  $\alpha$  any arbitrary constant. Applying Eq. (4.7) to the numerator of Eq. (4.6) give the upper bound on SNR as

$$\chi \leq \frac{(1/2\pi)^2 \int_{-\infty}^{\infty} |X(\Omega)e^{j\Omega T_M}|^2 d\Omega \int_{-\infty}^{\infty} |H(\Omega)|^2 d\Omega}{(\sigma_w^2/2\pi) \int_{-\infty}^{\infty} |H(\Omega)|^2 d\Omega} \quad (4.8)$$

The SNR is maximized when

$$\begin{aligned} H(\Omega) &= \alpha X^*(\Omega) e^{-j\Omega T_M} \quad \text{or} \\ h(t) &= \alpha x^*(T_M - t) \end{aligned} \quad (4.9)$$

This particular choice of the receiver filter frequency or impulse response is called the *matched filter*, because the response is “matched” to the signal waveform. Thus, the waveform and the receiver filter needed to maximize the output SNR are a matched pair. If the radar changes waveforms, it must also change the receiver filter response in order to stay in a matched condition. The impulse response of the matched filter is obtained by time-reversing and conjugating the complex waveform. The gain constant  $\alpha$  is often set equal to unity; it has no impact on the achievable SNR, as seen later in this chapter. The time  $T_M$  at which the SNR is maximized is arbitrary. However,  $T_M \geq \tau$  is required for  $h(t)$  to be causal.

Given an input signal  $x'(t)$  consisting of both target and noise components, the output of the matched filter is given by the convolution

$$\begin{aligned} y(t) &= \int_{-\infty}^{\infty} x'(s)h(t-s)ds \\ &= \alpha \int_{-\infty}^{\infty} x'(s)x^*(s+T_M-t)ds \end{aligned} \quad (4.10)$$

The second line of Eq. (4.10) is recognized as the cross-correlation of the target-plus-noise signal  $x'(t)$  with the transmitted waveform  $x(t)$ , evaluated at lag  $T_M - t$ . Thus, the matched filter implements a correlator with the transmitted waveform as the reference signal.

It is useful to determine the maximum value of SNR achieved by the matched filter. Using  $H(\Omega) = \alpha X^*(\Omega) \exp(-j\Omega T_M)$  in Eq. (4.6)

$$\begin{aligned} \chi &= \frac{\left| (1/2\pi) \int_{-\infty}^{\infty} X(\Omega) [\alpha X^*(\Omega) e^{-j\Omega T_M}] e^{j\Omega T_M} d\Omega \right|^2}{(\sigma_w^2 / 2\pi) \int_{-\infty}^{\infty} |\alpha X^*(\Omega) e^{-j\Omega T_M}|^2 d\Omega} \\ &= \frac{\left| (1/2\pi) \alpha \int_{-\infty}^{\infty} |X(\Omega)|^2 d\Omega \right|^2}{|\alpha|^2 \sigma_w^2 / 2\pi \int_{-\infty}^{\infty} |X(\Omega)|^2 d\Omega} \\ &= \frac{1}{2\pi\sigma_w^2} \int_{-\infty}^{\infty} |X(\Omega)|^2 d\Omega \end{aligned} \quad (4.11)$$

The energy in the signal  $x(t)$  is

$$E = \int_{-\infty}^{\infty} |x(t)|^2 dt = \frac{1}{2\pi} \int_{-\infty}^{\infty} |X(\Omega)|^2 d\Omega \quad (4.12)$$

where the second step follows from Parseval's relation. Using Eq. (4.12) in Eq. (4.11) gives

$$\chi = \frac{1}{2\pi\sigma_w^2} \int_{-\infty}^{\infty} |X(\Omega)|^2 d\Omega = \frac{E}{\sigma_w^2} \quad (4.13)$$

Equation (4.13) states the remarkable result that the maximum achievable SNR depends only on the energy of the waveform and not on other details such as its modulation. Two waveforms having the same energy will produce the same maximum SNR, provided each is processed through its own matched filter.

Although it is the ratio of the peak signal component power to the noise power, the SNR of Eq. (4.13) is called the *energy SNR* because the peak signal power at the matched filter output equals the energy of the transmitted signal. To see this, note that the peak signal component at the matched filter output is given by Eq. (4.10) with  $t = T_M$

$$y(T_M) = \int x(s) \alpha x^*(s) ds = \alpha E \quad (4.14)$$

Also, the duration of the signal component of the matched filter output is exactly  $2\tau$  seconds, since it is the convolution of the  $\tau$ -second pulse with the  $\tau$ -second matched filter impulse response.

The previous results can be generalized to develop a filter that maximizes output *signal-to-interference ratio* (SIR) when the interference power spectrum is not white. In radar, this is

useful for example in cases where the dominant interference is clutter, which generally has a colored power spectrum. The result can be expressed as a two-stage filtering operation. The first stage is a *whitening filter* that converts the interference power spectrum to a flat spectrum (and also modifies the signal spectrum in the process); the second stage is then a conventional matched filter as described earlier, but designed for the now-modified signal spectrum. Details are given by Kay (1998).

#### 4.2.2 Matched Filter for the Simple Pulse

To illustrate the previous ideas, consider a simple pulse of duration  $\tau$ :

$$x(t) = \begin{cases} 1, & 0 \leq t \leq \tau \\ 0, & \text{otherwise} \end{cases} \quad (4.15)$$

The corresponding matched filter impulse response is

$$\begin{aligned} h(t) &= \alpha x^*(T_M - t) \\ &= \begin{cases} \alpha, & T_M - \tau \leq t \leq T_M \\ 0, & \text{otherwise} \end{cases} \end{aligned} \quad (4.16)$$

where  $T_M > \tau$  for causality. Because  $x(t)$  is a much simpler function than its Fourier transform (a sinc function), it is easier to work with the correlation interpretation of Eq. (4.10) to compute the output. Figure 4.2 illustrates the two terms in the integrand, helping to establish the regions of integration. Part *a* of the figure shows that

$$y(t) = \begin{cases} 0, & t < T_M - \tau \\ \int_0^{t-T_M+\tau} (1)(\alpha) ds, & T_M - \tau \leq t \leq T_M \end{cases} \quad (4.17)$$

while part *b* is useful in identifying the next two regions

$$y(t) = \begin{cases} \int_{t-T_M}^{\tau} (1)(\alpha) ds, & T_M \leq t \leq T_M + \tau \\ 0, & t > T_M + \tau \end{cases} \quad (4.18)$$

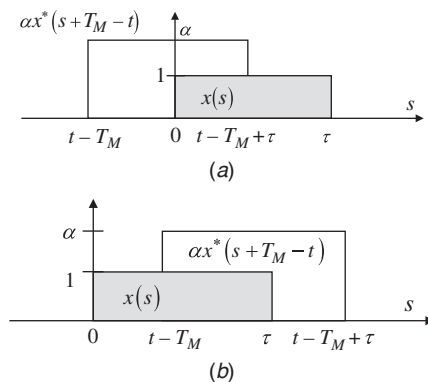


**FIGURE 4.2** Convolution of simple pulse and its matched filter: (a)  $T_M - \tau \leq t \leq T_M$ , (b)  $T_M \leq t \leq T_M + \tau$ .

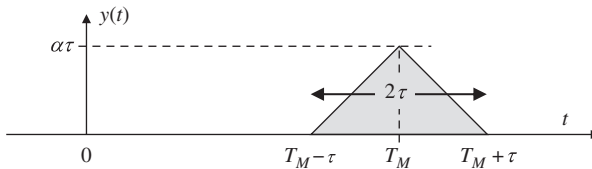


FIGURE 4.3 Matched filter output for a simple pulse.

The result is

$$y(t) = \begin{cases} \alpha[t - (T_M - \tau)], & T_M - \tau \leq t \leq T_M \\ \alpha[(T_M + \tau) - t], & T_M \leq t \leq T_M + \tau \\ 0, & \text{otherwise} \end{cases} \quad (4.19)$$

This result is illustrated in Fig. 4.3. The matched filter output is a triangle function of duration  $2\tau$  seconds with its peak at  $t = T_M$  as expected. The peak value is  $\alpha\tau$ ; since the energy of the unit amplitude pulse is just  $\tau$ , the peak value equals  $\alpha E$  as predicted.

The noise power at the output of the matched filter is

$$\begin{aligned} n_p &= \frac{\sigma_w^2}{2\pi} \int_{-\infty}^{\infty} |H(\Omega)|^2 d\Omega \\ &= \sigma_w^2 \int_{-\infty}^{\infty} |h(t)|^2 dt \quad (\text{Parseval's relation}) \\ &= \sigma_w^2 |\alpha|^2 \tau \end{aligned} \quad (4.20)$$

The SNR is therefore

$$\chi = \frac{|\alpha\tau|^2}{\sigma_w^2 |\alpha|^2 \tau} = \frac{\tau}{\sigma_w^2} = \frac{E}{\sigma_w^2} \quad (4.21)$$

consistent with Eq. (4.13). Note that the gain  $\alpha$  has no effect on the SNR.

### 4.2.3 All-Range Matched Filtering

The matched filter was designed to maximize the output SNR at a particular time instant  $T_M$ . This raises several questions. How should  $T_M$  be chosen, and how can the range of a target be related to the resulting output? What happens if the received signal contains echoes from multiple targets at different ranges?

Start by choosing  $T_M = \tau$ , the minimum value that results in a causal matched filter. Now suppose the input to the matched filter is the echo from a target at an unknown range  $R_0$ , corresponding to a time delay  $t_0 = 2R_0/c$ . The signal component of the output of the matched filter will be

$$y(t) = \int_{-\infty}^{\infty} x(s - t_0) \alpha x^*(s + \tau - t) ds \quad (4.22)$$

This is just the correlation of the received, delayed echo and the matched filter impulse response. The output waveform will again be a triangle with its peak at correlation lag zero.

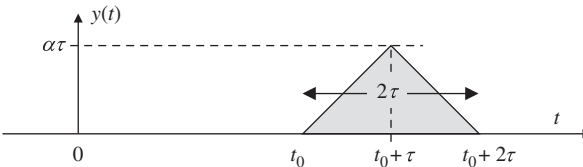


**FIGURE 4.4** Output of the matched filter for a target at range  $R_0 = ct_0/2$ .

This occurs when  $s - t_0 = s + \tau - t$ , or  $t = t_0 + \tau$ . The matched filter output will appear as in Fig. 4.4. The peak will occur at time  $t_{\text{peak}} = t_0 + \tau$ , corresponding to the actual delay to the target plus the delay of the causal matched filter. The target range can be easily determined from observation of the matched filter output as  $R_0 = c(t_{\text{peak}} - t)/2$ .

This discussion shows that the matched filter parameter  $T_M$  can be chosen arbitrarily (typically as  $T_M = \tau$ ). Once  $T_M$  is known, the range of a target can be determined by detecting the time at which a peak occurs at the matched filter output, subtracting  $T_M$  to get the delay to the target and back, and converting to units of range. Thus, a single choice of  $T_M$  allows detection of targets at all ranges. One simply samples the matched filter output at a series of fast-time sample instants  $t_k$ ; if a peak occurs at time  $t_k$ , it corresponds to a target at range  $c(t_k - T_M)/2$ . If the received signal contains echoes from multiple targets at different ranges, by superposition the matched filter output will contain multiple copies of the single-pulse triangle response, one centered at the time delay (plus filter delay) of each of the various targets.

#### 4.2.4 Straddle Loss

In modern practice, matched filtering is carried out digitally so that  $y(t)$  is sampled at some fast-time sampling rate  $F_s = 1/T_s$ . Typically  $F_s$  equals or is slightly greater than the waveform bandwidth  $\beta$ . The range sample spacing is then  $cT_s/2$  meters. In general, targets do not arrange themselves precisely at ranges corresponding to the range samples. The receiver then will not sample the matched filter output precisely at its peak. The result is a reduction in the measured signal amplitude and therefore an SNR loss.

This is exactly the issue of straddle loss that was discussed in Chap. 3 with regard to the DFT of frequency domain data. In either case, the finite sampling rate allows the processor to “miss” the peak response, whether it is the matched filter output in fast time or the spectrum of a slow-time signal. Straddle loss also arises in angular sampling with scanning antennas. In any of these cases it can be reduced with higher sampling rates or various interpolation methods. Consideration of these methods is deferred to the discussion of pulse Doppler analysis in Chap. 5 and the analyses of time delay, frequency, and angle estimation in Chap. 7. All of the methods there can be applied to the fast-time straddle loss for the various waveforms in this chapter.

#### 4.2.5 Range Resolution of the Matched Filter

By determining the range separation that would result in nonoverlapping echoes, it was shown in Chap. 1 that the range resolution achieved by a simple pulse of duration  $\tau$  seconds is  $c\tau/2$  meters. When a matched filter is used, the output due to each scatterer is now  $2\tau$  seconds long, but is also triangular rather than rectangular in shape. Does the longer matched filter output result in a larger value of range resolution?

Before considering this question, it is useful to recall that the demodulated echo from a scatterer at range  $R_0$  meters has not only a delay of  $t_0 = 2R_0/c$  seconds, but also an

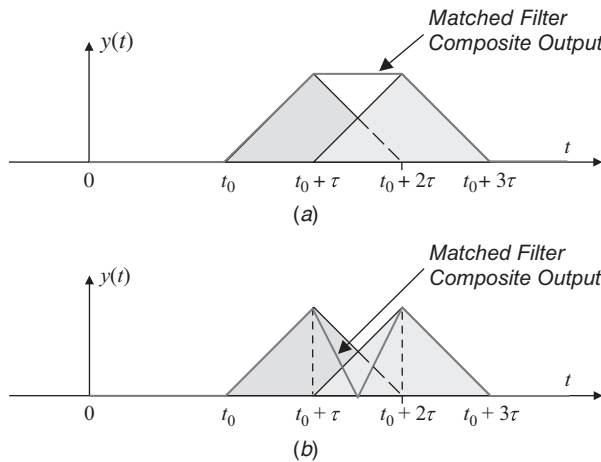


**FIGURE 4.5** Composite matched filter response due to two scatterers separated by  $c\tau/2$  meters: (a) target responses in phase, (b) target responses  $180^\circ$  out of phase.

overall phase shift of  $\exp[j(-4\pi/\lambda)R_0]$  radians.<sup>1</sup> A change of only  $\lambda/4$  in range will cause a change of  $180^\circ$  in the received echo phase. Two overlapping target responses may therefore add either constructively or destructively in phase, and small deviations in their spacing can result in large changes in the composite response. Consider two targets at ranges  $ct_0/2$  and  $ct_0/2 + c\tau/2$  and assume  $\tau$  is such that the two matched filter responses add in phase. Then the composite response at the matched filter output is a flat-topped trapezoid as shown in Fig. 4.5a. Clearly, if the separation between the two scatterers increases, a dip will begin to develop in the composite response, even when the separation is such that they remain in phase. If the separation decreases, the in-phase response will still be a trapezoid, but with a higher peak and a shorter flat region as the responses overlap more. Because any increase in separation will result in a dip between the two responses, the separation of  $c\tau/2$  meters is still considered to be the range resolution of the matched filter output. Thus, using a matched filter does not degrade the range resolution. To reinforce this further, recall that the definition of the Rayleigh resolution is the peak-to-first null distance. Inspection of Fig. 4.3 shows that  $c\tau/2$  is also the Rayleigh resolution of the simple pulse matched filter output.

Scatterers that are closer together than the Rayleigh resolution may still be resolved if the spacing is such that the individual responses add out of phase. Figure 4.5b illustrates the case where the two responses differ in phase by  $180^\circ$ . Destructive interference in the region of overlap causes a deep null in the composite response. However, this null is very sensitive to the fine spacing of the scatterers and cannot be relied on to resolve two targets.

### 4.3 Matched Filtering of Moving Targets

Suppose a simple pulse is transmitted,  $x(t) = 1$ ,  $0 \leq t \leq \tau$ , and it echoes from a target moving toward the radar with a radial velocity of  $v$  meters per second. After demodulation, the received waveform (ignoring the overall time delay) will be  $x'(t) = x(t)\exp(j\Omega_D t)$ , with  $\Omega_D = 4\pi v/\lambda$ .

<sup>1</sup>This phase shift term was absorbed into the effective reflectivity  $\rho'$  in Chap. 2.

Because the echo is different from  $x(t)$ , a filter matched to  $x(t)$  will *not* be matched to  $x'(t)$ . If the target velocity is known, the matched filter for  $x'(t)$  can be constructed:

$$h(t) = \alpha x'^*(-t) = \alpha x^*(-t)e^{+j\Omega_D t} \quad (4.23)$$

The frequency response of this matched filter is

$$\begin{aligned} H(\Omega) &= \alpha \int_{-\infty}^{\infty} x^*(-t)e^{+j\Omega_D t} e^{-j\Omega t} dt, \quad t' = -t \\ &= \alpha \left[ \int_{-\infty}^{\infty} x(t')e^{-j(\Omega - \Omega_D)t'} dt' \right]^* \\ &= \alpha X^*(\Omega - \Omega_D) \end{aligned} \quad (4.24)$$

Thus, the matched filter for  $x'(t)$  can be obtained by simply shifting the center frequency of the matched filter for  $x(t)$  to the expected Doppler shift.

A more interesting situation occurs when the velocity is not known in advance so that the receiver filter is not matched to the target Doppler shift. More generally, suppose the filter is matched to some Doppler shift  $\Omega_i$  radians per second but the actual Doppler shift of the echo is  $\Omega_D$ . Choosing  $T_M = 0$  for simplicity, the matched filter output will be zero for  $|t| > \tau$ . For  $0 \leq t \leq \tau$  the response is

$$y(t) = \alpha \int_t^\tau \exp(j\Omega_D s) \exp[-j\Omega_i(s-t)] ds \quad (4.25)$$

If the filter is in fact matched to the actual Doppler shift,  $\Omega_i = \Omega_D$ , the output becomes

$$\begin{aligned} y(t) &= \alpha \exp(j\Omega_D t) \int_t^\tau (1) ds \\ &= \alpha e^{j\Omega_D t} (\tau - t), \quad 0 \leq t \leq \tau \end{aligned} \quad (4.26)$$

The analysis is similar for negative  $t$ ,  $-\tau \leq t \leq 0$ . The complete result is

$$y(t) = \begin{cases} \alpha e^{j\Omega_D t} (\tau - |t|), & -\tau \leq t \leq \tau \\ 0, & \text{otherwise} \end{cases} \quad (4.27)$$

Thus,  $|y(t)|$  is the usual triangular function, peaking as expected at  $t = 0$ .

If there is a Doppler mismatch,  $\Omega_i \neq \Omega_D$ , the response at the expected peak time  $t = 0$  is

$$\begin{aligned} y(t)|_{t=0} &= \alpha \int_0^\tau \exp(j\Omega_D s) \exp(-j\Omega_i s) ds \\ &= \alpha \int_0^\tau \exp[j(\Omega_D - \Omega_i)s] ds \\ &= \frac{\alpha}{j(\Omega_D - \Omega_i)} \exp[j(\Omega_D - \Omega_i)s] \Big|_0^\tau \end{aligned} \quad (4.28)$$

Defining  $\Omega_{\text{diff}} \equiv \Omega_D - \Omega_i$

$$|y(0)| = \left| \frac{2\alpha \sin(\Omega_{\text{diff}}\tau/2)}{\Omega_{\text{diff}}} \right| \quad (4.29)$$

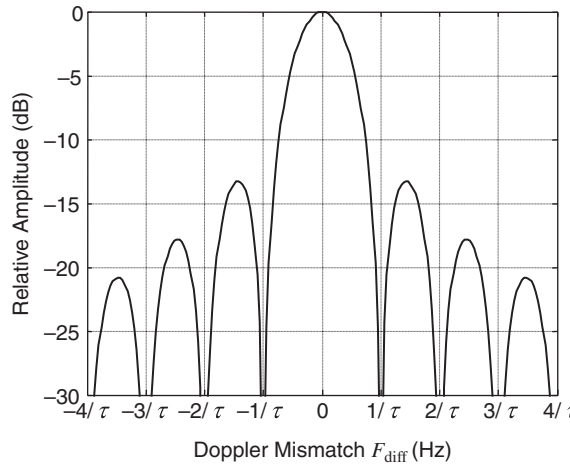


FIGURE 4.6 Effect of Doppler mismatch on matched filter response at expected peak time.

Equation (4.29) is plotted in Fig. 4.6. The first zero of this sinc function occurs at  $F_{\text{diff}} = 1/\tau$  Hz.<sup>2</sup> Relatively small Doppler mismatches ( $F_{\text{diff}} \ll 1/\tau$ ) will cause only slight reductions in the matched filter output peak amplitude. Large mismatches, however, can cause very substantial reductions.

The effect of Doppler mismatch can be either good or bad. If targets are moving and the velocities are unknown, mismatch will cause reductions in observed peaks and, if severe enough, may prevent detection. The signal processor must either estimate the target Doppler so that the matched filter can be adjusted or construct matched filters for a number of different possible Doppler frequencies and observe the output of each to search for targets. On the other hand, if the goal is to be selective in responding only to targets of a particular Doppler shift, it is desirable to have a matched filter that suppresses targets at other Doppler shifts.

From Fig. 4.6, it is clear that the Rayleigh resolution of the Doppler mismatch response is  $1/\tau$  Hz. The resolution in velocity is therefore  $\lambda/2\tau$  meters per second. For typical pulse lengths, these are fairly large values. For example, a 10  $\mu$ s pulse would exhibit a Rayleigh resolution in Doppler of 100 kHz, or in velocity at X band (10 GHz) of 1500 m/s. Many systems do not observe such high Doppler shifts, so Doppler mismatch effects are insignificant and targets cannot be resolved in Doppler on a single pulse. If finer Doppler resolution is desired, a very long pulse may be needed. For example, velocity resolution of 1 m/s at X band requires a 15-ms pulse. The range resolution is then a very poor 2250 km. This conflict between good range resolution and good Doppler resolution can be resolved using a pulse burst waveform, which will be addressed in Sec. 4.5.

## 4.4 The Ambiguity Function

### 4.4.1 Definition and Properties of the Ambiguity Function

In the preceding sections, the matched filter response for the simple pulse waveform has been analyzed to show its behavior both in time and in response to Doppler mismatches.

<sup>2</sup>Note that a frequency component of  $1/\tau$  hertz goes through exactly one full cycle during a pulse of duration  $\tau$  seconds.

The *ambiguity function* (AF) is an analytical tool for waveform design and analysis that succinctly characterizes the behavior of a waveform paired with its matched filter. The AF is useful for examining resolution, sidelobe behavior, and ambiguities in both range and Doppler for a given waveform, as well as phenomena such as range-Doppler coupling (introduced in Sec. 4.6.4).

Consider the output of a matched filter for a waveform  $x(t)$  when the input is a Doppler-shifted response  $x(t)\exp(j2\pi F_D t)$ . Also assume that the filter has unit gain ( $\alpha = 1$ ) and is designed to peak at  $T_M = 0$ ; this merely means that the time axis at the filter output is relative to the expected peak output time for the range of the target. The filter output will be

$$\begin{aligned} y(t; F_D) &= \int_{-\infty}^{\infty} x(s)\exp(j2\pi F_D s)x^*(s-t) ds \\ &\equiv \hat{A}(t, F_D) \end{aligned} \quad (4.30)$$

which is defined as the *complex ambiguity function*  $\hat{A}(t, F_D)$ . An equivalent definition can be given in terms of the signal spectrum by applying basic Fourier transform properties:

$$\hat{A}(t, F_D) = \int_{-\infty}^{\infty} X^*(F)X(F - F_D)\exp(j2\pi Ft) dF \quad (4.31)$$

The *ambiguity function*<sup>3</sup> is defined as the magnitude of  $\hat{A}(t, F_D)$ ,

$$A(t, F_D) \equiv |\hat{A}(t, F_D)| \quad (4.32)$$

It is a function of two variables: the time delay relative to the expected matched filter peak output, and the mismatch between that Doppler shift for which the filter was designed, and that which is actually received. For example, the AF evaluated at time  $t = 0$  corresponds to the output of the actual matched filter at time  $t = 2R_0/c + \tau$  for a target at range  $R_0$ . The particular form of the AF is determined entirely by the complex waveform  $x(t)$ .

Three properties of the ambiguity function are of immediate interest. The first states that if the waveform has energy  $E$ , then

$$|A(t, F_D)| \leq |A(0, 0)| = E \quad (4.33)$$

Thus, when the filter is matched in Doppler to the echo and is sampled at a delay corresponding to the target range, the response will be maximum. If the filter is not matched or is sampled at a different delay, then the response will be less than or equal to (usually less than) the maximum. The second property states that total area under any ambiguity function is constant and is given by

$$\int_{-\infty}^{\infty} \int_{-\infty}^{\infty} |A(t, F_D)|^2 dt dF_D = E^2 \quad (4.34)$$

This conservation of energy statement implies that, in the design of waveforms, one cannot remove energy from one portion of the ambiguity surface without placing it somewhere else; it can only be moved around on the ambiguity surface. The third property is a symmetry relation:

$$A(t, F_D) = A(-t, -F_D) \quad (4.35)$$

---

<sup>3</sup>Some authors define the term “ambiguity function” as  $|\hat{A}(t, F_D)|^2$  or as  $\hat{A}(t, F_D)$  itself. Also, some authors define the ambiguity function as  $|\int_{-\infty}^{\infty} x(s)\exp(j2\pi F_D s)x^*(s+t) ds|$  instead of  $|\int_{-\infty}^{\infty} x(s)\exp(j2\pi F_D s)x^*(s-t) ds|$ . The definition used here is consistent with that given in Rihaczek (1996).

In order to prove the first property, start with the square of Eq. (4.32)

$$|A(t, F_D)|^2 = \left| \int_{-\infty}^{\infty} x(s)x^*(s-t)\exp(j2\pi F_D s) ds \right|^2 \quad (4.36)$$

Applying the Schwartz inequality to Eq. (4.36) yields

$$\begin{aligned} |A(t, F_D)|^2 &\leq \int_{-\infty}^{\infty} |x(s)|^2 ds \int_{-\infty}^{\infty} |x^*(s-t)\exp(j2\pi F_D s)|^2 ds \\ &= \int_{-\infty}^{\infty} |x(s)|^2 ds \int_{-\infty}^{\infty} |x^*(s-t)|^2 ds \end{aligned} \quad (4.37)$$

Each integral is just the energy  $E$  in  $x(t)$ , so that

$$|A(t, F_D)|^2 \leq E^2 \quad (4.38)$$

The equality holds only if  $x(s) = x(s-t)\exp(-j2\pi F_D s)$  for all  $s$ , which occurs if and only if  $t = F_D = 0$ . Making these substitutions in Eq. (4.38) gives the equality in Eq. (4.33).

The proof of the second property starts by defining the complex conjugate of the complex ambiguity function, where

$$\begin{aligned} \hat{A}^*(t, F_D) &= \int_{-\infty}^{\infty} x^*(s) x(s-t)\exp(-j2\pi F_D s) ds \\ &= \int_{-\infty}^{\infty} X(F)X^*(F-F_D)\exp(-j2\pi F t) dF \end{aligned} \quad (4.39)$$

The squared magnitude of the ambiguity function can then be written as

$$\begin{aligned} |A(t, F_D)|^2 &= \hat{A}(t, F_D)\hat{A}^*(t, F_D) \\ &= \int_{-\infty}^{\infty} \int_{-\infty}^{\infty} x(s)x^*(s-t)X(F)X^*(F-F_D)\exp[j2\pi(F_D s - F t)] ds dF \end{aligned} \quad (4.40)$$

The total energy in the ambiguity surface is

$$\begin{aligned} \int_{-\infty}^{\infty} \int_{-\infty}^{\infty} |A(t, F_D)|^2 dt dF_D &= \frac{1}{2\pi} \int_{-\infty}^{\infty} \int_{-\infty}^{\infty} \int_{-\infty}^{\infty} \int_{-\infty}^{\infty} x(s)x^*(s-t)X(F)X^*(F-F_D) \\ &\quad \times \exp[j2\pi(F_D s - F t)] ds dF dt dF_D \end{aligned} \quad (4.41)$$

Isolating those terms integrated over  $t$  and  $F_D$  yields the following two relationships:

$$\int_{-\infty}^{\infty} x^*(s-t)\exp(-j2\pi F t) dt = \exp(-j2\pi F s)X^*(F) \quad (4.42)$$

$$\int_{-\infty}^{\infty} X^*(F-F_D)\exp(j2\pi F_D s) dF_D = \exp(j2\pi F s)x^*(s) \quad (4.43)$$

Substituting these into Eq. (4.41) yields

$$\begin{aligned} \int_{-\infty}^{\infty} \int_{-\infty}^{\infty} |A(t, F_D)|^2 dt dF_D &= (1/2\pi) \int_{-\infty}^{\infty} \int_{-\infty}^{\infty} x(s)X^*(F)X(F)x^*(s) ds dF \\ &= \left\{ \int_{-\infty}^{\infty} |x(s)|^2 ds \right\} \left\{ 1/2\pi \int_{-\infty}^{\infty} |X(F)|^2 dF \right\} \end{aligned} \quad (4.44)$$

The first integral on the right-hand side of Eq. (4.44) is just the energy  $E$  of the pulse measured in the time domain; the second is, by Parseval's theorem, also the energy. Thus

$$\int_{-\infty}^{\infty} \int_{-\infty}^{\infty} |A(t, F_D)|^2 dt dF_D = E^2 \quad (4.45)$$

The symmetry property can be proved by substituting  $-t$  and  $-F_D$  for  $t$  and  $F_D$ , respectively, in the definition in Eq. (4.30)

$$\hat{A}(-t, -F_D) = \int_{-\infty}^{\infty} x(s) \exp(-j2\pi F_D s) x^*(s+t) ds \quad (4.46)$$

Now make the change of variables  $s' = s + t$  to get

$$\begin{aligned} \hat{A}(-t, -F_D) &= \int_{-\infty}^{\infty} x(s'-t) \exp(-j2\pi F_D(s'-t)) x^*(s') ds' \\ &= \exp(j2\pi F_D t) \int_{-\infty}^{\infty} x(s'-t) \exp(-j2\pi F_D s') x^*(s') ds' \\ &= \exp(j2\pi F_D t) \hat{A}^*(t, F_D) \end{aligned} \quad (4.47)$$

Since  $A(t, F_D) \equiv |\hat{A}(t, F_D)|$ , Eq. (4.35) follows immediately.

It is reasonable to ask what would be an ideal ambiguity function. The answer varies depending on the intent of the system design, but a commonly cited goal is the "thumbtack" ambiguity function of Fig. 4.7, which features a single central peak with the remaining energy spread uniformly throughout the delay-Doppler plane. The narrow central peak implies good resolution in both range and Doppler. The lack of any secondary peak implies that there will be no range or Doppler ambiguities. The uniform plateau suggests low and uniform sidelobes, minimizing target masking effects. All of these features are beneficial for a system designed to make fine-resolution measurements of targets in range and Doppler or to perform radar imaging. On the other hand, a waveform intended to be used for target search might be preferred to be more tolerant of Doppler mismatch so that the Doppler shift of targets whose velocity is not yet known does not prevent their detection due to a weak response at the matched filter output. Thus, what is "ideal" in the way of an ambiguity function depends on the use to which the waveform will be put.

#### 4.4.2 Ambiguity Function of the Simple Pulse

As a first example of an ambiguity function, consider a simple pulse centered on the origin and normalized to have unit energy ( $E = 1$ ) for convenience

$$x(t) = \frac{1}{\sqrt{\tau}}, \quad -\frac{\tau}{2} \leq t \leq \frac{\tau}{2} \quad (4.48)$$

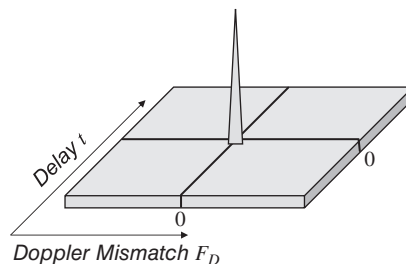


FIGURE 4.7 "Thumbtack" ambiguity function.

Applying Eq. (4.30) gives for  $t > 0$

$$\begin{aligned}\hat{A}(t, F_D) &= \int_{-\tau/2+t}^{\tau/2} \frac{1}{\tau} \exp(j2\pi F_D s) ds \\ &= \frac{\exp[j2\pi F_D \tau/2] - \exp[j2\pi F_D(-\tau/2+t)]}{\tau j2\pi F_D} \\ &= \frac{1}{\tau j2\pi F_D} e^{j2\pi F_D t/2} \left\{ \exp\left[j2\pi F_D\left(\frac{\tau}{2} - \frac{t}{2}\right)\right] \right. \\ &\quad \left. - \exp\left[-j2\pi F_D\left(\frac{\tau}{2} - \frac{t}{2}\right)\right] \right\} \end{aligned} \quad (4.49)$$

The ambiguity function for  $t > 0$  is the magnitude of Eq. (4.49)

$$A(t, F_D) = |\hat{A}(t, F_D)| = \left| \frac{\sin(\pi F_D(\tau-t))}{\tau \pi F_D} \right|, \quad 0 \leq t \leq \tau \quad (4.50)$$

Repeating the derivation for  $t < 0$  gives a similar result, but with the quantity  $(\tau-t)$  replaced by  $(t+\tau)$ . The complete AF of the simple pulse is therefore

$$\begin{aligned}A(t, F_D) &= \left| \frac{\sin[\pi F_D(\tau-|t|)]}{\tau \pi F_D} \right| \\ &= \left( 1 - \frac{|t|}{\tau} \right) \left| \frac{\sin[\pi F_D \tau(1-|t|/\tau)]}{\pi F_D \tau(1-|t|/\tau)} \right|, \quad -\tau \leq t \leq \tau \end{aligned} \quad (4.51)$$

Equation (4.51) is plotted in Fig. 4.8 in a three-dimensional surface plot and in Fig. 4.9 as a contour plot, which is often easier to interpret and is therefore used in most cases in the

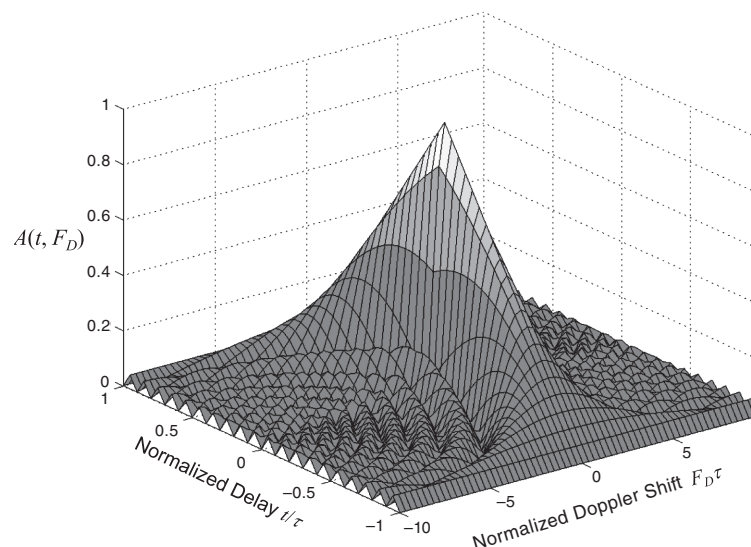


**FIGURE 4.8** Ambiguity function of a unit-energy simple pulse of length  $\tau$ .

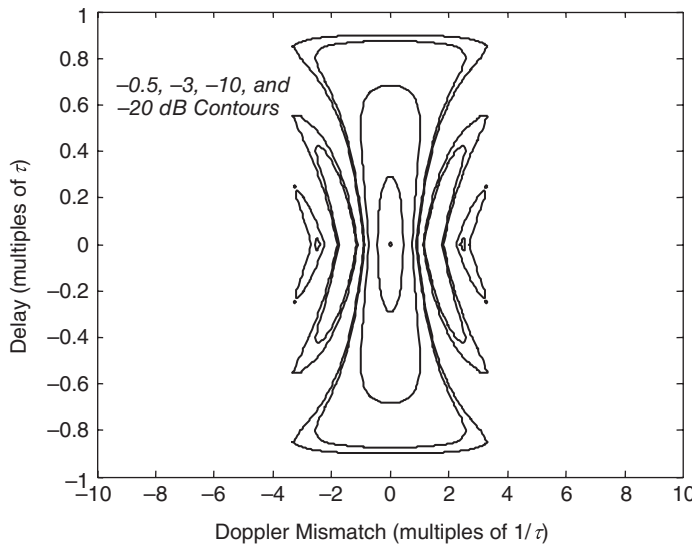


**FIGURE 4.9** Contour plot of the simple pulse ambiguity function of Fig. 4.8.

remainder of this chapter. The AF for a simple pulse is a triangular ridge oriented along the delay axis. Doppler mismatches on the order of  $1/\tau$  Hz or more drastically reduce and spread the matched filter output peak, as was shown previously.

The zero-Doppler response  $A(t, 0)$  gives the matched filter output when there is no Doppler mismatch. Setting  $F_D = 0$  in Eq. (4.51) and using L'Hôpital's rule to resolve the indeterminate form gives

$$\begin{aligned} A(t, 0) &= \left| \frac{\pi(\tau - |t|) \cos[\pi F_D(\tau - |t|)]}{\tau \pi} \right|_{F_D=0} \\ &= \frac{\tau - |t|}{\tau}, \quad -\tau \leq t \leq \tau \end{aligned} \quad (4.52)$$

Similarly, the zero-delay cut  $A(0, F_D)$  gives the output of the matched filter at the expected peak time  $t = 0$  as a function of Doppler mismatch. Using  $t = 0$  in Eq. (4.51) immediately gives

$$A(0, F_D) = \left| \frac{\sin(\pi F_D \tau)}{\tau \pi F_D} \right| \quad (4.53)$$

Equations (4.52) and (4.53) are the expected triangle and sinc functions derived previously. They are illustrated in Fig. 4.10.

A Doppler mismatch not only reduces the peak amplitude but, if severe enough, completely alters the shape of the range response of the matched filter. Figure 4.11 shows the effect of varying degrees of Doppler mismatch on the matched filter range response. These curves should be compared to Fig. 4.10a. A mismatch of  $0.31/\tau$  Hz results in a reduction of about 16 percent in the peak amplitude, but the peak remains at the correct time delay. A larger shift, for example  $0.94/\tau$ , not only reduces the maximum output amplitude by 65 percent but eliminates the central peak altogether. By the time the mismatch is several times  $1/\tau$ , the response becomes completely unstructured. Note that a mismatch of  $n/\tau$  Hz means that there will be  $n$  cycles of the Doppler frequency during the pulse duration  $\tau$ .

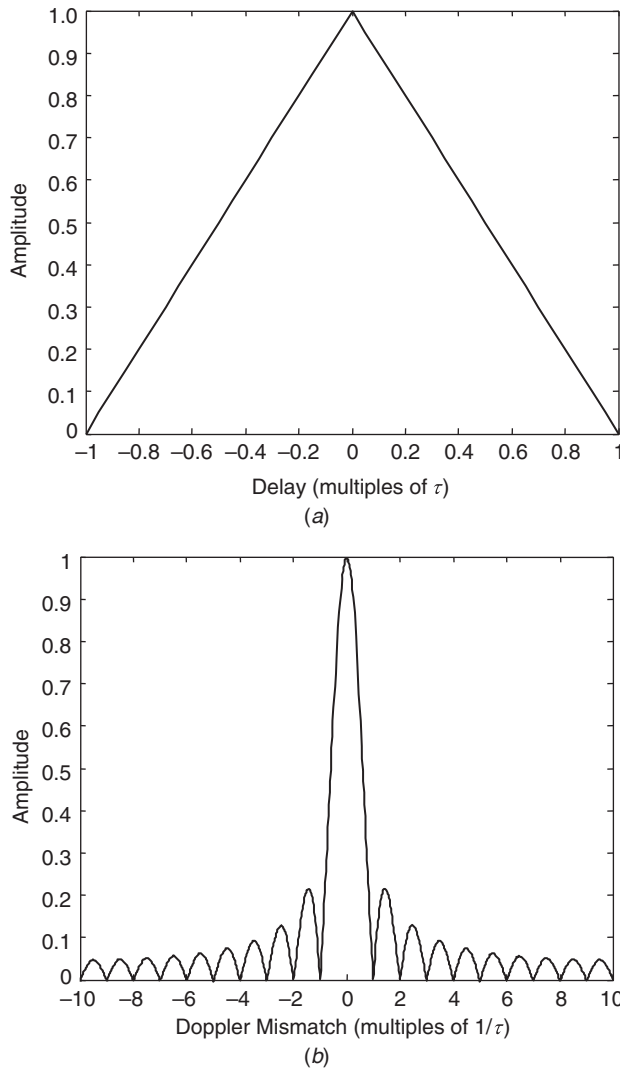


**FIGURE 4.10** (a) Zero-Doppler cut of simple pulse AF, (b) zero-delay cut.

Also recall that for typical pulse lengths,  $1/\tau$  is a large Doppler shift, so that the simple pulse still ranks as a relatively Doppler-tolerant waveform. For instance, if  $\tau = 10 \mu\text{s}$ , a Doppler shift of  $0.31/\tau$  is 31 kHz, corresponding at an RF of 10 GHz to a velocity of 465 m/s, or 1040 mph. Even with this very large Doppler mismatch, the simple pulse matched filter output retains its basic shape, correct peak location, and suffers only the 16 percent (1.5 dB) amplitude loss.

## 4.5 The Pulse Burst Waveform

The flip side of the Doppler tolerance of the simple pulse described in the preceding example is that its Doppler resolution is very poor. If the designer wants the radar system to respond to targets only at certain velocities and reject targets at nearby velocities, the simple pulse is

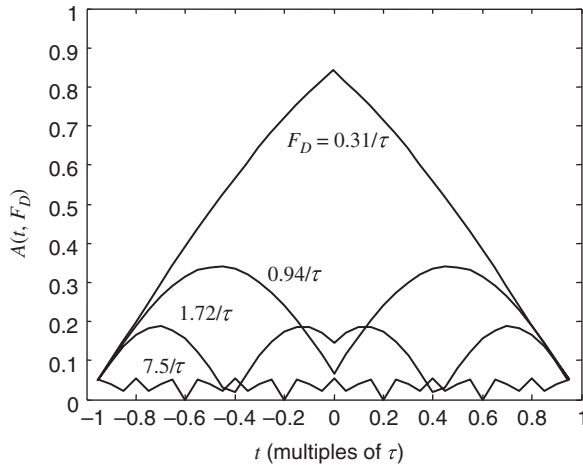


**FIGURE 4.11** Effect of Doppler mismatch on the range response of the matched filter for the simple pulse.

not adequate as a waveform. Better frequency resolution requires a longer observation time. The *pulse burst waveform* is one way to meet this requirement. It is defined as

$$x(t) = \sum_{m=0}^{M-1} x_p(t - mT) \quad (4.54)$$

where  $x_p(t)$  = single pulse of length  $\tau$

$M$  = number of pulses in the burst

$T$  = pulse repetition interval

While the constituent pulse  $x_p(t)$  can be any single-pulse waveform, for the moment only the simple pulse will be considered. Figure 4.12 illustrates this waveform. The solid line forming the envelope of the sinusoidal pulses is the actual baseband waveform  $x(t)$ . The train of RF pulses that results when it is impressed upon a carrier is denoted as usual as  $\bar{x}(t)$ . The total duration  $MT$  (which includes the dead time after the last pulse) is the *coherent processing interval* (CPI).

#### 4.5.1 Matched Filter for the Pulse Burst Waveform

The matched filter for the pulse burst is (with  $\alpha = 1$  and  $T_M = 0$ )

$$h(t) = x^*(-t) = \sum_{m=0}^{M-1} x_p^*(-t - mT) \quad (4.55)$$

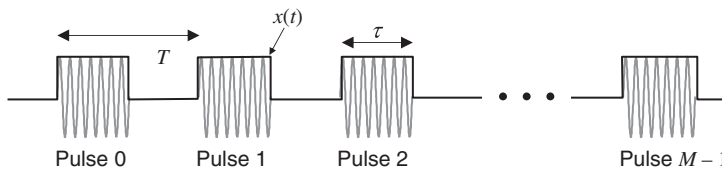


**FIGURE 4.12** Pulse burst waveform and the resulting train of RF pulses.

and the matched filter output, given an echo from a range corresponding to a time delay  $t_0$ , is therefore

$$\begin{aligned} y(t) &= \int_{-\infty}^{\infty} \left\{ \sum_{m=0}^{M-1} x_p(s-t_0-mT) \right\} \left\{ \sum_{n=0}^{M-1} x_p^*(s-t-nT) \right\} ds \\ &= \sum_{m=0}^{M-1} \sum_{n=0}^{M-1} \int_{-\infty}^{\infty} x_p(s-t_0-mT) x_p^*(s-t-nT) ds \end{aligned} \quad (4.56)$$

The inner integral is the matched filter output for the constituent simple pulse. Let  $t_0 = 0$  for simplicity; the results can be adjusted for any other delay  $t_0$  by shift invariance. Renaming the simple pulse matched filter output from Eq. (4.19) as  $s_p(t)$ , Eq. (4.56) becomes

$$y(t) = \sum_{m=0}^{M-1} \sum_{n=0}^{M-1} s_p(-t-(m-n)T) = \sum_{m=0}^{M-1} \sum_{n=0}^{M-1} s_p^*(t-(n-m)T) \quad (4.57)$$

where the symmetry of  $s_p(t)$  has been used in the last step. Equation (4.57) states that the matched filter output is a superposition of shifted copies of  $s_p(t)$ . The double summation can be simplified by noting that all terms that have the same value of  $(n - m)$  are identical and can be combined. There are  $M$  combinations of  $m$  and  $n$  such that  $m - n = 0$ , namely, all those where  $m = n$ . There are  $M - 1$  cases where  $m - n = +1$  and another  $M - 1$  cases where  $m - n = -1$ . Continuing in this vein gives

$$y(t) = \sum_{m=-\left(M-1\right)}^{M-1} (M - |m|) s_p^*(t - mT) \quad (4.58)$$

The matched filter output for the pulse burst waveform is simply a sum of scaled and shifted replicas of the output of the filter matched to a single constituent pulse.

Since the constituent pulse  $x_p(t)$  is of duration  $\tau$ ,  $s_p(t)$  is of duration  $2\tau$ . If  $T > 2\tau$  as is usually the case, none of the replicas of  $s_p(t)$  overlap one another. Figure 4.13 illustrates a pulse burst waveform and the corresponding matched filter output for this case and  $M = 3$ . The peak output occurs at  $t = T_M = 0$ :

$$\begin{aligned} y(0) &= \sum_{m=-\left(M-1\right)}^{M-1} (M - |m|) s_p^*(-mT) = \sum_{m=-\left(M-1\right)}^{M-1} (M - |m|) s_p(mT) \\ &= M s_p(0) = M E_p = E \end{aligned} \quad (4.59)$$

where the last step uses  $s_p(mT) = 0$  when  $T > \tau$ . In this equation  $E_p$  is the energy in the single pulse  $x_p(t)$ , while  $E$  is the energy in the entire  $M$ -pulse waveform. Note that the peak response is  $M$  times that achieved with a single pulse of the same amplitude. Recall the radar range equation signal processing gain factor  $G_{sp}$  of Eq. (2.85). The increase in the matched filter output peak for the pulse burst waveform represents a coherent signal processing gain of a factor  $G_{sp} = M$  that will improve the SNR compared to a single-pulse waveform, aiding detection probability and measurement precision.

### 4.5.2 Pulse-by-Pulse Processing

The structure of Eq. (4.58) suggests that it is not necessary to construct an explicit matched filter for the entire pulse burst waveform  $x(t)$ , but rather that the matched filter can be implemented by filtering the data from each individual pulse with the single-pulse matched filter and then combining those outputs. This process, called *pulse-by-pulse* processing, uses separable two-dimensional processing in fast time and slow time. It provides a much more convenient implementation and is consistent with how pulse burst waveforms are processed in real systems.

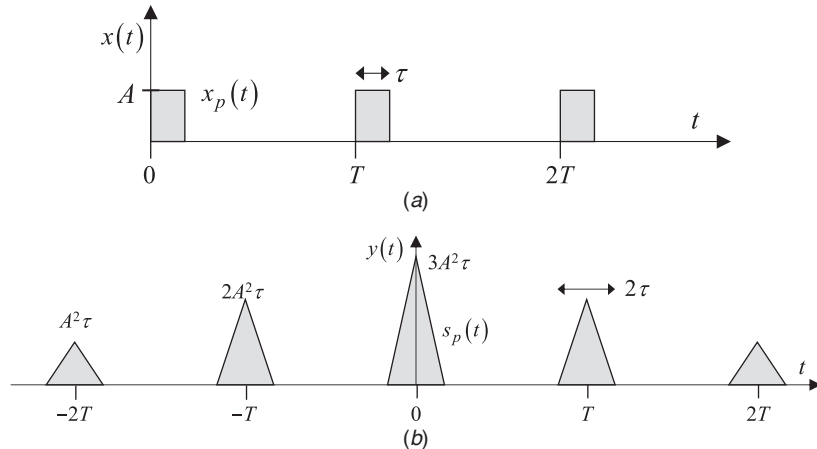


FIGURE 4.13 (a) Pulse burst waveform,  $M = 3$ , (b) matched filter output.

Define the matched filter impulse response for the individual pulse in the burst, assuming  $T_M = 0$

$$h_p(t) = x_p^*(-t) \quad (4.60)$$

The output from this filter for the  $m$ th transmitted pulse, assuming a target at some delay  $t_l$ , is

$$\begin{aligned} y_m(t) &= x_p(t - t_l - mT) * h_p(t) \\ &= s_p^*(t - t_l - mT) = s_p(-t + t_l + mT), \quad 0 \leq m \leq M-1 \end{aligned} \quad (4.61)$$

Assume that the echo from the individual pulse matched filter for the first pulse ( $m = 0$ ) is sampled at  $t = t_l$ ; that value will be  $y_0(t_l) = s_p(0)$ . Now sample the filter response to each succeeding pulse at the same delay after its transmission (i.e., sample the same range bin for each pulse). The filter output for pulse  $m$  is sampled at  $t = t_l + mT$ , giving  $y_m(t_l + mT) = s_p(0)$  again.

If the sample taken at time  $t_l$  after pulse transmission is associated with range bin  $l$ , the  $M$  samples so obtained form a discrete constant-valued sequence  $y[l, m] = s_p(0)$ ,  $0 \leq m \leq M-1$ . The discrete-time causal matched filter in the slow-time ( $m$ ) dimension for such a sequence is  $h[m] = \alpha y^*[M-1-m]$ ; with  $\alpha = 1/s_p(0)$ ,  $h[m] = 1$  for  $0 \leq m \leq M-1$ . The output of this discrete-time matched filter is

$$\begin{aligned} z[m] &= \sum_{r=0}^{M-1} y[l, r] h[m-r] \\ &= \begin{cases} \sum_{r=0}^m y[l, r](1), & 0 \leq m \leq M-1 \\ \sum_{r=m-M+1}^{M-1} y[l, r](1), & M-1 \leq m \leq 2(M-1) \end{cases} \end{aligned} \quad (4.62)$$

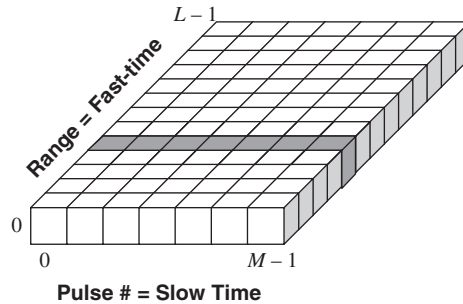


**FIGURE 4.14** Slow-time sequence to be integrated for matched filtering of a pulse burst waveform.

The peak output will occur when the two functions in the summand completely overlap, which requires  $m = M - 1$ ; then

$$z[M-1] = \sum_{r=0}^{M-1} y[l, r] = Ms_p(0) = ME_p = E \quad (4.63)$$

Equation (4.63) indicates that in pulse-by-pulse processing, matched filtering of the slow-time sequence from a given range bin reduces to coherently integrating the slow-time samples in each range bin, and the resulting peak output is identical to that obtained with a whole-waveform continuous matched filter of Eq. (4.55). Figure 4.14 illustrates the row of slow-time samples that are integrated (after matched filtering of the single pulse in fast time) to complete the matched filtering process for the pulse burst. This operation is performed independently for each range bin.

### 4.5.3 Range Ambiguity

Evaluating the pulse burst matched filter output at  $t = 0$  gave the peak output for a target at the time delay  $t_0$  under consideration. Normally  $t_0 < T$  and if a peak is observed it will be interpreted as implying the presence of a target at range  $R_0 = ct_0/2$  m. However, suppose the data instead contain echoes from a target an additional  $T$  seconds of delay further away. The received waveform will be unchanged except for a delay of  $T$  seconds and a reduced amplitude according to the range equation. The amplitude reduction is not pertinent to the discussion and is ignored. By shift invariance, the matched filter output of Eq. (4.58) will also be delayed by  $T$  seconds

$$y(t) = \sum_{m=-(M-1)}^{M-1} (M - |m|) s_p^*[t - (m+1)T] \quad (4.64)$$

Now when the matched filter output is evaluated at  $t = 0$  the result is

$$y(0) = \sum_{m=-(M-1)}^{M-1} (M - |m|) s_p^*[-(m+1)T] \quad (4.65)$$

In this expression (and continuing to assume  $T > 2\tau$ ) only the  $m = -1$  term is nonzero, so that

$$y(0) = (M - 1)s_p(0) = (M - 1)E_p \quad (4.66)$$

This equation shows that the output at the sample time is reduced from  $ME_p$  to  $(M - 1)E_p$ . The situation is illustrated in Fig. 4.15 from both the whole-waveform matched filter and pulse-by-pulse viewpoints. From the former viewpoint, a local peak of the matched filter output is

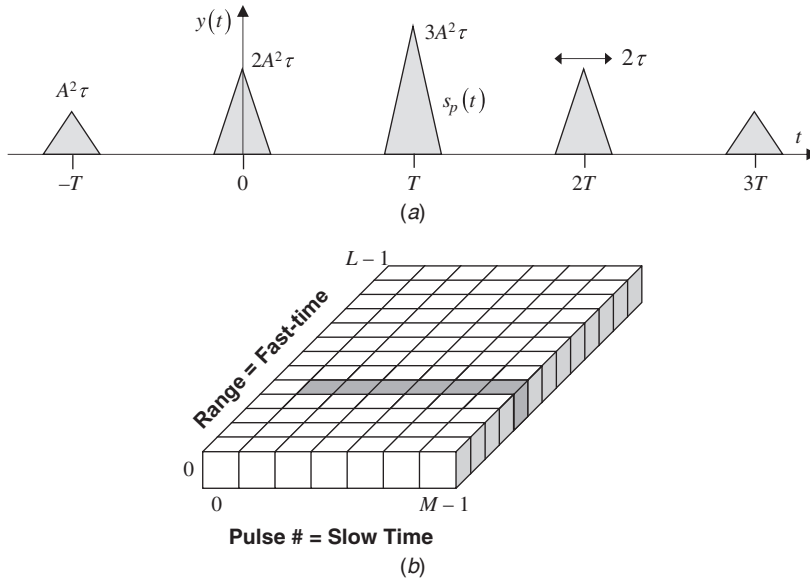


**FIGURE 4.15** Pulse burst matched filtering when target is range ambiguous by one PRI: (a) whole-waveform matched filter output. Compare to Fig. 4.13b. (b) Slow-time data in pulse-by-pulse processing viewpoint. Compare to Fig. 4.14.

sampled, but the global peak is missed because the filter is “tuned” for the wrong delay. The result, while not zero, is a reduced-amplitude sample, reducing SNR. From the latter viewpoint, the echo appears in only  $M - 1$  of the  $M$  slow-time samples integrated because it first returns after the sampling window following transmission of the second pulse rather than the first.

This behavior creates two problems. The reduced amplitude of the target component of the matched filter output reduces the SNR and thus the probability of detecting the target. Assuming the reduced-amplitude response does prove large enough to be detected, the processor will assume the target is at delay  $t_0$  when in fact it is at  $t_0 + T$ . This phenomenon whereby there is more than one possible range that can be associated with a detection is called a range ambiguity. First discussed in Chap. 3, it is a characteristic of pulse burst waveforms. It is not readily apparent if a peak at the matched filter output is due to a target at the implied range or at that range plus a multiple of the unambiguous range  $R_{ua} = cT/2$  meters.

As will be seen in Chap. 5, it is common in some radars to operate at a PRF for which the unambiguous range is less than the maximum detection range, so methods are needed to counter these two problems. Range ambiguities can be resolved using multiple pulse burst waveforms at different PRFs as discussed in Chap. 5. The reduction in matched filter output amplitude and SNR for range-ambiguous targets is countered by noting that it occurs because the pulse burst echo is not fully overlapped with the matched filter reference pulse burst at the output sampling time when the target time delay  $t_0 > T$ . The solution to this problem is to extend the transmitted waveform. Suppose the radar can be expected to detect targets at ranges up to  $P \cdot R_{ua}$ . Extend the transmitted waveform from  $M$  to  $M + P - 1$  pulses. The receiver matched filter remains the same  $M$ -pulse waveform. Still using  $t_0 = 0$  and  $T_M = 0$ , the matched filter output will be the waveform shown in Fig. 4.16a. It indicates that the full integrated target power of  $MA^2\tau = ME_p$  will be obtained for a target at the delay  $T_M$  (zero in the figure) for which the matched filter is tuned, but also for targets at the ambiguous delays  $T_M + pT$ ,  $p = 0, \dots, P - 1$ . Evaluating the matched filter output for delays  $T_M$  between zero and

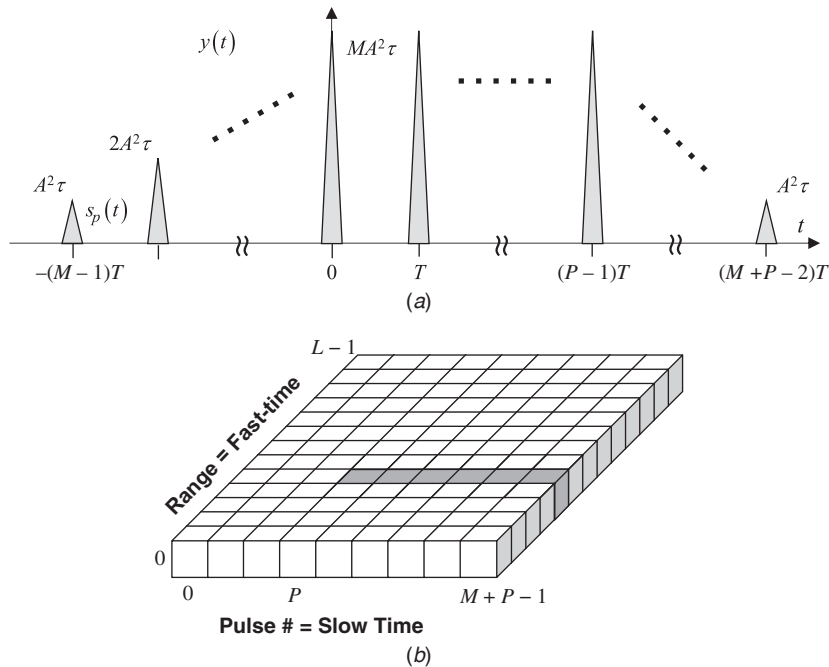


**FIGURE 4.16** Effect of extending the transmitted waveform with additional pulses when  $P$  range ambiguities can occur: (a) whole-waveform matched filter output. (b) slow-time data in pulse-by-pulse processing viewpoint.

$T$  allows full-SNR matched filtering of targets at delays up to  $T_M + (P-1)T$ , corresponding to ranges up to  $P \cdot R_{ua}$  as desired. The pulse-by-pulse viewpoint is shown in Fig. 4.16b. A target in the  $P$ th delay interval,  $(P-1)T \leq t_0 < PT$ , will produce a response in the appropriate range bin in the  $P$ th and later slow time samples. By integrating only samples  $P$  through  $M+P-1$  in each range bin the design integration gain of  $M$  can be achieved for all targets up to ranges  $P \cdot R_{ua}$ .

Another issue arises with pulse burst waveforms and clutter echoes. Suppose the radar can be expected to receive significant clutter returns at ranges up to  $P \cdot t_{uar}$  and consider the clutter component of the slow-time signal for a given range bin in the pulse-by-pulse processing viewpoint. When the range bin of interest is sampled at delay  $t_0 < T$  after the first pulse is transmitted, only clutter echoes from the corresponding range  $ct_0/2$  will be sampled at the receiver. When the range bin is sampled again after the second pulse, the clutter component will include echoes from the second pulse and range  $ct_0/2$  as well as from the first pulse and range  $c/2(t_0 + T)$ . These two contributions represent echo from two physically different patches of clutter scatterers. The first slow-time sample, which includes echoes from only the nearer patch, may differ significantly in power and statistical behavior from the second slow-time sample, which includes echoes from both. The  $P$ th and subsequent slow-time samples will contain contributions from all  $P$  contributing range intervals and therefore exhibit the consistent clutter power levels and statistical behavior needed for effective clutter filtering and target detection. Extending the transmitted waveform to  $M+P-1$  pulses as above therefore allows collection of  $M$  steady-state clutter measurements. In Chap. 5 these additional pulses will be called “clutter fill” pulses. The first  $P-1$  slow-time samples will be discarded in each range bin and only the remaining  $M$  samples will be used in clutter filtering, coherent integration, and detection processing.

#### 4.5.4 Doppler Response of the Pulse Burst Waveform

To consider the effect of a Doppler mismatch on the pulse burst waveform and its matched filter, consider a target moving toward the radar at velocity  $v$  meters per second so that its range is  $R_0 - vt$  meters at time  $t$ . Assume that the “stop-and-hop” approximation is valid and that the target motion does not exceed one range bin over the CPI, that is,  $MvT < c\tau/2$ ; this ensures that all echoes from a given target appear in the same range bin over the course of a CPI. The demodulated echoes will have a phase shift of  $-(4\pi/\lambda)R(t) = -(4\pi/\lambda)(R_0 - vt)$ . Adopting the pulse-by-pulse processing viewpoint and absorbing the phase  $\exp(-j4\pi R_0/\lambda)$  due to the nominal range  $R_0$  into the overall gain, the individual matched filtered outputs for each pulse become

$$\begin{aligned} y_m(t) &= x_p(t - mT) * h_p(t) \\ &= e^{j(4\pi v/\lambda)mT} s_p(-t + mT), \quad 0 \leq m \leq M-1 \end{aligned} \quad (4.67)$$

The corresponding slow-time sequence is

$$\begin{aligned} y[l, m] &= y_m(mT) = e^{j(4\pi v/\lambda)mT} s_p(0), \quad 0 \leq m \leq M-1 \\ &= e^{j\omega_D m} E_p \quad (\omega_D = 4\pi v T / \lambda) \end{aligned} \quad (4.68)$$

Integrating the slow-time samples gives

$$\begin{aligned} \sum_{m=0}^{M-1} y[l, m] &= E_p \sum_{m=0}^{M-1} e^{j\omega_D m} \equiv Y[l, \omega_D] \\ &= E_p \frac{\sin[\omega_D M/2]}{\sin[\omega_D/2]} \exp\left[-j\left(\frac{M-1}{2}\right)\omega_D\right] \end{aligned} \quad (4.69)$$

Equation (4.69) gives the system response to the pulse burst waveform in an arbitrary range bin  $l$  as a function of the normalized Doppler mismatch  $\omega_D$ .

This is the familiar asinc function. Figure 4.17 shows the central portion of the magnitude of this function. The zeros occur at intervals of  $1/M$  cycles per sample in normalized

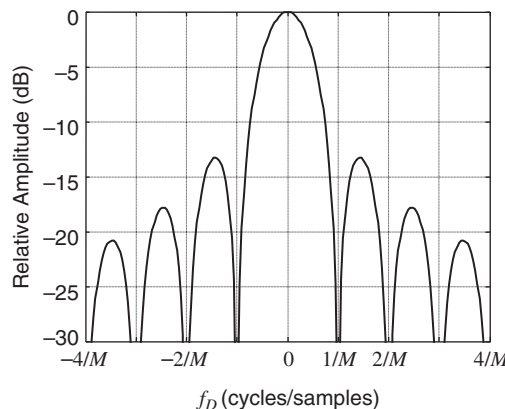


**FIGURE 4.17** Central portion of the Doppler mismatch response of the slow-time signal using a pulse burst waveform.

frequency; thus, the Rayleigh resolution in Doppler is  $1/M$  cycles per sample or  $1/MT$  Hz.  $MT$  is the duration of the entire pulse burst waveform. The Doppler resolution is therefore determined by the duration of the entire waveform instead of the duration of a single pulse. In this manner, the pulse burst waveform achieves much better Doppler resolution than a single pulse of the same duration while maintaining the same range resolution. The cost is the time and energy required to transmit and receive  $M$  pulses instead of one and the computational load of integrating  $M$  samples in each range bin.

Integrating the slow-time samples of the pulse burst echo corresponds to implementing a matched filter in slow time for a signal with zero Doppler shift; in this case the expected slow-time signal is simply a constant. A matched filter for a Doppler-shifted pulse burst can be implemented by continuing to use the single-pulse matched filter in fast time and constructing the appropriate slow-time matched filter for the signal expected for a given Doppler shift.

Suppose the normalized Doppler shift of interest is  $\omega_D$  radians per sample. The expected slow-time signal is then of the form  $A \exp(j\omega_D m)$ . After conjugation and time-reversal the slow-time matched filter coefficients will be  $h[m] = \exp(+j\omega_D m)$ . Consider the response of this filter when the actual Doppler shift of the signal is  $\omega$ . The matched filter peak output occurs when the impulse response and data sequence are fully overlapped, giving

$$\begin{aligned} Y[l, \omega; \omega_D] &= \sum_{m=0}^{M-1} e^{-j\omega_D m} y[l, m] \\ &= E_p \sum_{m=0}^{M-1} e^{-j\omega_D m} e^{j\omega m} = E_p \sum_{m=0}^{M-1} e^{-j(\omega - \omega_D)m} \\ &= E_p \frac{\sin[(\omega - \omega_D)M/2]}{\sin[(\omega - \omega_D)/2]} \exp\left[-j\left(\frac{M-1}{2}\right)(\omega - \omega_D)\right] \end{aligned} \quad (4.70)$$

which is identical to Eq. (4.69) except that the peak of the sinc function has been shifted to  $\omega = \omega_D$  radians per sample.

Note that the first line of Eq. (4.70) is simply the discrete time Fourier transform of the slow-time data sequence. Thus, a matched filter for a pulse burst waveform and a Doppler shift of  $\omega_D$  radians can be implemented with a single-pulse matched filter in fast time and a DTFT in slow time, evaluated at  $\omega_D$ . If  $\omega_D$  is a discrete Fourier transform frequency, i.e., of the form  $2\pi k/K$  for some integers  $k$  and  $K$ , the slow-time matched filter can be implemented with a DFT calculation. It follows that a  $K$ -point DFT of the data  $y[l, m]$  in the slow-time dimension simultaneously computes the output of  $K$ -matched filters, one at each of the DFT frequencies. These frequencies correspond to Doppler shifts of  $F_k = k/KT$  hertz or radial velocities  $v_k = \lambda k/2KT$  meters per second,  $k = 0, \dots, K-1$ . The fast Fourier transform (FFT) algorithm then allows very efficient search of the data for targets at various Doppler shifts by simply applying an FFT to each slow-time row of the data matrix.

### 4.5.5 Ambiguity Function for the Pulse Burst Waveform

Inserting the definition of the pulse burst waveform of Eq. (4.54) into the definition of the complex ambiguity function of Eq. (4.30) gives

$$\begin{aligned} \hat{A}(t, F_D) &= \int_{-\infty}^{\infty} \left( \sum_{m=0}^{M-1} x_p(s - mT) \right) \left( \sum_{n=0}^{M-1} x_p^*(s - t - nT) \right) e^{j2\pi F_D s} ds \\ &= \sum_{m=0}^{M-1} \sum_{n=0}^{M-1} \int_{-\infty}^{\infty} x_p(s - mT) x_p^*(s - t - nT) e^{j2\pi F_D s} ds \end{aligned} \quad (4.71)$$

Substitute  $s' = s - mT$

$$\hat{A}(t, F_D) = \sum_{m=0}^{M-1} e^{j2\pi F_D m T} \sum_{n=0}^{M-1} \int_{-\infty}^{\infty} x_p(s') x_p^*(s' - t - nT + mT) e^{j2\pi F_D s'} ds' \quad (4.72)$$

If the complex ambiguity function of the single simple pulse  $x_p(t)$  is denoted as  $\hat{A}_p(t, F_D)$ , the integral in Eq. (4.72) is  $\hat{A}_p(t + (n-m)T, F_D)$ . Thus

$$\hat{A}(t, F_D) = \sum_{m=0}^{M-1} e^{j2\pi F_D m T} \sum_{n=0}^{M-1} \hat{A}_p(t - (m-n)T, F_D) \quad (4.73)$$

The double sum in Eq. (4.73) is somewhat difficult to deal with. Obviously, all combinations of  $m$  and  $n$  having the same difference  $m - n$  result in the same summand in the second sum, but the dependence of the exponential term on  $m$  only prevents straightforward combining of all such terms. Defining  $n' = m - n$ , it can be shown by simply enumerating all of the combinations that the double summation of some function  $f[m, n]$  can be written (Rihaczek, 1996)

$$\sum_{m=0}^{M-1} \sum_{n=0}^{M-1} f[m, n] = \sum_{n'=-(M-1)}^0 \sum_{m=0}^{M-|n'|-1} f[m, m-n'] + \sum_{n'=1}^{M-1} \sum_{m=0}^{M-|n'|-1} f[m+n', m] \quad (4.74)$$

Applying the decomposition of Eq. (4.74) to Eq. (4.73) gives

$$\begin{aligned} \hat{A}(t, F_D) &= \sum_{n'=-(M-1)}^0 \hat{A}_p(t - n'T, F_D) \sum_{m=0}^{M-|n'|-1} e^{j2\pi F_D m T} \\ &\quad + \sum_{n'=1}^{M-1} e^{j2\pi F_D n' T} \hat{A}_p(t - n'T, F_D) \sum_{m=0}^{M-|n'|-1} e^{j2\pi F_D m T} \end{aligned} \quad (4.75)$$

The geometric series that appears in both halves of the right-hand side of this equation sums to

$$\sum_{m=0}^{M-|n'|-1} e^{j2\pi F_D m T} = \exp[j\pi F_D (M - |n'| - 1)T] \frac{\sin(\pi F_D (M - |n'|)T)}{\sin(\pi F_D T)} \quad (4.76)$$

Using this result in Eq. (4.75) and combining the two remaining sums over  $n'$  into one while renaming the index of summation as  $m$  gives

$$\hat{A}(t, F_D) = \sum_{m=-(M-1)}^{M-1} \hat{A}_p(t - mT, F_D) e^{j\pi F_D (M-1+m)T} \frac{\sin(\pi F_D (M - |m|)T)}{\sin(\pi F_D T)} \quad (4.77)$$

Equation (4.77) expresses the complex ambiguity function of the coherent pulse train in terms of the complex ambiguity function of its constituent simple pulses and the PRI.

Recall that the support in the delay axis of  $\hat{A}_p(t, F_D)$  is  $|t| \leq \tau$ . If  $T > 2\tau$ , which is almost always the case, the replications of  $\hat{A}_p$  in Eq. (4.77) will not overlap and the magnitude of the sum of the terms as  $m$  varies will be equal to the sum of the magnitude of the individual terms. The ambiguity function of the pulse burst waveform can then be written as

$$A(t, F_D) = \sum_{m=-(M-1)}^{M-1} A_p(t - mT, F_D) \left| \frac{\sin(\pi F_D (M - |m|)T)}{\sin(\pi F_D T)} \right| \quad (T > 2\tau) \quad (4.78)$$

To understand this ambiguity function, it is convenient to first look at the zero Doppler and zero delay responses. The zero Doppler response is obtained by setting  $F_D = 0$  in Eq. (4.78) and recalling that  $A_p(t, 0) = 1 - |t|/\tau$ :

$$A(t, 0) = \begin{cases} \sum_{m=-(M-1)}^{M-1} (M - |m|) \left( 1 - \frac{|t - mT|}{\tau} \right), & |t - mT| < \tau \\ 0, & \text{elsewhere} \end{cases} \quad (4.79)$$

Equation (4.79) describes the triangular output of the single-pulse matched filter, repeated every  $T$  seconds and weighted by an overall triangular function  $M - |m|$ . Figure 4.18 illustrates this function for the case  $M = 5$  and  $T = 4\tau$ . The ambiguity function has been normalized by the signal energy  $E$  so that it has a maximum value of 1.0. Note that, as with any waveform, the maximum of the AF occurs at  $t = 0$  and the duration is twice the total waveform duration ( $2MT$  in this case). The local peaks every  $T$  seconds represent the range ambiguities discussed previously in Sec. 4.5.3 and illustrated in Fig. 4.15a. If the transmitted waveform were extended by  $P$  pulses while the reference waveform remained  $M$  pulses long as discussed above, there would be  $P$  consecutive spikes with the full amplitude of 1.0, similar to Fig. 4.16a.

The zero delay cut is obtained by setting  $t = 0$  in Eq. (4.78) and recalling that  $A_p(0, F_D) = |\sin(\pi F_D \tau)/\pi F_D \tau|$  (assuming a unit energy simple pulse), giving

$$A(0, F_D) = \left| \frac{\sin(\pi F_D \tau)}{\pi F_D \tau} \right| \left| \frac{\sin(\pi F_D M T)}{\sin(\pi F_D T)} \right| \quad (4.80)$$

The response is an sinc function with a first zero at  $F_D = 1/MT$  Hz, repeating with a period of  $1/T$  Hz. This basic behavior is weighted by a more slowly varying true sinc function with its first zero at  $1/\tau$  Hz. This structure is evident in Fig. 4.19, which shows a portion of the zero delay cut for the same case with  $M = 5$  and  $T = 4\tau$ . The  $1/T$  spacing of the principal peaks in the zero-delay response is the blind Doppler shift first defined in Chap. 3.

Figure 4.20 is a contour plot of a portion of the complete ambiguity function for this waveform. Note the broadening of the response peaks in Doppler when sampling at the

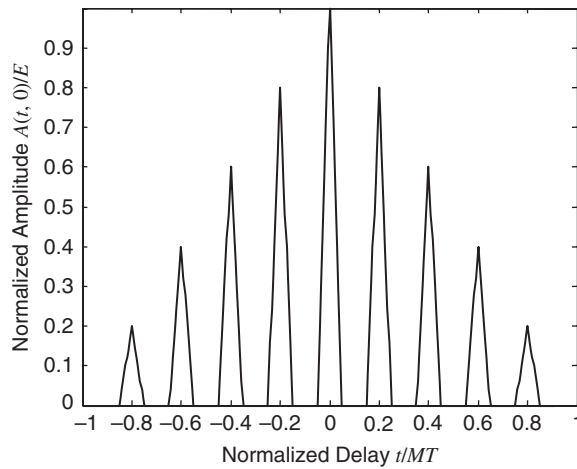


**FIGURE 4.18** Zero-Doppler cut of the ambiguity function of a pulse burst.  $M = 5$  pulses,  $T = 4\tau$ .

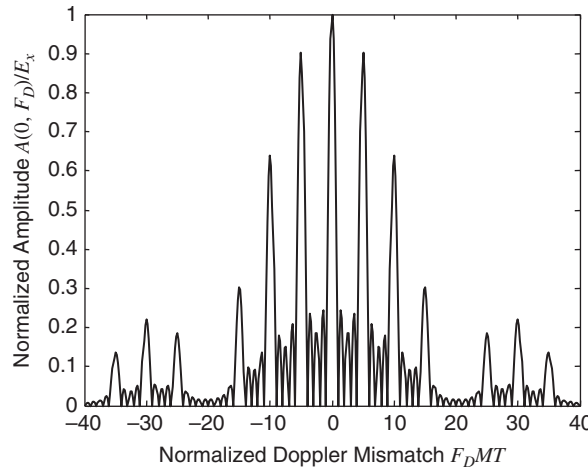


**FIGURE 4.19** Zero-delay cut of the pulse burst ambiguity function with  $M = 5$  and  $T = 4\tau$ .

range-ambiguous delays such as  $4\tau$  and  $8\tau$  (corresponding to  $\pm 0.2$  and  $\pm 0.4$  on the normalized delay scale of the contour plot). This phenomenon is caused by the  $(M - |m|)$  term in the sinc term of Eq. (4.78) and reflects the fact that at these range-ambiguous delays fewer than  $M$  pulses are contributing to the matched filter local output peak. The reduced observation time results in degraded Doppler resolution. Again, if the transmitted waveform were extended by  $P$  pulses, there would be  $P$  consecutive range peaks which retained the full Doppler resolution. This plot also illustrates the breakup of the well-defined peaks in delay when the Doppler mismatch reaches  $1/\tau$  hertz (corresponding to 20 on the normalized Doppler scale of the plot).

Figure 4.21 is a diagram of the structure of the central peak of the pulse burst ambiguity function and the first repeated peaks in Doppler and range. This figure summarizes how the

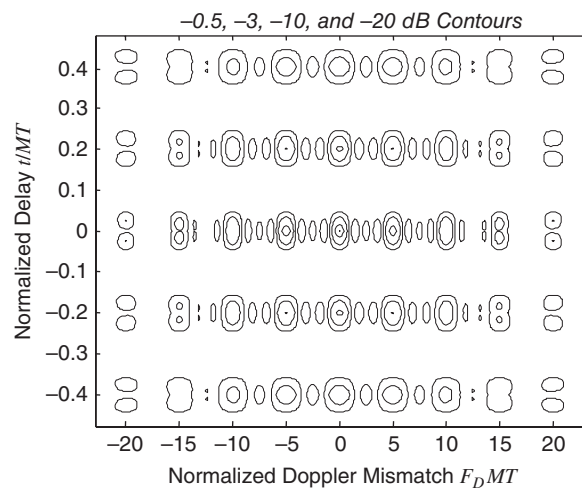


**FIGURE 4.20** A portion of the ambiguity function for the pulse burst waveform with  $M = 5$  and  $T = 4\tau$ . Positive frequencies only shown.

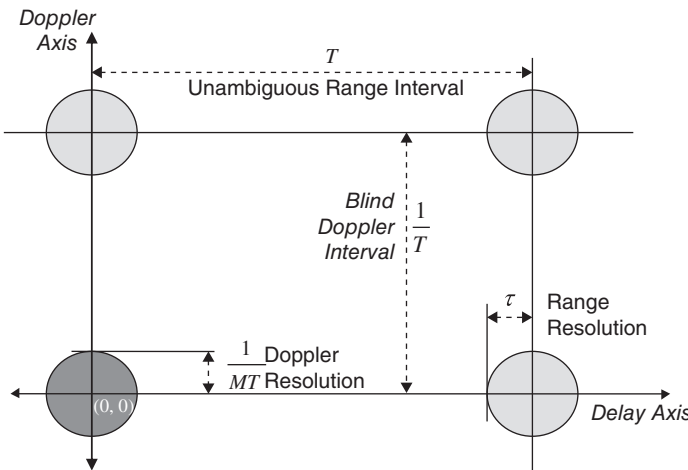


**FIGURE 4.21** Relationship between pulse burst waveform parameters and range and Doppler resolution and ambiguities.

various waveform parameters determine the resolution in range and Doppler, the range ambiguity interval, and the blind Doppler interval. The individual pulse length  $\tau$  is chosen to achieve the desired range resolution ( $c\tau/2$  meters). The pulse repetition interval  $T$  sets the ambiguity interval in range ( $cT/2$  meters) and the blind interval in Doppler ( $1/T$  Hz). Finally, once the PRI is chosen, the number of pulses in the burst determines the Doppler resolution ( $1/MT$  Hz).

#### 4.5.6 The Slow-Time Spectrum and the Periodic Ambiguity Function

It would seem that the DTFT  $Y[l, \omega_D]$  of the slow-time sequence  $y[l, m]$  should be related to the variation of the complex ambiguity function  $\hat{A}(t, F_D)$  in Doppler. The slow-time sequence  $y[l, m]$  is obtained by sampling the output of the simple pulse matched filter output  $s_p(t)$  at the same delay after transmission on each pulse. If the target motion across the CPI is small compared to the range resolution (i.e., the target moves only a small fraction of a range bin during the CPI), the amplitude of the sample taken on each pulse will be the same. This amplitude will be the maximum value  $s_p(0)$  if the sampling time exactly corresponds to the target range; if the sampling time differs from that corresponding to the target range by  $\Delta t$  seconds the measured amplitude on each pulse will be  $s_p(\Delta t)$ . Thus, the slow-time sequence in a given range bin will have constant amplitude but the ambiguity function of the waveform will determine that amplitude based on the alignment of the target range and the range bin sampling times.

If there is relative motion between the radar and target, there will be a sample-to-sample decrease in the phase of the slow-time samples of the form  $-4\pi mvT/\lambda$ . If the target is within the first unambiguous range interval the target echo will be present in all  $M$  slow-time samples for the appropriate range bin and the magnitude of the DTFT will have the  $|\sin(\pi F_D MT)/\sin(\pi F_D T)|$  form seen in Eq. (4.80). However, the  $|\sin(\pi F_D \tau)/\pi F_D \tau|$  term of the AF Doppler response due to the individual pulse shape will not be observed in the DTFT; rather, this term will weight the overall amplitude of the DTFT. Finally, if the target range exceeds  $R_{ua}$  the target echo will not be present in all of the slow-time samples and the Doppler resolution will degrade in  $Y[l, \omega_D]$  in the same manner it did in  $\hat{A}(t, F_D)$ .

When the transmitted pulse burst waveform is extended by  $P$  pulses to provide full integration gain of a factor of  $M$  for targets extending over  $P$  range ambiguities, the matched

filter output maintains its full maximum peak value of  $ME_p$  over the  $P$  range ambiguities (delay interval 0 to  $(P - 1)T$ ) of interest as shown in Fig. 4.16a. The same result over only that delay interval could be obtained by at least two equivalent calculations: correlation of an  $M$ -pulse transmitted waveform with an infinitely extended reference, evaluated over  $[0, (P - 1)T]$ , or circular correlation of an  $M$ -pulse waveform with an  $M$ -pulse reference. The *periodic ambiguity function* (PAF) is a modification of the complex AF of Eq. (4.30) that, when applied to a pulse burst waveform, produces the full-gain AF over this delay interval. A typical definition is (Levanon, 2010; Levanon and Mozeson, 2004)

$$PA(t, F_D) \equiv \left| \int_0^{MT} x(s) \exp(j2\pi F_D s) x^*(s-t) ds \right|, \quad 0 \leq t < P \cdot T \quad (4.81)$$

A significant property of the PAF is its relation to the AF of the single constituent pulse in the pulse burst when  $T > 2\tau$ :<sup>4</sup>

$$PA(t, F_D) = A_p(t, F_D) \left| \frac{\sin(\pi F_D M T)}{\sin(\pi F_D T)} \right|, \quad 0 \leq t < P \cdot T \quad (4.82)$$

That is, the PAF is the AF of the single pulse multiplied by the DTFT of a discrete  $M$ -sample pulse. This is exactly the DTFT  $Y[l, \omega_D]$  that will result from the pulse-by-pulse processing approach as described above.

## 4.6 Frequency-Modulated Pulse Compression Waveforms

A simple pulse has only two parameters, its amplitude  $A$  and its duration  $\tau$ . The range resolution  $c\tau/2$  is directly proportional to  $\tau$ ; better resolution requires a shorter pulse. Most modern radars operate with the transmitter in saturation. That is, any time the pulse is on, its amplitude is kept at the maximum value of  $A$ ; amplitude modulation other than on/off switching is not used. The energy in the pulse is then  $A^2\tau$ . This mode of operation maximizes the pulse energy, which is then also directly proportional to  $\tau$ . As will be seen in Chaps. 6 and 7, increasing pulse energy improves detection and estimation performance. Thus, improving resolution requires a shorter pulse, while improving detection and estimation performance requires a longer pulse. The two metrics are coupled in this unfortunate way because there is effectively only one free parameter  $\tau$  in the design of the simple pulse waveform.

*Pulse compression* waveforms decouple energy and resolution. Recall that a simple pulse has a Rayleigh bandwidth  $\beta = 1/\tau$  Hz and a Rayleigh resolution in time at the matched filter output of  $\tau$  seconds. Thus, the *time-bandwidth product* (BT product) of the simple pulse is  $\tau(1/\tau) = 1$ . A pulse compression waveform, in contrast, has a bandwidth  $\beta$  that is much greater than  $1/\tau$ . Equivalently, it has a duration  $\tau$  much greater than that of a simple pulse with the same bandwidth,  $\tau \gg 1/\beta$ . Either condition is equivalent to stating that a pulse compression waveform has a BT product  $\beta\tau$  much greater than one.

Pulse compression waveforms are obtained by adding frequency or phase modulation to a simple pulse. There are a vast number of pulse compression waveforms in the literature. In this text, only the most commonly used types will be described. These include linear frequency modulation, biphase codes, and certain polyphase codes. Nonlinear FM will also be briefly introduced. Many other waveforms are described in Levanon and Mozeson (2004) and Keel and Baden (2012).

<sup>4</sup>A slightly more complicated version of this result holds when  $T \leq 2\tau$ , see (Levanon and Mozeson, 2004).

### 4.6.1 Linear Frequency Modulation

A linear frequency modulated waveform is defined by

$$x(t) = \cos\left(\pi \frac{\beta}{\tau} t^2\right), \quad 0 \leq t \leq \tau \quad (4.83)$$

The complex equivalent is

$$x(t) = e^{j\pi\beta t^2/\tau} = e^{j\theta(t)} \quad 0 \leq t \leq \tau \quad (4.84)$$

The instantaneous frequency in hertz of this waveform is the time derivative of the phase function

$$F_i(t) = \frac{1}{2\pi} \frac{d\theta(t)}{dt} = \frac{\beta}{\tau} t \text{ hertz} \quad (4.85)$$

This function is shown in Fig. 4.22, assuming  $\beta > 0$ .  $F_i(t)$  sweeps linearly across a total bandwidth of  $\beta$  Hz during the  $\tau$ -second pulse duration. The waveform  $x(t)$  [Eq. (4.83), or the real part of Eq. (4.84)] is shown in Fig. 4.23 for  $\beta\tau = 50$ . The LFM waveform is often called a *chirp* waveform in analogy to the sound of an acoustic sinusoid with a linearly changing frequency. When  $\beta$  is positive the pulse is an *upchirp*; if  $\beta$  is negative it is a *downchirp*.

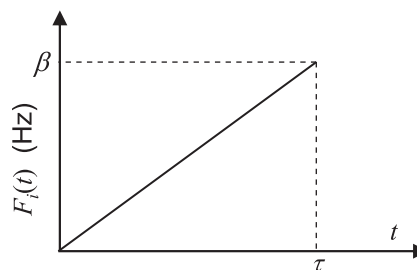


**FIGURE 4.22** Instantaneous frequency of an LFM pulse.

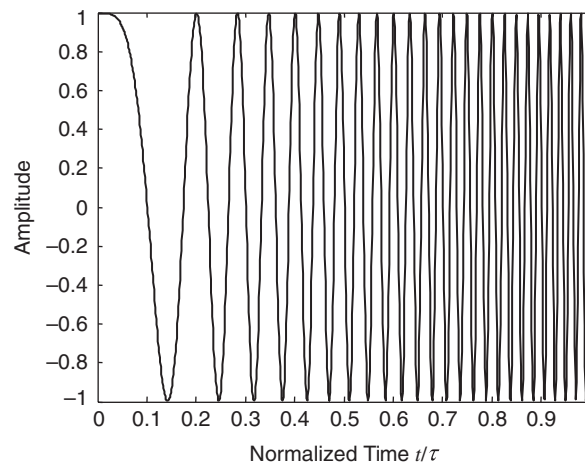


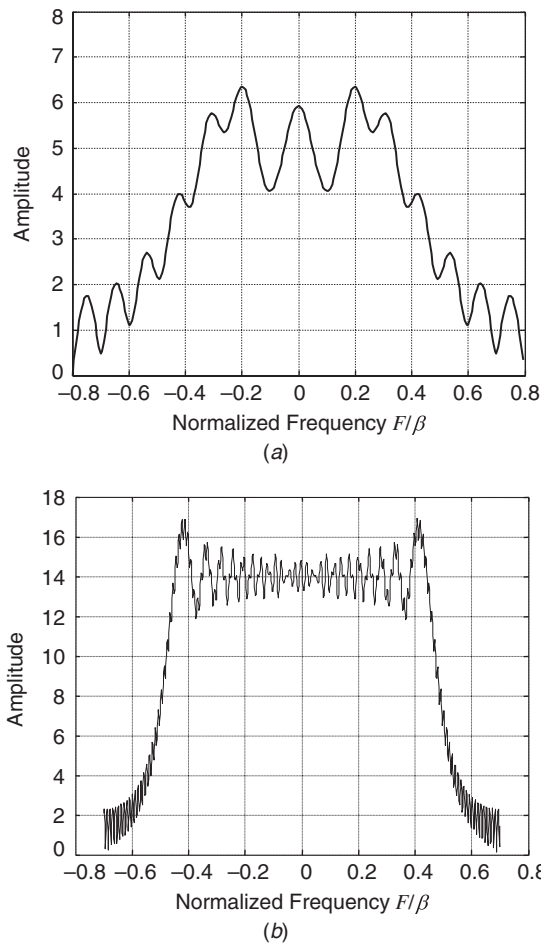
**FIGURE 4.23** Real-valued LFM upchirp waveform, BT product  $\beta\tau = 50$ .

The BT product of the LFM pulse is simply  $\beta\tau$ ;  $\beta\tau \gg 1$  if the LFM pulse is to qualify as a pulse compression waveform.

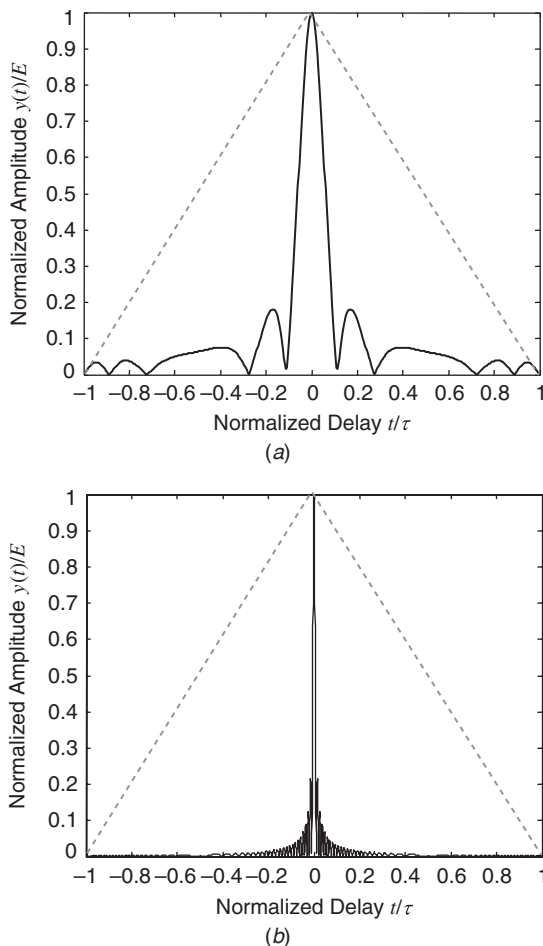
Figure 4.24 shows the magnitude spectrum of the LFM waveform for a relatively low BT product case ( $\beta\tau = 10$ ), and again for a higher BT product case ( $\beta\tau = 100$ ). For low BT the spectrum is relatively poorly defined. As the BT product increases the spectrum takes on a more rectangular shape. This is intuitively reasonable: because the sweep is linear, the waveform spreads its energy uniformly across the spectrum.

Figure 4.25 shows the output of the matched filter for the same two chirp waveforms. The dotted line superimposed on the output waveform is the output of a matched filter for a simple pulse of the same duration. As always, the total duration of the matched filter output is  $2\tau$  seconds. In both cases, the LFM waveform results in a matched filter output with a Rayleigh resolution much narrower than  $\tau$ . In fact, the Rayleigh resolution is very nearly  $1/\beta$  in each case (this will be confirmed shortly), an improvement over the simple pulse by a factor of the time-bandwidth product  $\beta\tau$ .

Simple and LFM pulses of the same amplitude and duration will have the same peak power at the matched filter output and achieve the same output SNR in accordance with Eq. (4.13).



**FIGURE 4.24** Magnitude spectrum of an LFM waveform: (a)  $\beta\tau = 10$ , (b)  $\beta\tau = 100$ .



**FIGURE 4.25** Output of matched filter for an LFM waveform: (a)  $\beta\tau = 10$ , (b)  $\beta\tau = 100$ . The dotted line is the output of a matched filter for a simple pulse of the same duration.

However, for an LFM pulse and a simple pulse of the same amplitude to have the same fast-time Rayleigh resolution at the output of their matched filters, the simple pulse must be shorter than the LFM pulse by the factor  $\beta\tau$ . The energy in the simple pulse and the SNR achieved are then also less by the factor of  $\beta\tau$ . In other words, the LFM waveform with proper matched filtering achieves a signal processing gain of  $G_{sp} = \beta\tau$  compared to a simple pulse of the same Rayleigh resolution.

Unlike the simple pulse case, the matched filter output for the LFM pulse exhibits a sidelobe structure. Figure 4.26 expands the central portion of Fig. 4.25b, showing the distinctly sinc-like mainlobe and first few sidelobes. This should not be surprising: the waveform spectrum  $X(F)$  (Fig. 4.24b) is approximately a rectangle of width  $\beta$  Hz. Consequently, the spectrum of the matched filter output,  $|X(F)|^2$ , will also be approximately a rectangle of width  $\beta$ . The time-domain output of the matched filter is therefore expected to be approximately a sinc function with a Rayleigh resolution of  $1/\beta$  seconds.

To summarize, the LFM waveform enables separate control of pulse energy (through its duration) and range resolution (through its swept bandwidth). The possibility of pulse

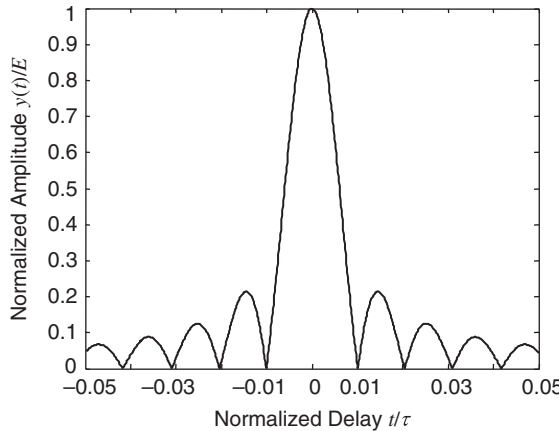


**FIGURE 4.26** Expanded view of central portion of Fig. 4.25b.

compression is created by the use of matched filters. The output of the matched filter is not a replica of the transmitted waveform  $x(t)$ , but of its autocorrelation function  $s_x(t)$ . Therefore, if a waveform can be designed that has a long duration but a narrowly concentrated autocorrelation, both good range resolution and good energy can be obtained simultaneously. This in turn is accomplished by modulating a long pulse to spread its bandwidth beyond the usual  $1/\tau$ . Since the spectrum of the autocorrelation function is just the squared magnitude of the waveform spectrum, a spectrum spread over  $\beta$  Hz will tend to produce a filter output with most of its energy concentrated in a mainlobe of about  $1/\beta$  seconds duration. The linear FM pulse is the first example of such a waveform, but phase coded waveforms will provide more examples of this approach.

#### 4.6.2 The Principle of Stationary Phase

The Fourier transform of Eq. (4.84) is a relatively complicated result involving the sine integral  $\text{Si}(F)$  (Rihaczek, 1996). A very useful and much simpler approximation can be derived using the *principle of stationary phase* (PSP), an advanced technique in Fourier analysis. The PSP is useful for approximate evaluation of integrals with highly oscillatory integrands; thus, it applies particularly well to Fourier transforms. Write  $x(t)$  in amplitude and phase form,  $x(t) = A(t) \exp[j\theta(t)]$ , and consider its Fourier transform

$$X(\Omega) = \int_{-\infty}^{+\infty} \underbrace{A(t) e^{j\theta(t)}}_{x(t)} e^{-j\Omega t} dt \quad (4.86)$$

Define the phase  $\phi(t, \Omega)$  of the Fourier integral as the combination of the signal phase and the Fourier kernel phase

$$\begin{aligned} X(\Omega) &= \int_{-\infty}^{+\infty} A(t) e^{j\theta(t)} e^{-j\Omega t} dt = \int_{-\infty}^{+\infty} A(t) e^{j[\theta(t) - \Omega t]} dt \\ &\equiv \int_{-\infty}^{+\infty} A(t) e^{j\phi(t, \Omega)} dt \end{aligned} \quad (4.87)$$

Of course, the exact Fourier transform is known for many signals having relatively simple phase functions  $\tau(t)$ . The PSP is most useful when the signal phase function and thus the total integral phase  $\phi(t, \Omega)$  is continuous but nonlinear or otherwise complicated.

Define a *stationary point* of the integrand as a value of  $t = t_0$  such that the first time derivative of the integral phase  $\phi'(t_0, \Omega) = 0$ . Then the PSP approximation to the spectrum is (Born and Wolf, 1959; Papoulis and Pillai, 2002; Raney, 1992)

$$X(\Omega) \approx \sqrt{\frac{-2\pi}{\phi''(t_0, \Omega)}} e^{-j\pi/4} A(t_0) e^{j\phi(t_0, \Omega)} \quad (4.88)$$

where  $\phi''(t_0, \Omega)$  is the second time derivative of  $\phi(t, \Omega)$  evaluated at  $t = t_0$ . If there are multiple stationary points the spectrum is the sum of such terms for each stationary point. Equation (4.88) states that the magnitude of the spectrum at a given frequency  $\Omega$  is proportional to the amplitude of the signal envelope at the time that the stationary point occurs and, more importantly, is inversely proportional to the square root of the rate of change of the frequency  $\phi''(t_0, \Omega)$  at that time. The PSP also implies that only the stationary points significantly influence  $X(\Omega)$ .

The PSP can be applied to estimate the spectrum of the LFM waveform. The waveform is defined as

$$x(t) = A(t) e^{j\alpha t^2}, \quad A(t) = \begin{cases} 1, & -\tau/2 \leq t \leq +\tau/2 \\ 0, & \text{otherwise} \end{cases}, \quad \alpha \equiv \pi \frac{\beta}{\tau} \quad (4.89)$$

Thus

$$X(\Omega) = \int_{-\infty}^{+\infty} x(t) e^{-j\Omega t} dt = \int_{-\infty}^{+\infty} A(t) e^{j(\alpha t^2 - \Omega t)} dt \quad (4.90)$$

The integrand phase and its derivatives are then

$$\begin{aligned} \phi(t, \Omega) &= \alpha t^2 - \Omega t \\ \phi'(t, \Omega) &= 2\alpha t - \Omega \\ \phi''(t, \Omega) &= 2\alpha \end{aligned} \quad (4.91)$$

The stationary points are found by setting  $\phi'(t, \Omega) = 0$  and solving for  $t$ . In this case, there is only one stationary point:

$$0 = \phi'(t_0, \Omega) \Rightarrow t_0 = \frac{\Omega}{2\alpha} \quad (4.92)$$

Inserting Eq. (4.92) into Eq. (4.88) gives

$$\begin{aligned} X(\Omega) &\approx \sqrt{\frac{-2\pi}{\phi''(t_0, \Omega)}} e^{-j\pi/4} A(t_0) e^{j\phi(t_0, \Omega)} \\ &= \sqrt{\frac{-2\pi}{2\alpha}} e^{-j\pi/4} A\left(\frac{\Omega}{2\alpha}\right) e^{j[\alpha(\Omega/2\alpha)^2 - \Omega(\Omega/2\alpha)]} \\ &= j\sqrt{\frac{\pi}{\alpha}} e^{-j\pi/4} A\left(\frac{\Omega}{2\alpha}\right) e^{-j\Omega^2/4\alpha} \end{aligned} \quad (4.93)$$

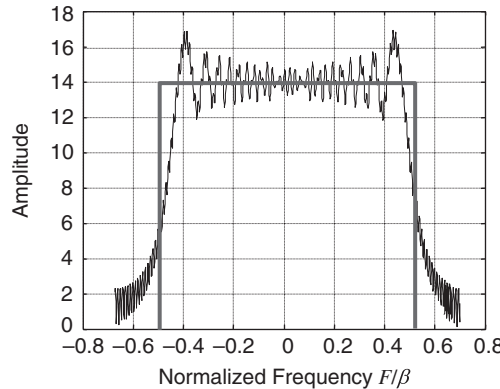


**FIGURE 4.27** Comparison of actual magnitude spectrum and PSP approximation for an LFM pulse with  $\beta\tau = 100$ .

Recalling the finite support of the signal envelope  $A(t)$ , the term  $A(\Omega/2\alpha)$  becomes (using  $\alpha = \pi\beta/\tau$ )

$$A\left(\frac{\Omega}{2\alpha}\right) = \begin{cases} 1, & -\tau/2 \leq \frac{\Omega}{2\alpha} \leq +\tau/2 \\ 0, & \text{otherwise} \end{cases} \Rightarrow \quad (4.94)$$

$$A\left(\frac{\Omega}{2\alpha}\right) = \begin{cases} 1, & -2\pi\left(\frac{\beta}{2}\right) \leq \Omega \leq +2\pi\left(\frac{\beta}{2}\right) \\ 0, & \text{otherwise} \end{cases}$$

The final result is

$$X(\Omega) \approx j\sqrt{\frac{\pi}{\alpha}} e^{-j\pi/4} e^{-j\Omega^2/4\alpha}, \quad -2\pi\left(\frac{\beta}{2}\right) \leq \Omega \leq +2\pi\left(\frac{\beta}{2}\right) \quad (4.95)$$

Figure 4.27 compares this approximation with the exact spectrum when  $\beta\tau = 100$ . Equation (4.95) estimates that  $|X(\Omega)|$  is constant over the range  $\pm\beta/2$  Hz and is zero outside of this range. This is both intuitively satisfying, since this is exactly the range over which the instantaneous frequency of the LFM pulse sweeps, and consistent with the increasingly rectangular shape of the exact spectrum observed in Fig. 4.23 as the BT product increases. The PSP result also gives an estimate of the phase of the spectrum which, like the temporal phase of the waveform  $x(t)$ , is seen to be quadratic in frequency.

#### 4.6.3 Ambiguity Function of the LFM Waveform

The ambiguity function of an LFM pulse can be obtained by direct calculation, similar to the simple pulse, but with a good deal more tedium. An easier way is to introduce the “chirp property” of the ambiguity function and then apply it to the LFM case. Suppose that a waveform  $x(t)$  has an ambiguity function  $A(t, F_D)$ . Create a modified waveform  $x'(t)$  by

modulating  $x(t)$  with a linear FM complex chirp and compute its complex ambiguity function

$$\begin{aligned}
 x'(t) &\equiv x(t)e^{j\pi\beta t^2/\tau} \\
 \hat{A}'(t, F_D) &= \int_{-\infty}^{\infty} x'(s)x'^*(s-t)e^{j2\pi F_D s} ds \\
 &= \int_{-\infty}^{\infty} x(s)e^{j\pi\beta s^2/\tau}x^*(s-t)e^{-j\pi\beta(s-t)^2/\tau}e^{j2\pi F_D s} ds \\
 &= e^{-j\pi\beta t^2/\tau} \int_{-\infty}^{\infty} x(s)x^*(s-t)e^{j2\pi(F_D + \beta t/\tau)s} ds \\
 &= e^{-j\pi\beta t^2/\tau} \hat{A}\left(t, F_D + \frac{\beta}{\tau}t\right)
 \end{aligned} \tag{4.96}$$

Taking the magnitude of  $\hat{A}'(t, F_D)$  gives the ambiguity function of the chirp signal in terms of the ambiguity function of the original signal without the chirp

$$A'(t, F_D) = A\left(t, F_D + \frac{\beta}{\tau}t\right) \tag{4.97}$$

Equation (4.97) states that adding a chirp modulation to a signal skews its ambiguity function in the delay-Doppler plane. Applying this property to the simple pulse AF [Eq. (4.51)] gives the AF of the LFM waveform

$$\begin{aligned}
 A(t, F_D) &= \left(1 - \frac{|t|}{\tau}\right) \left| \frac{\sin[\pi(F_D + \beta t/\tau)\tau(1 - |t|/\tau)]}{\pi(F_D + \beta t/\tau)\tau(1 - |t|/\tau)} \right| \\
 &= \left(1 - \frac{|t|}{\tau}\right) \left| \frac{\sin[\pi(F_D\tau + \beta t)(1 - |t|/\tau)]}{\pi(F_D\tau + \beta t)(1 - |t|/\tau)} \right|, \quad -\tau \leq t \leq \tau
 \end{aligned} \tag{4.98}$$

Figure 4.28 is a contour plot of the AF of an LFM pulse of duration  $\tau = 10 \mu\text{s}$  and swept bandwidth  $\beta = 1 \text{ MHz}$ ; thus, the BT product is 10. The AF retains the triangular ridge of the simple pulse but is now skewed in the delay-Doppler plane as predicted by Eq. (4.97).

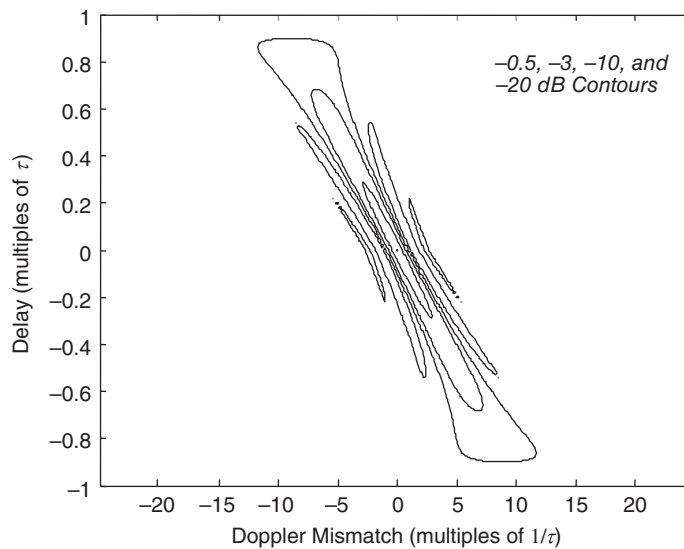


**FIGURE 4.28** Contour plot of the ambiguity function of an LFM waveform with  $\beta\tau = 10$ .

The zero-Doppler cut of the LFM ambiguity function is the matched filter output when there is no Doppler mismatch:

$$A(t, 0) = \left| \frac{\sin[\pi\beta t(1 - |t|/\tau)]}{\pi\beta t} \right|, \quad -\tau \leq t \leq \tau \quad (4.99)$$

This function was illustrated for BT products of both 10 and 100 in Fig. 4.25. The Rayleigh resolution of the LFM pulse is obtained by examination of Eq. (4.99). The peak of  $A(t, 0)$  occurs at  $t = 0$ . The first zero occurs when the argument of the numerator equals  $\pi$ , which occurs when  $\beta t(1 - |t|/\tau) = 1$ . For positive  $t$ , this becomes

$$\beta t - \frac{\beta t^2}{\tau} = 1 \quad \Rightarrow \quad t^2 - \tau t + \tau/\beta = 0 \quad (4.100)$$

The roots of this equation are  $t = (\tau \pm \sqrt{\tau^2 - 4\tau/\beta})/2 = \tau(1 \pm \sqrt{1 - 4/\beta\tau})/2$ . Since the argument of the square root in the last expression is less than one, taking the negative sign gives the positive root closest to zero and thus the Rayleigh resolution in time. This result can be simplified with the following series expansion of the square root

$$\begin{aligned} \sqrt{1-x} &= 1 - \frac{x}{2} - \frac{x^2}{8} - \dots \approx 1 - \frac{x}{2} \quad (x \ll 1) \quad \Rightarrow \\ t &\approx \frac{\tau}{2} \left[ 1 - \left( 1 - \frac{2}{\beta\tau} \right) \right] \approx \frac{1}{\beta} \quad (\beta\tau \gg 1) \end{aligned} \quad (4.101)$$

Thus, the Rayleigh resolution in time is approximately  $1/\beta$  seconds, corresponding to a Rayleigh range resolution  $\Delta R$  of

$$\Delta R = \frac{c}{2\beta} \quad \text{m} \quad (4.102)$$

The zero-delay response is

$$A(0, F_D) = \left| \frac{\sin(\pi F_D \tau)}{\pi F_D \tau} \right| \quad (4.103)$$

which is simply a standard sinc function. The Doppler resolution of the LFM pulse is the same as that of a simple pulse, namely

$$\Delta F_D = \frac{1}{\tau} \quad \text{Hz} \quad (4.104)$$

Equation (4.103) shows that, like the simple pulse, the Doppler resolution of an LFM pulse is inversely proportional to the pulse length. Furthermore, the energy in the LFM pulse is still  $A^2\tau$ , directly proportional to the pulse length. Equation (4.102) shows that, unlike the simple pulse, the range resolution is inversely proportional to the swept bandwidth. The LFM waveform has two parameters, bandwidth and duration, which can now be used to independently control pulse energy and range resolution. The pulse length is chosen (along with the pulse amplitude  $A$ ) to set the desired energy, while the swept bandwidth is chosen to obtain the desired range resolution.

The expression  $c/2\beta$  for range resolution is quite general. For instance, the Rayleigh bandwidth of a simple pulse is  $\beta = 1/\tau$  Hz; using this in  $c/2\beta$  gives  $\Delta R = c\tau/2$  as before. While bandwidth and pulse length are directly related in the simple pulse, modulation of the LFM waveform has decoupled them. If  $\beta\tau > 1$  for the LFM pulse the range resolution will be better

than that of a simple pulse of the same duration by the factor  $\beta\tau$ . Alternatively, the range resolution of a simple pulse of length  $\tau$  can be matched by an LFM pulse that is longer (and thus higher energy, given the same transmitted power) by the factor  $\beta\tau$ .

#### 4.6.4 Range-Doppler Coupling

The skew in the ambiguity function for the LFM pulse gives rise to an interesting phenomenon. Consider the AF of Eq. (4.98). The peak of this sinc-like function will occur when

$$F_D + \frac{\beta}{\tau}t = 0 \quad \Rightarrow \quad t = -\frac{\tau F_D}{\beta} \quad (4.105)$$

That is, when there is a Doppler mismatch the peak of the matched filter output will not occur at  $t = 0$  as desired. Instead, it will be shifted by an amount proportional to the Doppler shift. Because the target range will be estimated based on the time of occurrence of this peak, a Doppler mismatch will induce an error in measuring range. The corresponding range error will be

$$\delta R = -\frac{c\tau F_D}{2\beta} \quad (4.106)$$

The amplitude of the peak will also be reduced by the factor  $(1 - |t|/\tau) = (1 - F_D/\beta)$ . Figure 4.29 illustrates the skewed ridge of the LFM ambiguity function and the relationship between Doppler shift and range measurement error.

While an incorrect range measurement is certainly undesirable, range-Doppler coupling is a useful phenomenon in some systems. A simple pulse with duration  $\tau$  will have a Doppler Rayleigh resolution of  $1/\tau$  Hz; targets with Doppler mismatches approaching this value or larger will produce a greatly attenuated output from the matched filter and will likely go undetected. An LFM pulse of the same duration will still produce a significant output peak for a much broader range of Doppler shifts, even though the peak will be mislocated in range. Nonetheless, the target will be more likely to be detected. The LFM waveform is said to be more *Doppler tolerant* than the simple pulse. This makes it a good choice for surveillance applications because a relatively large range of Doppler shifts can be searched with an LFM pulse. The range error can be eliminated, at least for isolated targets, by repeating the measurements with an LFM pulse of the opposite slope, e.g., an upchirp followed by a downchirp. In this case the sign of the range error will be reversed. Averaging the two measurements will give the true range and also allow determination of the Doppler shift.

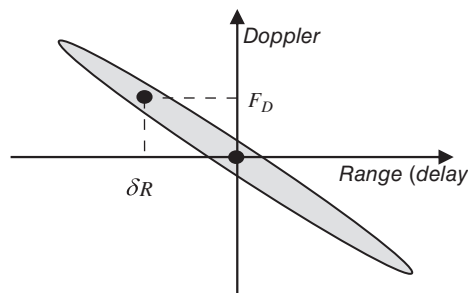


**FIGURE 4.29** Illustration of the effect of range-Doppler coupling on apparent target range.

### 4.6.5 Stretch Processing

LFM waveforms are often the waveform of choice for exceptionally wideband radar systems where the swept bandwidth  $\beta$  may be hundreds of megahertz or even exceed 1 GHz. Digital processing can be difficult to implement in such systems because the high instantaneous bandwidth of the waveform requires equally high sampling rates in the A/D converter. It is difficult to obtain high-quality A/D converters at these rates with wordlengths longer than perhaps 8 bits with current technology; wordlengths at 1 GHz are expected to reach only about 11 bits by 2020 (Jonsson, 2010). In addition, the sheer number of samples generated can be stressing for the signal processor.

*Stretch processing* is a specialized technique for matched filtering of wideband LFM waveforms. It is also called *deramp processing*, *deramp on receive*, *dechirp*, and *one-pass processing*. It is essentially the same as the processing used with linear frequency-modulated continuous wave (FMCW) radar. Stretch processing is most appropriate for applications seeking very fine range resolution over relatively short range intervals (called *range windows* or *range swaths*).

Figure 4.30 shows the scenario for analyzing stretch processing. The *central reference point* (CRP) is in the middle of the range window of interest at a range of  $R_0$  meters, corresponding to a time delay of  $t_0$  seconds. Consider a scatterer at range  $R_b$  and time delay  $t_b = t_0 + \delta t_b$ . The problem will be analyzed in terms of differential range or delay relative to the CRP, denoted  $\delta R_b$  and  $\delta t_b$ . The transmitted waveform is the LFM pulse of Eq. (4.84). The echo from the scatterer, with the carrier frequency included, is

$$\bar{x}(t) = \rho \exp\left[j\pi \frac{\beta}{\tau} (t - t_b)^2\right] \exp[j\Omega(t - t_b)], \quad 0 \leq t - t_b \leq \tau \quad (4.107)$$

where  $\rho$  is proportional to the scatterer reflectivity. This echo is processed with the modified coherent receiver in complex equivalent form shown in Fig. 4.31. The unique aspects of this stretch receiver are the reference oscillator and the Fourier transform. The oscillator contains a conventional term  $\exp(-j\Omega t)$  to remove the carrier. However, it also contains a replica of the transmitted chirp, referenced to the time delay  $t_0$  corresponding to the CRP. The reason for the Fourier transform will be apparent shortly.

After some algebra and using  $t_b = t_0 + \delta t_b$ , the output  $y(t)$  can be expressed as

$$y(t) = \rho \exp\left(-j\frac{4\pi R_b}{\lambda}\right) \exp\left[-j2\pi \frac{\beta}{\tau} \delta t_b(t - t_0)\right] \exp\left[j\pi \frac{\beta}{\tau} (\delta t_b)^2\right], \quad t_0 \leq t - \delta t_b \leq t_0 + \tau \quad (4.108)$$

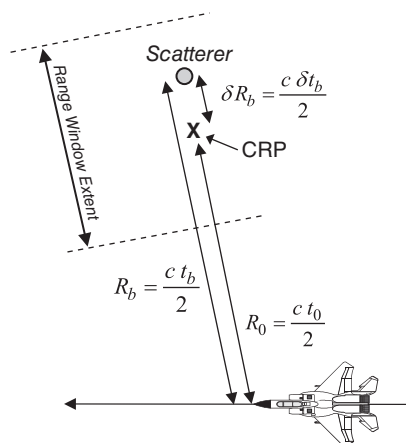


FIGURE 4.30 Scenario for stretch processing analysis.

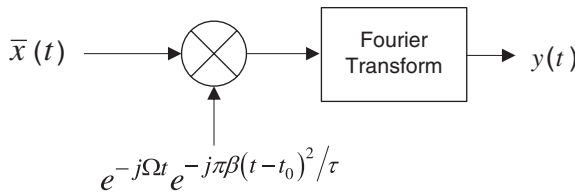


FIGURE 4.31 Complex equivalent receiver for stretch processor.

The phase term that is quadratic in  $\delta t_b$  is a complex constant. In synthetic aperture imaging it is called the *residual video phase* (RVP). The middle complex exponential contains a term that is linear in  $t$  and therefore represents a constant-frequency complex sinusoid. By inspection, the sinusoid frequency is  $F_b = -\beta \delta t_b / \tau$  Hz.  $F_b$  is proportional to  $\delta t_b$  and thus to the range of the scatterer relative to the CRP. The differential range can be obtained from the mixer output frequency as

$$\delta R_b = -\frac{c F_b \tau}{2\beta} \quad (4.109)$$

Heuristically, the scatterer produces a constant frequency tone at the output of the stretch receiver because the receiver not only removes the carrier from the LFM echo but also combines it in a mixer with a replica of the LFM with a delay corresponding to the CRP. In the conventional real-signal receiver of Fig. 1.13, the mixer produces sum and difference “beat” frequencies. The sum frequency is removed by a lowpass filter. (This LPF is not needed in the complex representation and is therefore not shown in Fig. 4.31.) The difference frequency is the difference between the instantaneous frequency of the LFM echo and the LFM reference. Since both have the same sweep rate, this beat frequency is a constant.

If there are several scatterers distributed at ranges  $R_i$  and delays  $\delta t_i$ , the stretch receiver output is simply the superposition of several terms of the form of Eq. (4.108)

$$y(t) = \sum_i \rho_i \exp\left(-j\frac{4\pi R_i}{\lambda}\right) \exp\left[-j2\pi\frac{\beta}{\tau}\delta t_i(t-t_0)\right] \exp\left[j\pi\frac{\beta}{\tau}(\delta t_i)^2\right] \quad (4.110)$$

Thus the output of the stretch receiver contains a different beat frequency tone for each scatterer. The reason for the Fourier transform block in Fig. 4.31 is now apparent. Spectral analysis of  $y(t)$  can identify the beat frequencies present in the mixer output and therefore the ranges and amplitudes of the scatterers present in the composite echo. Figure 4.32 illustrates the instantaneous frequencies and timing of the signals involved for three scatterers, one in the middle and one at each edge of the scene.

It is desirable that the reference LFM chirp completely overlap the echo from a scatterer anywhere within the range window. If the range window is  $R_w = c T_w / 2$  meters long the leading edge of the echo from a scatterer at the nearest range,  $R_0 - R_w / 2$ , will arrive  $t_0 - T_w / 2$  seconds after transmission as shown in Fig. 4.32. The trailing edge of the echo from the scatterer at the far limit of the range window,  $R_0 + R_w / 2$ , will arrive  $t_0 + T_w / 2 + \tau$  seconds after transmission. Thus, data from the range window have a total duration of  $T_w + \tau$  seconds. To ensure complete overlap of the reference chirp with echoes from any part of the range window the reference chirp must be  $T_w + \tau$  seconds long and so will sweep over  $(1 + T_w / \tau)\beta$  Hz.

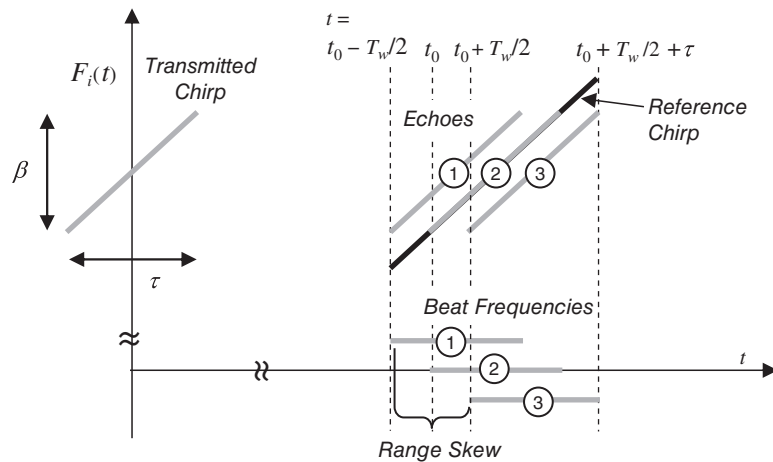


**FIGURE 4.32** Instantaneous frequency vs. time for an LFM transmitted pulse and echoes from three scatterers. See text for details.

Another issue evident in Fig. 4.32 is *range skew*. This is the phenomenon whereby the beat frequencies for scatterers at different ranges, while all of the same duration (provided the reference chirp is lengthened), start and stop at different times. This complicates weighting of the mixer output prior to spectral analysis for range sidelobe control. If the window is aligned with the beat frequency for the center scatterer response, it will be misaligned with earlier and later scatterer responses. If it is lengthened to cover the full mixer output duration of  $T_w + \tau$  seconds, none of the beat frequencies will be weighted by the full window and each will have a different effective window function. In either case, sidelobe suppression will be poor.

This problem can be solved by placing an additional filter between the mixer output and the Fourier transform. Notice that the scatterer at delay  $\delta t_b$  relative to the patch center generates a beat frequency of  $-\beta \cdot \delta t_b / \tau$  Hz. What is needed is a filter whose frequency response has unit magnitude for all frequencies so as not to distort the scatterer amplitudes, but also a *group delay*<sup>5</sup> of  $-\delta t_b$  seconds at the frequency  $-\beta \cdot \delta t_b / \tau$ . It can be shown that the required frequency response in analog radian frequency units is  $H(\Omega) = \exp(-j\Omega^2 \tau^2 / 2\beta_\Omega)$ , which has unit magnitude for all frequencies and a quadratic phase in the frequency domain (see Prob. 15). All of the beat frequencies will be aligned in time at the output of this filter. As an extra benefit, this filter also corrects RVP (Carrara et al., 1995).

The bandwidth of the stretch receiver output can be obtained by considering the difference in beat frequencies for scatterers at the near and far edges of the range window. This gives

$$\begin{aligned} F_{\text{near}} - F_{\text{far}} &= \left[ -\frac{\beta}{\tau} \left( -\frac{T_w}{2} \right) \right] - \left[ -\frac{\beta}{\tau} \left( +\frac{T_w}{2} \right) \right] \\ &= \frac{T_w}{\tau} \beta \end{aligned} \quad (4.111)$$

<sup>5</sup>Group delay in seconds is the negative of the derivative of the frequency-domain phase function  $\Phi(\Omega)$  of  $H(\Omega) = |H(\Omega)| \exp[j\Phi(\Omega)]$  with respect to  $\Omega$ . It is a measure of the filter delay for inputs of a given frequency. See Oppenheim and Schafer (2010).

If  $T_w < \tau$ , the bandwidth at the receiver output is less than the original signal bandwidth  $\beta$ . The mixer output can then be sampled with slower A/D converters and the number of range samples needed to represent the range window data is reduced. Thus, the stretch technique is most effective for systems performing fine range resolution analysis over limited range windows. Also note that while the digital processing rates have been reduced, the analog receiver hardware up through the LFM mixer must still be capable of handling the full instantaneous signal bandwidth.

As an example, consider a 100  $\mu\text{s}$  pulse with a swept bandwidth of 750 MHz, giving a BT product of 75,000. Suppose the desired range window is  $R_w = 1.5$  km, corresponding to a sampling window of  $T_w = 10 \mu\text{s}$ . In a conventional receiver the sampling rate will be 750 megasamples per second. Data from scatterers over the extent of the range window will extend over  $T_w + \tau$  seconds, requiring  $(750 \text{ MHz})(10 \mu\text{s} + 100 \mu\text{s}) = 82,500$  samples to represent the range window. In contrast, the bandwidth at the output of the stretch receiver will be  $(T_w/\tau)\beta = 75 \text{ MHz}$ . The sampled time interval remains the same, so only 8250 samples are required. Restricting the analysis to a delay window one-tenth the length of the pulse and using the stretch technique has resulted in a factor of 10 reduction in both the sampling rate required and the number of samples to be digitally processed.

Stretch processing of linear FM waveforms preserves both the resolution and the range-Doppler coupling properties of conventionally processed LFM. Consider the output of the stretch mixer for a scatterer at differential range  $\delta t_b$  from the central reference point. This signal will be a complex sinusoid at a frequency  $F_b = -\beta \cdot \delta t_b / \tau$  Hz observed for a duration of  $\tau$  seconds. In the absence of windowing, the Fourier transform of this signal will be a sinc function with its peak at  $F_b$  and a Rayleigh resolution of  $1/\tau$  Hz. The processor will be able to resolve scatterers whose beat frequencies are at least  $\Delta F_b = 1/\tau$  Hz apart. The time-delay spacing that gives this frequency separation satisfies

$$\frac{1}{\tau} = \left| \frac{\beta}{\tau} \delta t_b \right| \Rightarrow \delta t_b = \frac{1}{\beta} \quad (4.112)$$

The corresponding range separation is then the usual result for range resolution

$$\delta R_b = \frac{c}{2} \delta t_b = \frac{c}{2\beta} \quad (4.113)$$

If the reference oscillator sweep is not lengthened as discussed above to fully overlap the echo from scatterers at any location in the range window, the range resolution will be degraded. Specifically, the duration  $\tau'$  of the beat frequency will be less than  $\tau$  seconds for scatterers at any delay other than the center of the window due to the incomplete overlap. The Rayleigh resolution of the Fourier transform of that scatterer's beat frequency will increase to a value  $1/\tau' > 1/\tau$ , causing the range resolution of Eq. (4.113) to increase proportionately. The processing gain will similarly be reduced from the ideal factor of  $\beta\tau$ .

To consider the effect of Doppler shift on the stretch processor, replace  $\bar{x}(t)$  in Eq. (4.107) with

$$\bar{x}(t) = \rho \exp \left[ j\pi \frac{\beta}{\tau} (t - t_b)^2 \right] \exp(j2\pi F_D t) \exp[j\Omega(t - t_b)], \quad 0 \leq t - t_b \leq \tau \quad (4.114)$$

Repeating the previous analysis, Eq. (4.108) becomes

$$y(t) = \rho \exp \left( -j \frac{4\pi R_b}{\lambda} \right) \exp \left[ -j2\pi \left( \frac{\beta}{\tau} \delta t_b - F_D \right) t - 2\pi \frac{\beta}{\tau} \delta t_b t_0 \right] \exp \left[ j\pi \frac{\beta}{\tau} (\delta t_b)^2 \right] \quad (4.115)$$

Equation (4.115) shows that the effect of a Doppler shift is to increase the beat frequency  $F_b$  by  $F_D$  Hz. Since beat frequency is mapped to differential range by the stretch processor according to  $\delta R_b = -cF_b\tau/2\beta$ , this implies a measured range shift of

$$\delta R = -\frac{c\tau}{2\beta} F_D \quad \text{m} \quad (4.116)$$

which is the same range-Doppler coupling relationship obtained previously.

Stretch processing and especially Eq. (4.110) will be revisited and extended in Chap. 8, where the technique is central to the polar format algorithm for spotlight synthetic aperture radar imaging. Additional details of stretch processing are given in Keel and Baden (2012).

## 4.7 Range Sidelobe Control for FM Waveforms

It was seen in the previous section that the output of the LFM matched filter exhibits sidelobes in range (equivalently, delay). These are a consequence of the approximately rectangular LFM matched filter output spectrum, which produces a sinc-like range response. The first range sidelobe is approximately 13 dB below the output peak for moderate-to-high BT products, and about -15 dB for small BT products. Sidelobes this large are unacceptable in many systems that will encounter multiple targets in range due to *target masking*. This phenomenon is shown in Fig. 4.33a, where the smaller target is barely visible above the sidelobes of the stronger target despite being separated by approximately sixteen times the Rayleigh resolution. The smaller target could not be reliably detected in this scenario. If the sidelobes could be reduced, this masking effect could be greatly reduced as shown in part b of the figure.

For a simple pulse, the matched filter output is a triangle function, which exhibits no sidelobes. Thus, sidelobe reduction is not an issue for that waveform and it will not be further discussed. For the LFM pulse, there are two basic approaches to delay sidelobe reduction: shaping the receiver frequency response, and shaping the waveform spectrum.

### 4.7.1 Matched Filter Frequency Response Shaping

Recall from *finite impulse response* (FIR) digital filter design that to reduce sidelobes of the frequency response of a digital filter, a window function is applied in the time domain to the impulse response. The goal here is to reduce sidelobes in range, corresponding to the time domain, so the analogous approach is to window the receiver frequency response in the frequency domain.

The matched filter frequency response is  $H(F) = X^*(F)$ , and at least for larger BT products is approximately rectangular. A modified frequency response  $H'(F)$  can be obtained by multiplying  $H(F)$  by a window function  $w(F)$ <sup>6</sup>

$$H'(F) = w(F)H(F) = w(F)X^*(F) \quad (4.117)$$

Figure 4.34a shows a Hamming window function overlaid on the matched filter frequency response for an LFM waveform with  $\beta\tau = 100$ .  $H'(F)$  is the product of these two functions. The resulting impulse response  $h'(t)$  is shown in Fig. 4.34b. The response of both the matched filter and the filter of Fig. 4.34b to the unwindowed LFM echo are overlaid in Fig. 4.35. The LFM waveform used had  $\beta\tau = 100$  and the window cutoff was placed at  $\pm\beta/2$  Hz. The peak sidelobe

<sup>6</sup>The lower case  $w$  is used for the frequency-domain window function  $w(F)$  to emphasize that the multiplying function is the window function itself (e.g., a Hamming window) rather than its Fourier transform.

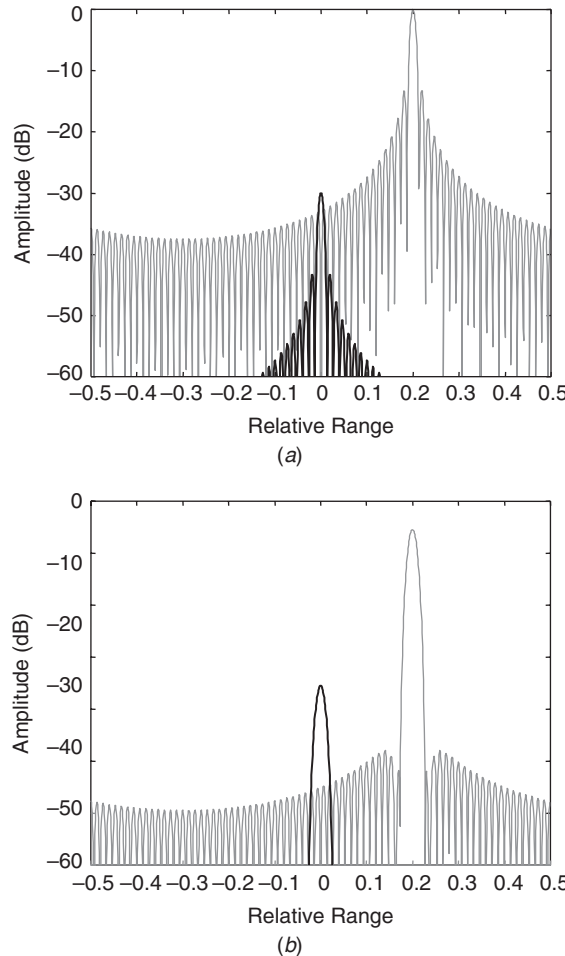


**FIGURE 4.33** Effect of windowing on target masking: (a) no windowing, (b) Hamming window applied.

has dropped 23.7 dB, from 13.5 dB below the mainlobe peak in the unwindowed case to 37.2 dB below the mainlobe peak for the windowed case. This comes at a cost of the mainlobe peak gain dropping 5.35 dB and the Rayleigh time (range) resolution increasing by 93 percent.

Since the matched frequency response does not have a perfectly sharp cutoff frequency, there is some uncertainty as to where in frequency to place the window cutoff. In the example, the support of the window equals the instantaneous frequency cutoff, which is 0.36 cycles per sample on the normalized frequency scale for this particular sampled LFM waveform. However, this choice cuts off some of the waveform energy in the sidelobes, increasing the mismatched filtering losses. A case could be made for a narrower support so that the window is applied only over the relatively flat portion of the spectrum. This would provide range sidelobes more closely matching those expected for the chosen window but would reduce the effective bandwidth, further degrading the range resolution. A case could also be made for increasing the support to maximize the output energy, but this choice might increase the range sidelobes by “wasting” some of the window shape on the skirts of the LFM spectrum.

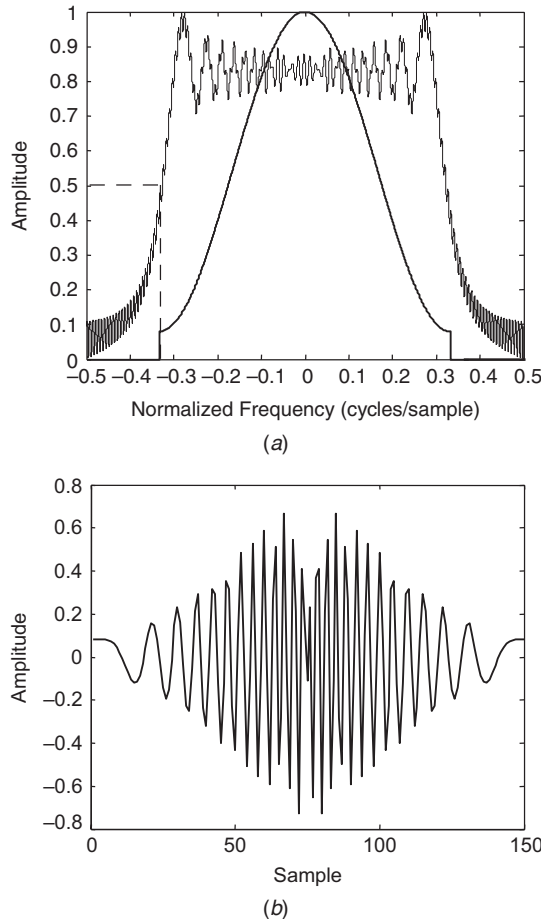


**FIGURE 4.34** Hamming weighting of the LFM receiver frequency response: (a) Hamming window overlaid on matched filter frequency response, (b) resulting filter impulse response  $h'(t)$ .

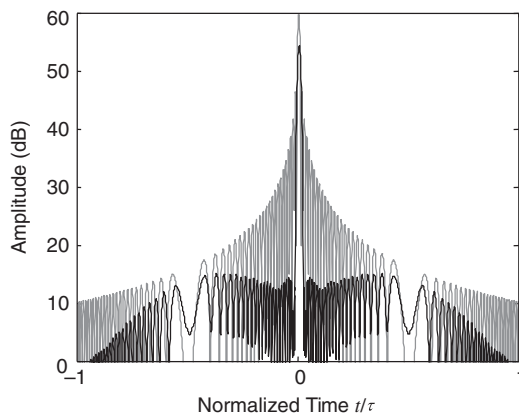


**FIGURE 4.35** Comparison of the receiver filter output with (black curve) and without (gray curve) frequency-domain Hamming weighting of the matched filter. See text for details.

Since  $H'(F) \neq X^*(F)$ , the modified receiver is not matched to the transmitted LFM pulse and therefore the output peak and SNR will be reduced from their maximum values. This effect was evident in Fig. 4.33b, where the peak of the dominant target response is several dB lower than the unwindowed case in part *a* of the figure. The losses in output peak amplitude and SNR can be estimated from the window function  $w(F)$ . In practice, a discrete window  $w[k]$  will be applied to a discrete-frequency version of  $H(F)$ ,  $H[k]$ . The loss in the peak signal output from the matched filter, called the *loss in processing gain* (LPG), is

$$LPG = \frac{K^2}{\left| \sum_{k=0}^{K-1} w[k] \right|^2} \quad (4.118)$$

where  $K$  is the window length. The loss in SNR at the matched filter output is called the *processing loss* (PL) and is

$$PL = \frac{K \sum_{k=0}^{K-1} |w[k]|^2}{\left| \sum_{k=0}^{K-1} w[k] \right|^2} \quad (4.119)$$

With these definitions *LPG* and *PL* are both greater than one so that the losses in decibels are positive numbers. For a relatively long Hamming window, the LPG is approximately 5.4 dB while the PL is approximately 1.4 dB. Both are weak functions of  $K$  and are slightly larger for small  $K$ . These formulas are approximate when applied to windowing of the LFM spectrum due to the finite-width transition of the LFM spectrum and the designer's discretion in choosing the cutoff of the window in frequency. In the example above, the LPG is 5.35 dB. Derivation of these formulas is deferred to Chap. 5, where they will arise again in the context of Doppler processing and where the results will be exact.

#### 4.7.2 Matched Filter Impulse Response Shaping

The impulse response of the filter just obtained and illustrated in Fig. 4.34b suggests that similar results could have been obtained by windowing the LFM waveform in the time domain. Consider again the signal in Eq. (4.89) having an arbitrary amplitude function  $A(t)$  and a quadratic phase function. The PSP approximation to its spectrum was given in Eq. (4.93). The magnitude of the spectrum is proportional to the *time-domain* amplitude:

$$|X(\Omega)| \propto \left| A\left(\frac{\Omega}{2\alpha}\right) \right| \quad (4.120)$$

If  $A(t)$  has finite support on  $-\tau/2 \leq t \leq \tau/2$ , it follows that  $X(\Omega)$  will have finite support on  $-\beta/2 \leq F \leq \beta/2$  and in that interval  $|X(\Omega)|$  has the same shape as the window magnitude  $|A(t)|$ . Thus, a Hamming-shaped (for example) spectrum can be obtained by applying a Hamming window to the impulse response  $h(t)$  instead of the frequency response  $H(F)$ . Note that this result is specific to the use of a linear FM waveform.

The output of the resulting filter is overlaid on the matched filter response in Fig. 4.36. It has the same general character as the frequency-domain weighting result but with some differences in details of the sidelobe structure. The peak is reduced from 60 to 54.64 dB with weighting, a nearly identical LPG of 5.36 dB. The peak sidelobe of the weighted response is 40.7 dB below the corresponding mainlobe peak, 3.5 dB better than the frequency-domain case. The Rayleigh width has increased 97 versus 93 percent in the frequency domain weighted case. This is consistent with the better sidelobe performance of the time-domain case. Additional detail on frequency- and time-domain weighting of LFM waveforms is available in Richards (2006).

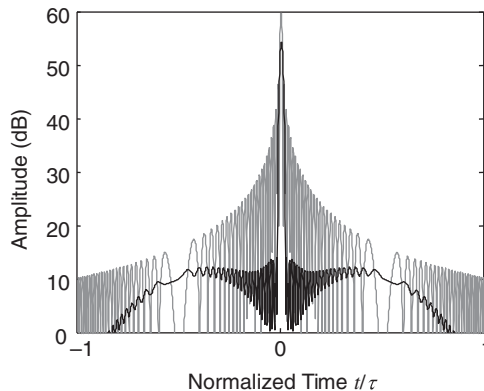


**FIGURE 4.36** Comparison of the receiver filter output with (black curve) and without (gray curve) time-domain Hamming weighting of the matched filter. See text for details.

### 4.7.3 Waveform Spectrum Shaping

The principal limitation of the receiver weighting approach to range sidelobe control is that the resulting filter is not matched to the transmitted waveform, resulting in an SNR loss. An alternative approach is to design a modified pulse compression waveform whose matched filter output inherently has lower sidelobes than the standard LFM. The waveform should be designed to have a spectrum shaped like that of a window function with the desired sidelobe behavior. Such a waveform would combine the maximized SNR of a truly matched filter with low sidelobes. There are two common ways to shape the spectrum. Both start with the idea that the LFM spectrum's relatively square shape is the result of a linear sweep rate combined with a constant pulse amplitude, resulting in a fairly uniform distribution of the signal energy across the spectral bandwidth. The spectral energy could be reduced at the edges, giving a "window-shaped" spectrum, by reducing the signal amplitude at the pulse edges while maintaining a constant sweep rate, by using a faster sweep rate at the edges with a constant pulse amplitude so as to spend less time in each spectral interval near the band edges, or both. The technique using variable sweep rates is referred to as *nonlinear FM* (NLFM).

The amplitude modulation technique implies operating the power amplifier at less than full power over the pulse length. This requires more complicated transmitter control but, more importantly, results in a pulse with less than the maximum possible energy for the given pulse length. This technique is not discussed further in this book; see Levanon and Mozeson (2004) for more information.

Two methods that have been proposed for NLFM waveform design are the principle of stationary phase method and empirical techniques. The PSP technique is used to design a temporal phase function from a prototype spectral amplitude function; the instantaneous frequency function is then obtained from the temporal phase. Examples of using this technique for deriving NLFM waveforms from common window functions such as Hamming or Taylor functions are given in Keel and Baden (2012).

One empirically developed design gives the instantaneous frequency function as (Price, 1979)

$$F_i(t) = \frac{t}{\tau} \left( \beta_L + \beta_C \frac{1}{\sqrt{1 - 4t^2/\tau^2}} \right), \quad |t| \leq \frac{\tau}{2} \quad (4.121)$$

The term  $\beta_L t / \tau$  represents a linear FM component, while the term involving  $\beta_C$  is designed to achieve a result that approximates a Chebyshev-shaped (constant sidelobe level) spectrum. Since  $F_i(t) = (1/2\pi)(d\theta(t)/dt)$ , integrating and scaling this instantaneous frequency function gives the required phase modulation

$$\theta(t) = \frac{\pi\beta_L}{\tau} t^2 - \frac{\pi\beta_C\tau}{2} \sqrt{1 - 4t^2/\tau^2}, \quad |t| \leq \frac{\tau}{2} \quad (4.122)$$

Figure 4.37 illustrates the behavior of the resulting nonlinear FM waveform for the case where  $\beta_L\tau = 50$  and  $\beta_C\tau = 20$ . The waveform is sampled at 10 times the bandwidth of the linear term,  $T_s = 1/10\beta_L$ . The instantaneous frequency (part *a* of the figure) is nearly linear in the center of the pulse but sweeps much more rapidly near the pulse edges. This reduces the spectral density at the pulse edge, resulting in the spectrum shown in part *c*, which has a window-like tapered shape instead of the usual nearly square LFM spectrum. The resulting matched filter output, shown in part *d*, has most of its sidelobes between -48 and -51 dB with the first sidelobe at -29 dB. In contrast, Fig. 4.38 illustrates the spectrum of the same waveform with  $\beta_C$  set to zero. This results in a linear FM waveform with the usual nearly square spectrum. These two figures are on the same normalized frequency scale. Comparing the spectra of these two waveforms illustrates how the nonlinear term has spread and tapered the LFM spectrum to lower the matched filter sidelobes. The LFM matched filter output has a peak sidelobe of -13.5 dB, decaying approximately as  $1/F$  at higher frequencies. The Rayleigh resolution in time of the NLFM waveform is approximately  $0.8/\beta_L$ , less than the  $1/\beta_L$  value observed for the LFM case but greater than  $1/(\beta_L + \beta_C)$ .

An example of a hybrid technique that combines a similar frequency modulation function with amplitude tapering of the matched filter impulse response is described in De Witte and Griffiths (2004). It is claimed there that the far sidelobes are controlled primarily by the maximum instantaneous frequency, while the near-in sidelobes are controlled by the amplitude weighting.

In addition to the more difficult phase control required, the major drawback of nonlinear FM pulses is their Doppler intolerance. Figure 4.39 shows the matched filter output for the waveform of Fig. 4.37 when a Doppler mismatch of  $7/\tau$  Hz is present. While the general sidelobe level remains largely unchanged, the mainlobe is seriously degraded, exhibiting both range-Doppler coupling (a shift of the peak) and severe spreading and ambiguity caused by very high near-in sidelobes. The major advantage of NLFM over linear FM with receiver weighting is that the receiver filter for the NLFM waveform is a matched filter so that lower sidelobes are achieved with no reduction of the matched filter output peak.

## 4.8 The Stepped Frequency Waveform

The LFM waveform increases resolution well beyond that of a simple pulse by sweeping the instantaneous frequency over the desired range  $\beta$  within the pulse. This technique is very effective and very common but does have drawbacks in some systems, particularly those using very large bandwidths on the order of hundreds of megahertz or more. First, the transmitter hardware must be capable of generating the LFM sweep. Second, all of the analog components must be able to support an instantaneous bandwidth of  $\beta$  Hz without introducing distortion. Even if stretch processing is used, the same is true of the receiver components up to and including the dechirp mixer and reference oscillator.

A second issue arises in systems using phase-steered array antennas. Recall from Chap. 1 that the antenna pattern of a phase-steered array antenna is determined primarily by the array factor

$$E(\theta) = E_0 \sum_{n=0}^{N-1} a_n e^{j(2\pi/\lambda)nd \sin \theta} \quad (4.123)$$

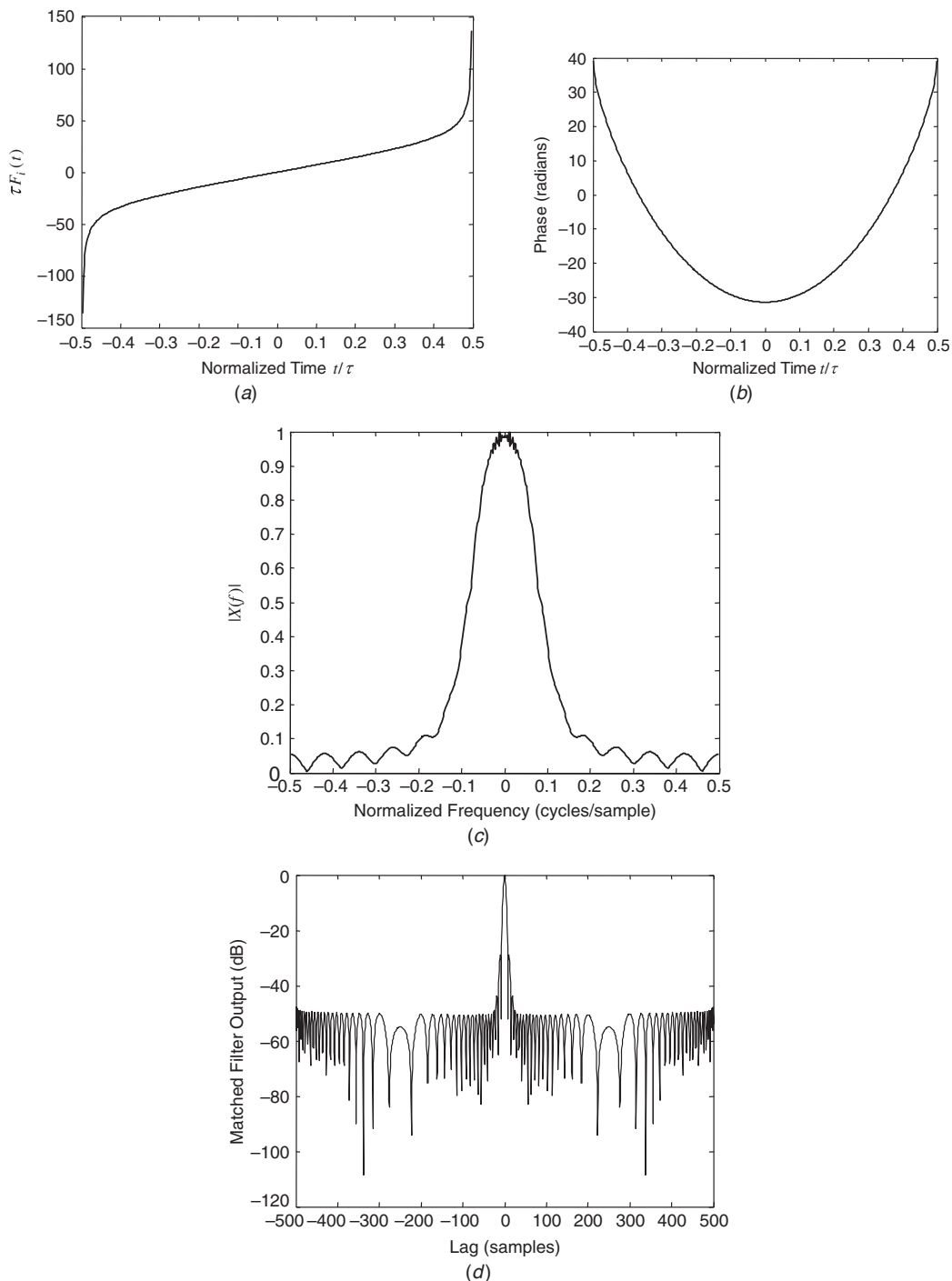


**FIGURE 4.37** Nonlinear FM waveform: (a) normalized instantaneous frequency  $\tau F_i(t)$ , (b) resulting phase modulation function, (c) magnitude of Fourier spectrum, (d) magnitude of matched filter output.

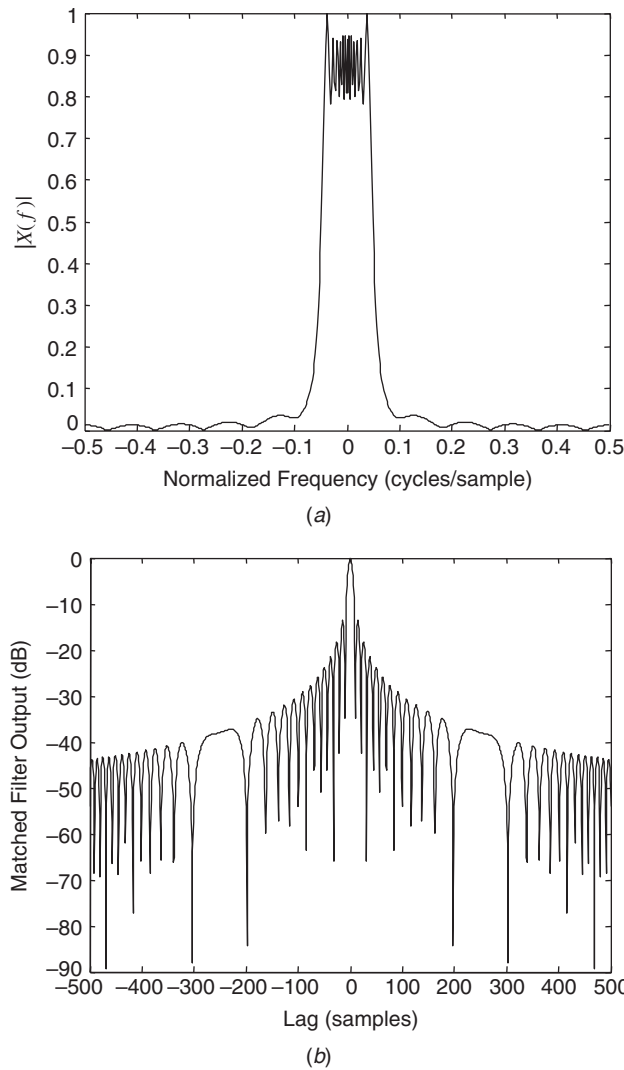


**FIGURE 4.38** FM waveform having same linear component as that of Fig. 4.33, but no nonlinear component: (a) magnitude of Fourier spectrum, (b) magnitude of matched filter output.

where  $d$  is the element spacing and the  $\{a_n\}$  are the complex weights on each subarray output. The antenna is steered to a particular look direction  $\theta_0$  by setting the steering weights  $a_n$  according to<sup>7</sup>

$$a_n = |a_n| e^{-j(2\pi/\lambda)nd \sin \theta_0} \quad (4.124)$$

<sup>7</sup>Array antennas can also be steered using time delay units at each element or a combination of phase steering within a subarray and time delay steering across subarrays. Pure time-delay-steered arrays do not suffer antenna steering errors due to wideband waveforms.

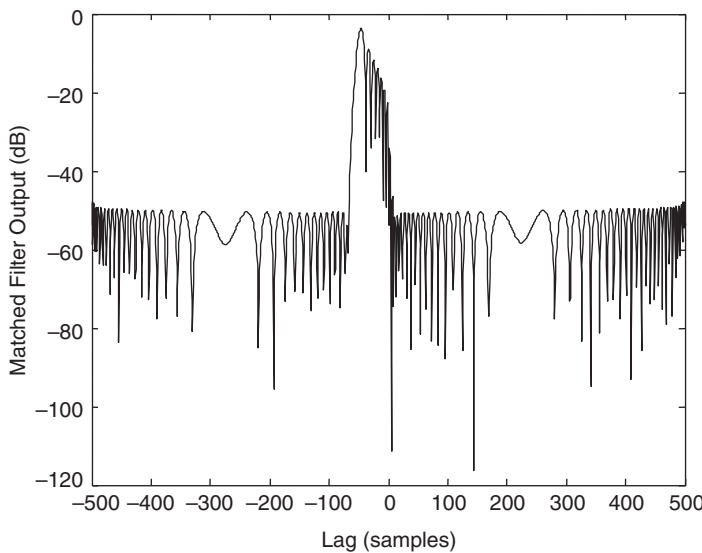


**FIGURE 4.39** Output of NLFM matched filter when  $F_D = 7/\tau$  Hz.

The magnitudes of the weights are chosen to provide the desired sidelobe level.  $E(\theta)$  will exhibit a peak at  $\theta = \theta_0$ ; for example, if  $|a_n| \equiv 1$ ,  $E(\theta)$  will be an sinc function with its peak at  $\theta_0$ . Note that the phases of the required weights  $\{a_n\}$  are a function of the wavelength  $\lambda$ . If an LFM pulse is transmitted, the effective wavelength changes during the pulse sweep. If the system is wideband, this wavelength change will be significant and the value of  $\theta$  at which  $E(\theta)$  peaks will change as well. That is, the antenna look direction will actually change during the LFM sweep (see Prob. 18). This undesired frequency steering effect is an additional source of SNR loss.

Stepped frequency waveforms are an alternative technique for obtaining a large bandwidth and thus fine range resolution without requiring intrapulse frequency modulation. A stepped frequency waveform is a pulse burst waveform. Each pulse in the burst is a simple, constant-frequency pulse; however, the RF is changed from one pulse to the next. The most common stepped frequency waveform employs a linear frequency stepping pattern, where the RF of each pulse is increased by  $\Delta F$  Hz from the preceding pulse. Factoring out the starting RF gives the following baseband waveform

$$x(t) = \sum_{m=0}^{M-1} x_p(t - mT) e^{j2\pi m \Delta F(t - mT)} \quad (4.125)$$

Figure 4.40 illustrates the linearly stepped frequency waveform.

Because only simple pulses are used for each constituent pulse, the instantaneous bandwidth capability of the transmitter and receiver need be only on the order of  $1/\tau$  Hz.

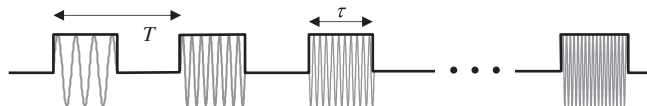


**FIGURE 4.40** Linearly frequency-stepped waveform.

The total bandwidth of the waveform as a whole is  $M \cdot \Delta F$ . When used with a phase-steered array antenna, the time between pulses can be used to reset the phase shifters to update the  $\{a_n\}$  sequence and maintain a nearly constant steering direction  $\theta_0$  as the effective wavelength changes from pulse to pulse. The major disadvantages of this waveform are that it requires a pulse-to-pulse tunable transmitter and receiver, and that  $M$  PRIs are required to collect data over the desired bandwidth instead of just one.

The pulse-by-pulse processing viewpoint applied to the constant-frequency pulse burst waveform can be applied again to analyze the matched filter response for the stepped frequency waveform. Suppose the radar is stationary, and a stationary target is located at a range corresponding to a delay  $t_l + \delta t$ , where  $\delta t$  represents an incremental delay relative to the nominal delay  $t_l$  corresponding to range bin  $l$ . Individual pulses are processed through the simple pulse matched filter as before, producing the output waveforms (assuming  $T_M = 0$ )

$$y_m(t) = s_p^* [t - (t_l + \delta t) - mT] e^{j2\pi m \Delta F [t - (t_l + \delta t) - mT]} \quad (4.126)$$

This output is then sampled at  $t = t_l + mT$  (that is,  $t_l$  seconds after the current pulse was transmitted), corresponding to range  $R_l = ct_l/2$ . The resulting sample becomes the  $l$ th coarse range bin sample for the current pulse

$$\begin{aligned} y[l, m] &= y_m(t_l - mT) \\ &= s_p^*(\delta t) e^{j2\pi m \Delta F \delta t} \end{aligned} \quad (4.127)$$

Equation (4.127) shows that the slow-time sequence at a fixed coarse range bin  $l$  when using a linearly stepped frequency waveform is a discrete time sinusoid. The frequency is proportional to the displacement of the scatterer from the nominal range bin location of  $R_l = ct_l/2$  meters. The amplitude of the sequence is weighted by the triangular simple pulse matched filter response evaluated at the incremental delay  $s_p(\delta t)$ .

Following the earlier discussion of pulse-by-pulse processing for the conventional pulse burst waveform, the slow-time matched filter impulse response for a target located at the nominal delay  $t_l + \delta t$  is  $h[m] = \exp(-j2\pi m \Delta F \delta t)$ . Thus, the matched filter impulse response is different for every value of  $\delta t$ . Consider a DTFT of the slow-time data

$$\begin{aligned} Y[l, \omega] &= \sum_{m=0}^{M-1} y[l, m] e^{-j\omega m} = \sum_{m=0}^{M-1} s_p^*(\delta t) e^{j2\pi m \Delta F \delta t} e^{-j\omega m} \\ &= s_p^*(\delta t) \sum_{m=0}^{M-1} e^{-j(\omega - 2\pi \Delta F \delta t)m} \end{aligned} \quad (4.128)$$

The summation will yield an sinc function having its peak at  $\omega = 2\pi \Delta F \delta t$ . Thus, the peak of the DTFT of the slow-time data in a fixed range bin with a linearly stepped frequency waveform provides a measure of the delay of the scatterer relative to the nominal delay  $t_l$ . Specifically, if the peak of the DTFT is at  $\omega = \omega_p$ , the scatterer is at an incremental delay

$$\delta t = \frac{\omega_p}{2\pi \Delta F} = \frac{f_p}{\Delta F} \text{ seconds} \quad (4.129)$$

Note also that the DTFT evaluated at  $\omega_p$  is the matched filter for the slow-time sequence, so that the data samples are integrated in phase

$$\begin{aligned} Y[l, \omega_p] &= \sum_{m=0}^{M-1} s_p^*(\delta t) e^{j2\pi m \Delta F \delta t} e^{-j\omega_p m} \\ &= s_p^*(\delta t) \sum_{m=0}^{M-1} (1) = M s_p^*(\delta t) \end{aligned} \quad (4.130)$$

The factor of  $M$  is the coherent integration gain from using  $M$  pulses. If  $\delta t = 0$ , meaning the matched filter output was sampled at its peak,  $Y[l, \omega_p] = ME_p = E$ , the total waveform energy. If  $\delta t \neq 0$  the ambiguity function of the individual pulses reduces the amplitude of the slow-time samples by  $|s_p(\delta t)|$ . This represents a straddle loss.

It follows that applying a  $K$ -point DFT to the slow-time sequence implements  $K$  filters, each matched to a different incremental delay  $\delta t$ . Thus, the DFT of the slow-time data within a single range bin for a stepped frequency waveform is a map of echo amplitude versus incremental range within that coarse range bin.

The DTFT of an  $M$ -point sinusoid has a Rayleigh frequency resolution of  $\Delta f = 1/M$  cycles per sample. Using the scaling between  $f$  and  $t$  from Eq. (4.129), the corresponding time resolution is  $\Delta t = 1/M \cdot \Delta F$  seconds; the range resolution is therefore

$$\Delta R = \frac{c}{2M \cdot \Delta F} = \frac{c}{2\beta} \text{ meters} \quad (4.131)$$

where  $\beta$  is the total stepped bandwidth  $M \cdot \Delta F$ . Thus, the linearly stepped frequency waveform achieves the same range resolution as a single pulse of bandwidth  $\beta$ . If a  $K$ -point DFT is used to process the slow-time data the DFT output will provide range measurements at intervals of

$$\delta R = \frac{c}{2K \cdot \Delta F} = \frac{M}{K} \Delta R \quad (4.132)$$

Since  $K \geq M$  normally, the DFT output provides echo amplitude samples at intervals equal to or less than the range resolution. This fine-resolution reflectivity map is often called a *high resolution range profile*<sup>8</sup> or just a *range profile*.

The total bandwidth  $\beta$  of the stepped frequency waveform is determined by the desired range resolution. It can be realized by various combinations of the number of frequency steps  $M$  and the step size  $\Delta F$ . To determine how to choose these parameters, note that the DTFT of the slow-time data is periodic in  $\omega$  with period  $2\pi$  radians per sample. Because the DTFT peak is at  $\omega_p = 2\pi\Delta F\delta t$ , the range profile is periodic in  $\delta t$  with period  $1/\Delta F$ . This periodicity establishes the required coarse range bin spacing. Specifically, avoiding range ambiguities in the range profile requires  $c/2\Delta F > L_t$ , where  $L_t$  is the maximum target length of interest. Once  $\Delta F$  is chosen,  $M$  is selected to span the bandwidth required to provide the desired fine range resolution. The DFT range profile then effectively breaks each relatively large coarse range bin ( $c/2\Delta F$  meters) into  $M$  fine-resolution range bins ( $c/2\beta$  meters) sampled at  $K$  points within the coarse range bin. If  $K = M$  the range sample spacing equals the range resolution. If  $K > M$  the range profile is oversampled compared to the resolution by the factor  $K/M$ . The pulse length  $\tau$  is chosen to balance straddle losses and range ambiguities. Recall that the single-pulse matched filter output  $s_p(t)$  is  $2\tau$  seconds long. Choosing  $\tau < 1/2\Delta F$  means that  $s_p(t)$  will be no more than  $1/\Delta F$  seconds long so that a scatterer will only influence measurements in one coarse range bin, avoiding range ambiguities. On the other hand, the shorter  $\tau$  is made, the greater the potential straddle loss for targets located between coarse range samples. A detailed consideration of these tradeoffs is in Keel and Baden (2012).

Details of the Doppler response and ambiguity function of the linearly stepped frequency waveform are available in Levanon and Mozeson (2004). A small central portion of the ambiguity function is shown in Fig. 4.41 for the case  $M = 8$  pulses, PRI  $T = 10\tau$ , and a frequency step size of  $\Delta F = 0.8/\tau$ . The resulting bandwidth is  $\beta = M \cdot \Delta F = 6.4/\tau$  Hz. The AF displays both the skewed response typical of a linear FM modulation, and the range and

<sup>8</sup>While “fine” is preferred in this text to “high” to describe small values of resolution, the term “high range resolution profile” is well-established in the literature.

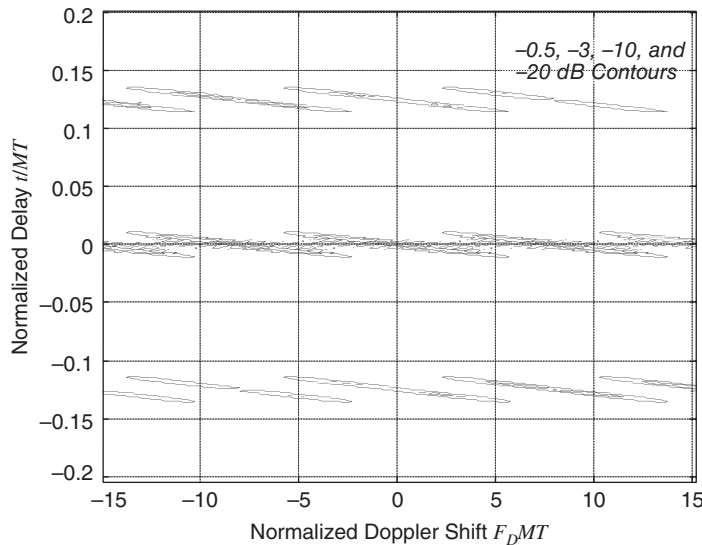


**FIGURE 4.41** Contour plot of the central portion of the ambiguity function of a pulse burst waveform.  $M = 8$ ,  $T = 10\tau$ , and  $\Delta F = 0.8/\tau$ .

Doppler ambiguities typical of pulse burst waveforms. Ambiguities in delay (range) are evident at intervals of  $T$  seconds, corresponding to  $1/8 = 0.125$  on the normalized scale of the figure. The first zero in Doppler of the main ridge occurs at  $1/MT$  Hz, corresponding to 1 on the normalized Doppler scale.

Figure 4.42a further magnifies the delay coordinate of this AF. The delay coordinate now covers the interval  $\pm \tau = \pm 0.0125$  ( $\pm 1/80$ ) on this normalized scale. The zero-delay and zero-Doppler axes are highlighted by the heavier gray lines. The expected Rayleigh resolution in delay is  $1/\Delta F = \tau/6.4$ , which becomes 0.002 on this scale. The dotted heavy gray line marks the  $+0.002$  delay coordinate. It can be seen that this intersects the first null on the zero-Doppler axis of the AF, confirming that the intended resolution is achieved.

Choosing  $\Delta F > 1/\tau$  allows generation of a wide total bandwidth with fewer pulses and therefore a shorter data collection time, but the resulting undersampling creates aliasing that appears as extra range ambiguities (also called grating lobes). Figure 4.42b shows a similar view of another case with  $\Delta F \cdot \tau = 2.5$  but the other parameters unchanged. The bandwidth is now  $20/\tau$  Hz so the resolution in delay is correspondingly finer. However, there are now five peaks along the zero-Doppler axis, representing five range ambiguities, within  $\pm 1$  pulse length.

## 4.9 The Stepped Chirp Waveform

The stepped chirp waveform is a stepped frequency waveform that substitutes an LFM constituent pulse for the constant-frequency pulse used above. It can achieve very wideband operation without resorting to stretch processing, thereby avoiding the restriction of short range windows. In addition, it avoids the array frequency steering effects mentioned previously so long as the individual pulse bandwidth is not too large.

The stepped chirp waveform can allow a large frequency step  $\Delta F > 1/\tau$  without suffering the aliasing seen in the conventional stepped frequency waveform. Careful design is needed to relate the LFM pulse bandwidth and length to the RF step size in order to achieve

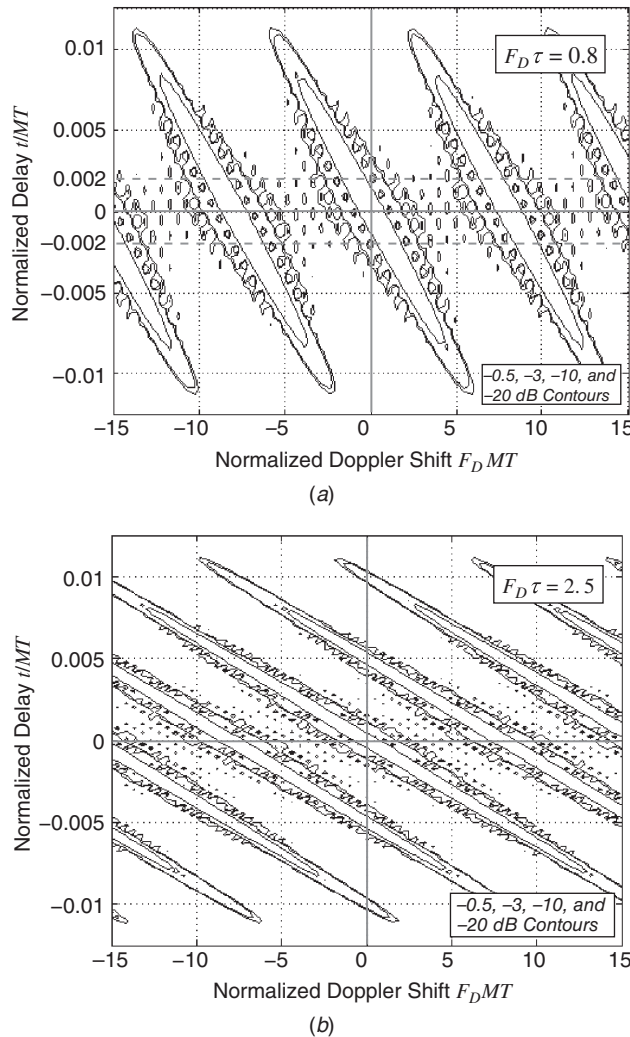


**FIGURE 4.42** Contour plot of the central portion of the ambiguity function of a pulse burst waveform:  $M = 8$ ,  $T = 10\tau$ , (a)  $\Delta F = 0.8/\tau$  (same waveform as Fig. 4.41), (b)  $\Delta F = 2.5/\tau$ .

effective suppression of the ambiguities. Details and sample parameter sets are given in Levanon and Mozeson (2004). Processing of the waveform requires individually demodulating and matched filtering each individual pulse, and then post-processing the ensemble to construct a new signal with the full bandwidth. This post-processing can be performed in either the time or frequency domain. Details are given in Keel and Baden (2012).

## 4.10 Phase-Modulated Pulse Compression Waveforms

The second major class of pulse compression waveforms is referred to as *phase coded* waveforms. A phase coded waveform has a constant RF but an absolute phase that is switched between one of two or more fixed values at regular intervals within the pulse length. Such a

pulse can be modeled as a collection of  $N$  contiguous subpulses  $x_n(t)$  of duration  $\tau_c$ , each with the same frequency but a (possibly) different phase

$$\begin{aligned} x(t) &= \sum_{n=0}^{N-1} x_n(t - n\tau_c) \\ x_n(t) &= \begin{cases} \exp(j\phi_n), & 0 \leq t \leq \tau_c \\ 0, & \text{elsewhere} \end{cases} \end{aligned} \quad (4.133)$$

The total pulse length is  $\tau = N\tau_c$ . Individual subpulses are often referred to as *chips*. Phase coded waveforms are divided into *biphase codes* and *polyphase codes*. A biphase code has only two possible choices for the phase state  $\phi_n$ , typically 0 and  $\pi$ ; a polyphase code has more than two phase states. There are several common subcategories of each. Figure 4.1c was an example of a biphase-coded waveform.

The matched filter output for a phase coded pulse is derived in detail in Levanon and Mozeson (2004); the result is now summarized. Denote the sequence of complex amplitudes of the individual pulse chips  $x_n(t)$  of Eq. (4.133) as  $\{A_n\} = \{\exp[j\phi_n]\}$ . Express the time variable  $t$  in terms of the chip duration  $\tau_c$  and an offset  $\eta$ , as  $t = k\tau_c + \eta$ ,  $0 \leq \eta < \tau_c$ . The matched filter output, which is just the autocorrelation of  $x(t)$ , is

$$y(t) = s_x(t) = y(k\tau_c + \eta) = \left(1 - \frac{\eta}{\tau_c}\right)s_A[k] + \frac{\eta}{\tau_c}s_A[k+1] \quad (4.134)$$

where  $s_A[k]$  is the discrete autocorrelation of the complex amplitude sequence  $\{A_n\}$ . Equation (4.134) shows that  $s_x(t)$  takes on the value  $s_A[k]$  at  $t = k\tau_c$ , and is linearly interpolated (in the complex plane) between adjacent samples. Thus, the matched filter output can be determined by computing the autocorrelation of the amplitude sequence and interpolating between those values. One consequence of this result and the fact that the  $\{A_n\}$  have unit magnitude is that the peak value of the autocorrelation will always be  $s_x(0) = N$ .

### 4.10.1 Biphase Codes

The most common biphase codes in radar are the *Barker codes*. Barker codes are a specific set of biphase sequences that have a maximum sidelobe magnitude of 1 at the matched filter output and therefore attain an  $N : 1$  ratio of the peak to the highest sidelobe. A low-frequency Barker coded waveform for  $N = 13$  is shown in Fig. 4.43. The phase switches are visible at  $t = 5\tau_c, 7\tau_c, 9\tau_c, 10\tau_c, 11\tau_c$ , and  $12\tau_c$ . Because there are only two phase states, the waveform is often represented by a diagram such as the one shown in Fig. 4.44, using either "+" and "-" symbols as shown, or +1 and -1 symbols. Note that biphase codes do not necessarily change phase state at every subpulse transition.

Recall that pulse compression waveforms have a bandwidth  $\beta \gg 1/\tau$ . Because phase coded waveforms are constant frequency, it may not be obvious that their spectrum is spread. However, the discontinuities caused by the phase transitions do spread the signal spectrum. As an example, Fig. 4.45 shows the effect of a single phase switch of  $180^\circ$  on the spectrum of a constant-frequency waveform. While the effect depends on the point in the pulse at which the switch occurs, clearly it significantly spreads the signal energy in frequency. Multiple phase transitions increase this effect: Fig. 4.46 compares the spectra of the 13-bit Barker coded waveform with that of a simple pulse of the same duration. The Rayleigh bandwidth of the Barker spectrum is  $\beta = 1/\tau_c$  Hz (about 13 times as wide as that of the simple pulse in this specific case). In addition, the

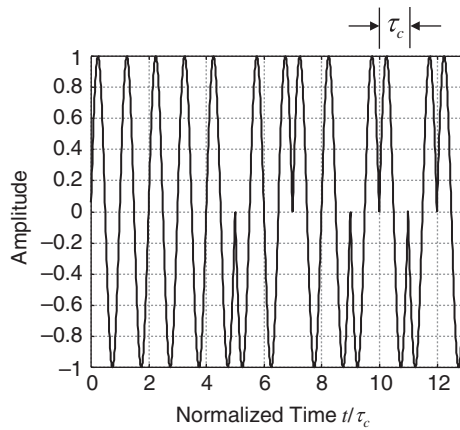


FIGURE 4.43 Barker coded waveform,  $N = 13$ .

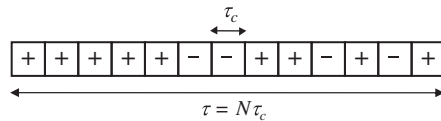


FIGURE 4.44 Binary sequence describing the Barker code of Fig. 4.43.

sidelobes of the Barker waveform spectrum decay much more slowly than those of the simple pulse.

Because of the increased bandwidth, the signal processing gain due to pulse compression with the Barker codes in particular, and phase codes in general, is the same factor  $G_{sp} = \beta\tau$  that applied for the LFM waveform. This is again because a simple pulse must be shorter than a phase-coded pulse by the factor  $\beta\tau$  to achieve the same Rayleigh resolution in time. Note that in the case of phase codes,  $\beta\tau$  can also be expressed as  $\tau/\tau_c$ .

One of the major disadvantages of Barker codes is that there are not very many of them. Barker codes have been found only for  $N$  up to 13. Sample Barker codes of all known lengths are listed in Table 4.1; more than one code exists for some lengths, while none exist for  $N = 6, 8 - 10$ , and 12. The table also lists the peak sidelobe level (PSL) relative to the mainlobe peak, which is simply  $20 \log_{10}(1/N)$ . Because of the modest lengths, low PSLs are not attainable.

As an example, consider the Barker code with  $N = 13$ . Representing the code sequence of Table 4.1 as the sequence  $\{A_n\} = \{1, 1, 1, 1, 1, -1, -1, 1, 1, -1, 1, -1, 1\}$  gives the autocorrelation sequence  $\{1, 0, 1, 0, 1, 0, 1, 0, 1, 0, 1, 0, 1, 0, 1, 0, 1, 0, 1, 0, 1, 0, 1, 0, 1, 0, 1, 0, 1, 0, 1, 0, 1\}$ . Figure 4.47 illustrates the resulting autocorrelation function obtained by interpolating between the discrete autocorrelation samples. In addition to a peak autocorrelation value of  $N$  and sidelobe peaks equal to 1, the discrete autocorrelation sequence sidelobes of a Barker code always follow an alternating pattern of zeros and ones. Consequently, the Rayleigh resolution is always  $\tau_c$  seconds in time or  $c\tau_c/2$  meters in range. Thus, the resolution is set by the chip length instead of the complete pulse length.

Barker codes have two major disadvantages. The first is that the lack of Barker codes longer than  $N = 13$  limits the degree of sidelobe suppression possible. The second is that they are very Doppler intolerant. A Doppler phase rotation of  $360^\circ$  across the full pulse is

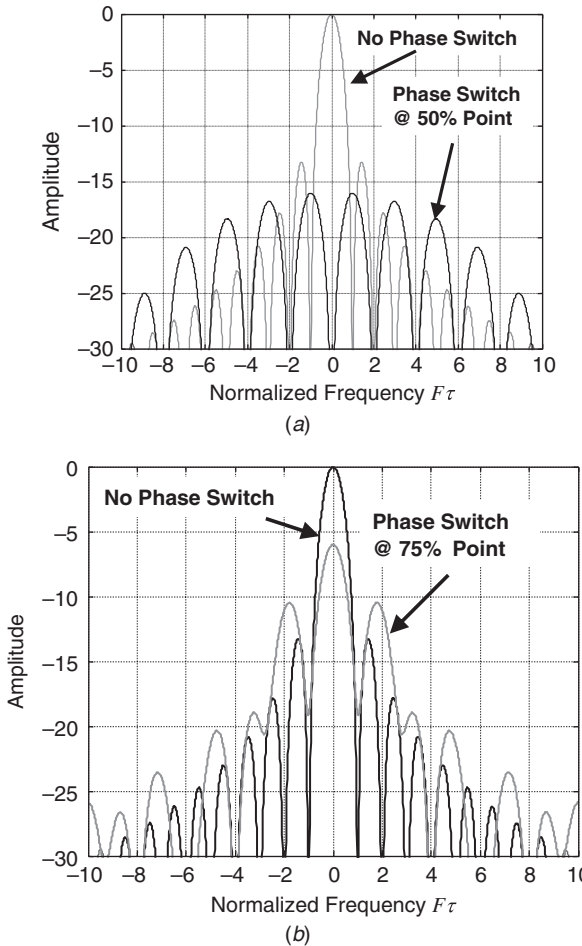


**FIGURE 4.45** Effect of a single  $180^\circ$  phase switch on the spectrum of a constant-frequency pulse: (a) phase switch occurs at  $t = \tau/2$ , (b) phase switch occurs at  $t = 3\tau/4$ .

more than sufficient to completely break up the structure of the matched filter output, as seen in the 13-bit Barker ambiguity function contour plot of Fig. 4.48. As a consequence, it is common to design Barker coded waveforms to limit the Doppler phase rotation to one-quarter cycle or less, which requires that the maximum expected Doppler shift and target velocity satisfy

$$F_{D_{\max}} \tau < \frac{1}{4} \Rightarrow v_{\max} < \frac{\lambda}{8\tau} \quad (4.135)$$

This constraint limits the Doppler mismatch loss to 1 dB or less.

The limited number and length of Barker codes has led to various techniques for constructing longer biphasic codes with good sidelobe properties. *Combined* or *nested* Barker codes form a longer code as the Kronecker product of two shorter Barker codes. If an  $N$ -bit Barker code sequence is denoted as  $B_N$ , an  $MN$ -bit code can be constructed as  $B_M \otimes B_N$ . The Kronecker product is simply the  $B_N$  code repeated  $M$  times, with each repetition multiplied

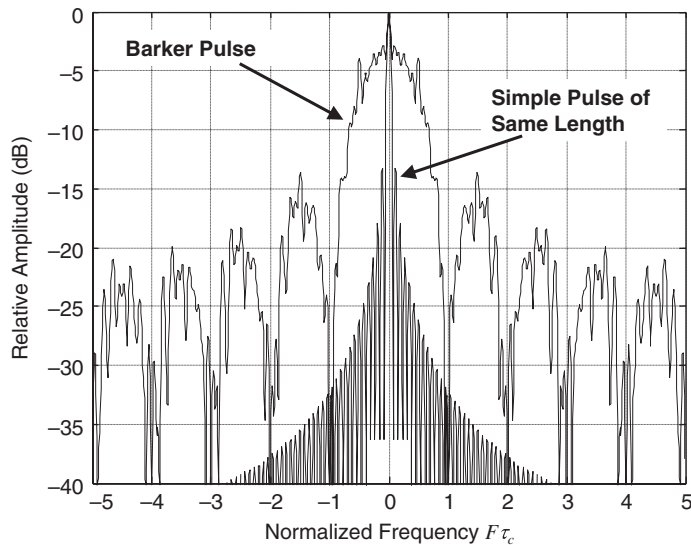


**FIGURE 4.46** Spectra of a 13-bit Barker coded pulse and a simple pulse of the same length.

by the corresponding element of the  $B_M$  code. For example, a 20-bit code can be constructed as the product  $B_4 \otimes B_5$

$$\begin{aligned}
 B_4 \otimes B_5 &= \{1, 1, 1, -1\} \otimes \{1, 1, 1, -1, 1\} \\
 &= (1)\{1, 1, 1, -1, 1\} + (1)\{1, 1, 1, -1, 1\} + (1)\{1, 1, 1, -1, 1\} + \dots \\
 &\quad \dots + (-1)\{1, 1, 1, -1, 1\} \\
 &= \{1, 1, 1, -1, 1, 1, 1, 1, -1, 1, 1, 1, 1, -1, 1, -1, -1, 1, -1\} \tag{4.136}
 \end{aligned}$$

<b>N</b>	<b>Code Sequence</b>		
	<b>+/-Format</b>	<b>Octal</b>	<b>PSL, dB</b>
2	+-	2	-6.0
2	++	3	-6.0
3	++-	6	-9.5
4	++-+	15	-12.0
4	+++-	16	-12.0
5	+++-+	35	-14.0
7	+++-+--	162	-16.9
11	+++-+-+-+--	3422	-20.8
13	+++-+-+-+--+-+	17465	-22.3

**TABLE 4.1** Barker Codes

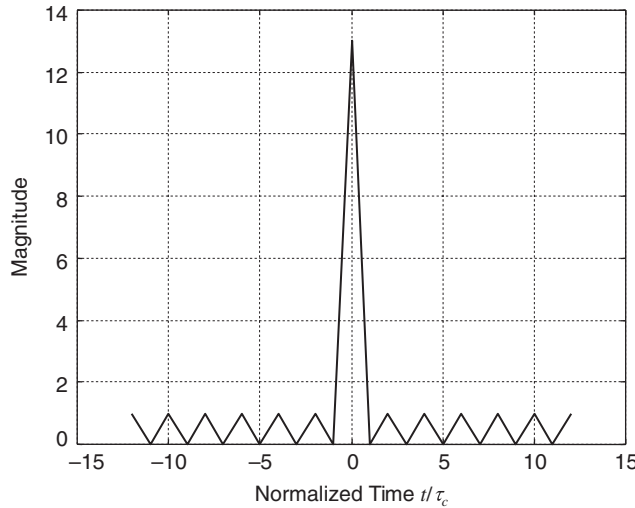


**FIGURE 4.47** Matched filter output for a 13-bit Barker code.

These codes have a peak sidelobe higher than 1. The autocorrelation of the code of Eq. (4.136) is shown in Fig. 4.49. Notice that the magnitude of the peak sidelobes is 5, so that the PSL compared to the autocorrelation peak is only 1/4 instead of the 1/20 that would be obtained if a 20-bit Barker code existed. A code that obtains a PSL = 2 for  $N = 20$  is discussed momentarily.

Another technique uses pseudorandom noise sequences to generate much longer biphase codes. Pseudorandom sequences have length  $N = 2^P - 1$  for some  $P$  and generally exhibit range sidelobes on the order of  $-10 \log_{10}(N)$ . For example, the matched filter output for a typical  $N = 1023$  ( $P = 10$ ) code, shown in Fig. 4.50, has peak sidelobes just above -30 dB.

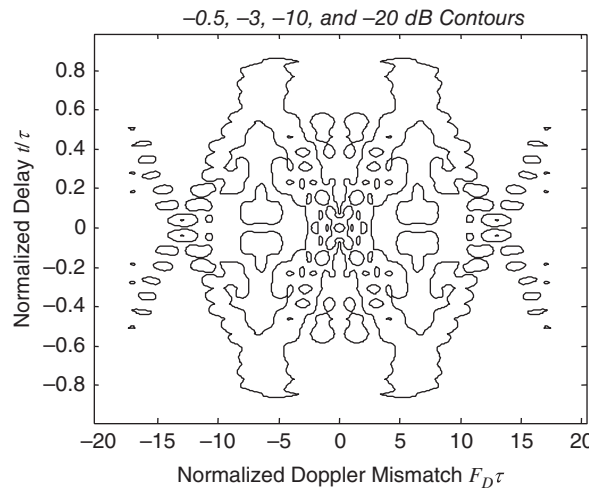


**FIGURE 4.48** Contour plot of ambiguity function of a 13-bit Barker code.

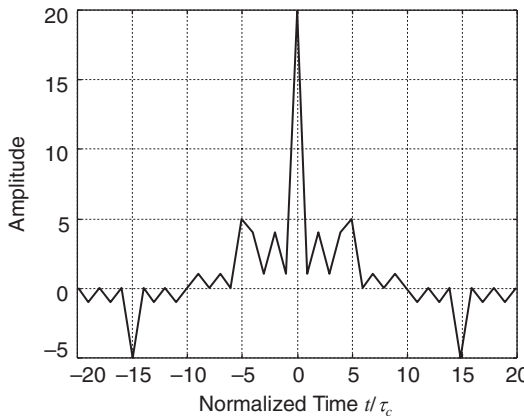


**FIGURE 4.49** Autocorrelation of combined  $B_4 \otimes B_5$  code.

While the Barker codes are the only biphase codes with a peak sidelobe value of 1 that are known to exist, one can seek longer codes with *minimum peak sidelobe* (MPS) levels for the length of interest. These *MPS codes* are found by exhaustive search techniques, taking advantage of certain properties of biphase code autocorrelations to prune the search somewhat. As an example, the MPS code for  $N = 20$  has a maximum sidelobe level of 2, giving a PSL ratio of 1/10 instead of the 1/4 obtained by the nested Barker code above. The state of the art is summarized and references given in Keel (2010). The peak sidelobe for MPS codes of lengths 2 through 5, 7, 11, and 13 (Barker codes) is 1; for  $N = 6, 8 - 10, 12, 14 - 21, 25$ , and 28 is 2; for  $N = 22 - 24, 26 - 27, 29 - 48$ , and 51 is 3; for  $N = 49 - 50$  and  $52 - 82$  is 4; and for  $N = 83 - 105$  is 5. The MPS has not been established at this writing for codes longer than 105. Table 4.2 lists one sample code for the longest code length in each of these sidelobe level regimes; additional sample codes for other lengths are available in the references. It is evident that the sidelobe level in dB improves only very slowly as the code length increases.

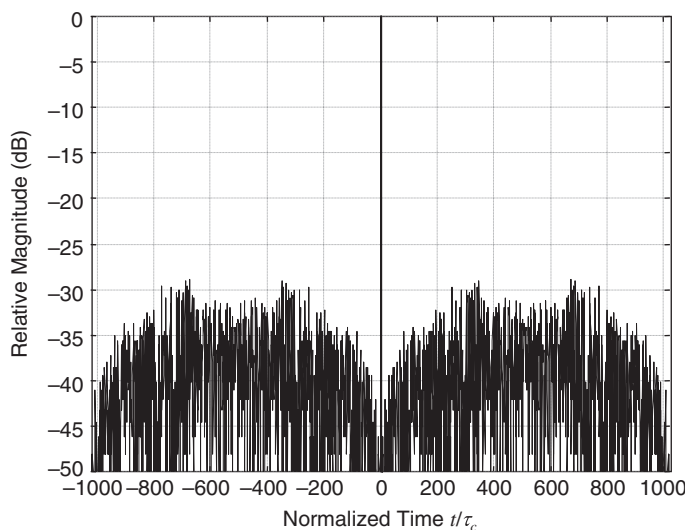


**FIGURE 4.50** Matched filter output for a 1023-bit pseudorandom biphase code.

Code Length $N$	Sample Code (Hexadecimal)	Peak Sidelobe Level (PSL)	PSL, dB
13 (Barker)	1F35	1	-22.3
28	8F1112D	2	-22.9
51	0E3F88C89524B	3	-24.6
82	3CB25D380CE3B7765695F	4	-26.2
105	1C6387FF5DA4FA325C895958DC5	5	-26.4

TABLE 4.2 Sample Minimum Peak Sidelobe Biphase Codes

#### 4.10.2 Polyphase Codes

Biphase codes, as noted previously, have poor Doppler tolerance. They also suffer from precompression bandlimiting effects. As is shown in Fig. 4.51, the spectrum of a typical biphase code not only exhibits the desired mainlobe spreading, but also a very slow falloff of the far sidelobes. This is a direct consequence of the sharp phase discontinuities. Practical receivers will have a noise-limiting bandpass filter that will bandlimit the biphase waveform spectrum, smoothing the phase transitions. This has the effect of mismatching the received waveform relative to the correlator, reducing the peak gain and widening the mainlobe.

*Polyphase codes* allow arbitrary values for the chip phases  $\phi_n$ . Compared to biphase codes, they can exhibit lower sidelobe levels and greater Doppler tolerance. A number of polyphase codes are in common use. These include “polyphase Barker codes,” the Frank codes, and the P1, P2, P3, P4, and P( $n, k$ ) codes. All of these except the polyphase Barker codes are related to LFM or NLFM waveforms. Numerous other polyphase codes have been proposed; many are described in Levanon and Mozeson (2004). The special case of quadriphase codes is described in Keel and Baden (2012).

*Frank codes* are codes whose length is a square,  $N = M^2$  for some  $M$ . The phase sequence for a Frank code is given by

$$\phi_n = \phi(Mp + q) = \frac{2\pi}{M} pq, \quad p = 0, 1, 2, \dots, M-1, \quad q = 0, 1, 2, \dots, M-1 \quad (4.137)$$

As an example, if  $M = 4$  so  $N = 16$ , the sequence of phases becomes

$$\phi_n = \left\{ \underbrace{0 \ 0 \ 0 \ 0}_{p=0} \underbrace{\frac{\pi}{2} \ \pi \ \frac{3\pi}{2}}_{p=1} \underbrace{0 \ \pi \ 0 \ \pi}_{p=2} \underbrace{0 \ \frac{3\pi}{2} \ \pi \ \frac{\pi}{2}}_{p=3} \right\} \quad (4.138)$$

Figure 4.51 shows the magnitude of the matched filter output for the case  $N = 16$ .<sup>9</sup> Note that while the mainlobe has a local minimum at  $t = \tau_c$ , it does not go to zero at that point as the Barker code autocorrelations do. The largest sidelobe in this example is  $\sqrt{2}$ , larger than the Barker codes. The sidelobe level is  $\sqrt{2}/16$  or -21.1 dB. Figure 4.52 shows the ambiguity function in contour plot form. The main ridge is skewed in the delay-Doppler plane, similar to the range-Doppler coupling of an LFM ambiguity function.

<sup>9</sup>This figure may appear to violate the earlier claim that the continuous autocorrelation function is a linear interpolation between the discrete autocorrelation values of the code sequence  $\exp(j\phi_n)$ . However, linear interpolation of the complex values does not result in linear interpolation of the magnitude; see Prob. 4.24.

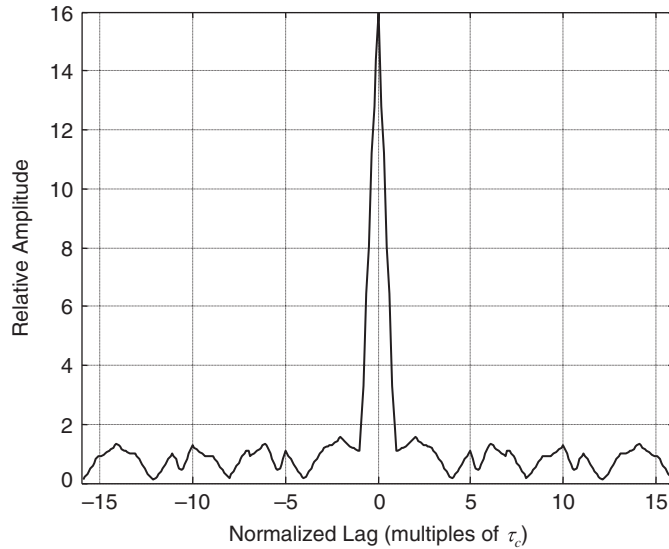


**FIGURE 4.51** Matched filter output for a 16-bit Frank code.

The *P3* and *P4* codes of length  $N$  are given, respectively, by

$$\text{P3: } \phi_n = \begin{cases} \frac{\pi}{N} n^2, & n = 0, 2, \dots, N-1 \quad (N \text{ odd}) \\ \frac{\pi}{N} n(n+1), & n = 0, 1, 2, \dots, N-1 \quad (N \text{ even}) \end{cases} \quad (4.139)$$

$$\text{P4: } \phi_n = \frac{\pi}{N} n^2 - \pi n, \quad n = 0, 1, 2, \dots, N-1$$

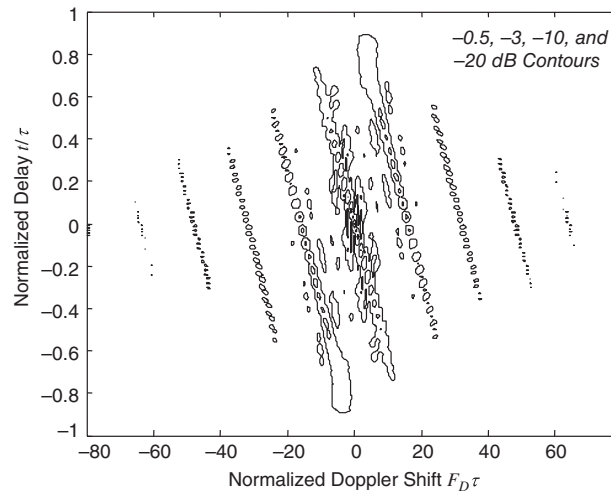


**FIGURE 4.52** Contour plot of 16-bit Frank code ambiguity function.

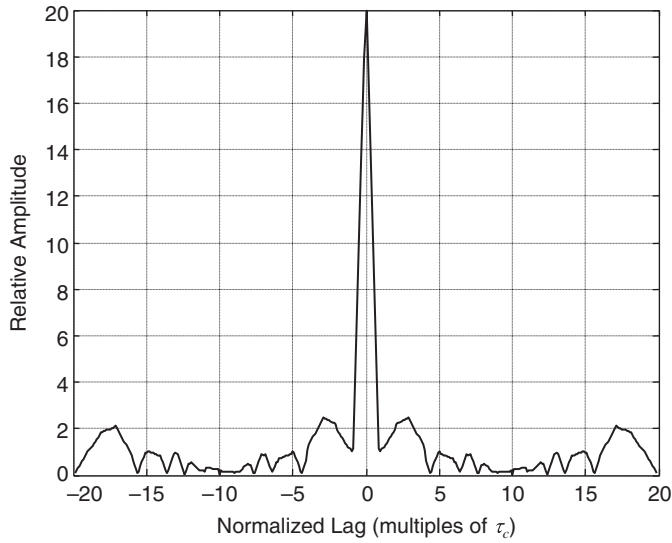


FIGURE 4.53 Matched filter output for a 20-bit P3 code.

Unlike the Frank code, these codes can be generated for any length  $N$ . Figure 4.53 shows the matched filter output for the  $N = 20$  P3 code, while Fig. 4.54 shows the corresponding ambiguity function. Again, range-Doppler coupling is evident.

The Frank, P3, and P4 codes all are based on quadratic phase progressions, as is evident from Eqs. (4.137) and (4.139), and are therefore related to LFM waveforms. Figure 4.55 shows the (unwrapped) phase progression of these three codes for the case  $N = 16$ . The P3 and P4 codes are truly quadratic, the difference being whether the minimum phase “slope” occurs

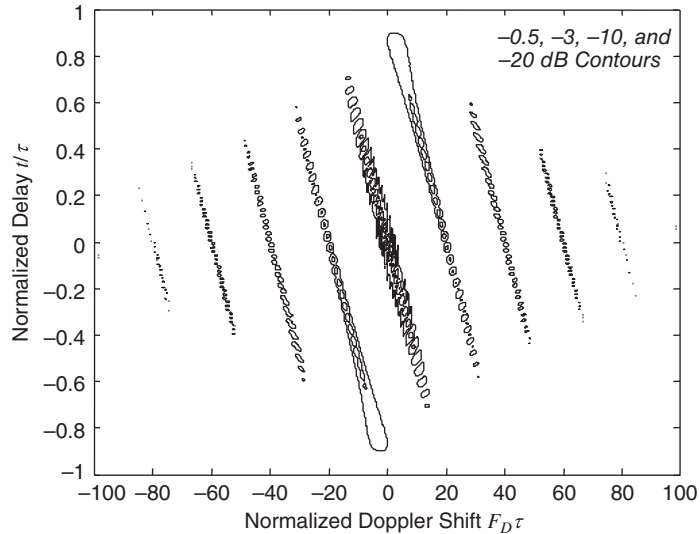


FIGURE 4.54 Contour plot of ambiguity function of 20-bit P3 code.

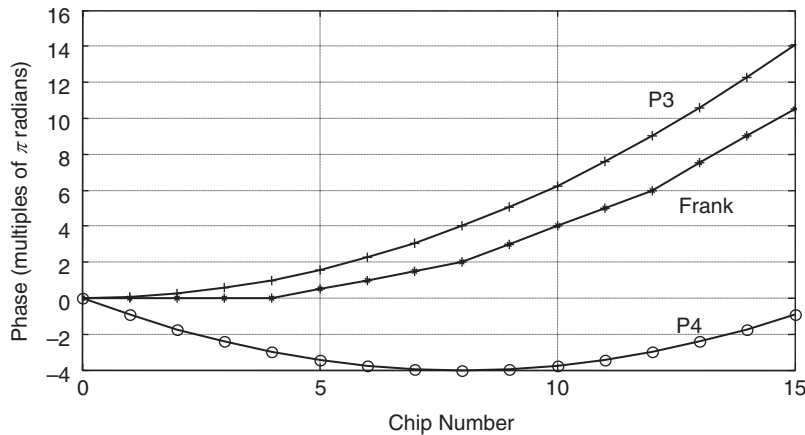


FIGURE 4.55 Unwrapped phase sequences of 16-bit Frank, P3, and P4 codes.

at the beginning (P3) or the middle (P4) of the waveform. The smallest phase increments, and thus the minimum discontinuities in the actual RF waveform, occur where the phase slope is least. The Frank code uses a piecewise linear approximation to a quadratic phase progression. The phase increment is constant for  $M$  bits at a time and then increases for the next  $M$  bits. This can be viewed as a phase code approximation to a stepped-frequency waveform having  $M$  steps and  $M$  bits per step (Lewis and Kretschmer, 1986). As a result, the Frank code is less Doppler tolerant than the P3 and P4 codes.

Bandlimiting of the phase-coded waveform prior to matched filtering results in an increase in mainlobe width but a decrease in PSL in codes that have the smallest phase increments in the middle of the codes (Lewis and Kretschmer, 1986; Levanon and Mozeson, 2004). Codes with the largest phase increments near the end exhibit the opposite behavior. Thus, of the three codes shown, the P4 will show the greatest tolerance to precompression bandlimiting in the sense of maintaining or improving its sidelobe level at the matched filter output.

Just as phase codes can be designed based on linear frequency modulation waveforms, they can also be designed based on nonlinear frequency modulation waveforms. A class of codes based on NLFM waveforms designed using the PSP technique mentioned earlier is given in Felhauer (1994). No closed form expression is known for these  $P(n, k)$  codes; they must be found numerically. Typical results are very similar to those for the empirical NLFM waveforms described earlier. The effect of Doppler mismatch is similar to that observed in Fig. 4.39. This is an improvement over conventional polyphase codes, which are prone to exhibiting significantly increased sidelobes near the ends of the code and, in many cases, large spurious peaks well above the general sidelobe level.  $P(n, k)$  codes also exhibit better tolerance to precompression bandlimiting than do codes based on linear FM, since their spectra are already shaped by the basic NLFM design approach. Their chief disadvantage is the difficulty of their design.

Another approach to reducing spectral sidelobes and thus improving precompression bandlimiting tolerance is the use of quadriphase codes. These codes are obtained from biphasic codes by mapping the binary phase progression to a four-phase code using a specified transformation, and also by replacing the rectangular subpulse chips with half-cosine chips of twice the width. Compared to the biphasic code, the resulting codes have significantly lower spectral sidelobes, nearly the same autocorrelation sidelobes, but a significant loss of time (range) resolution. Details are given in Keel and Baden (2012).

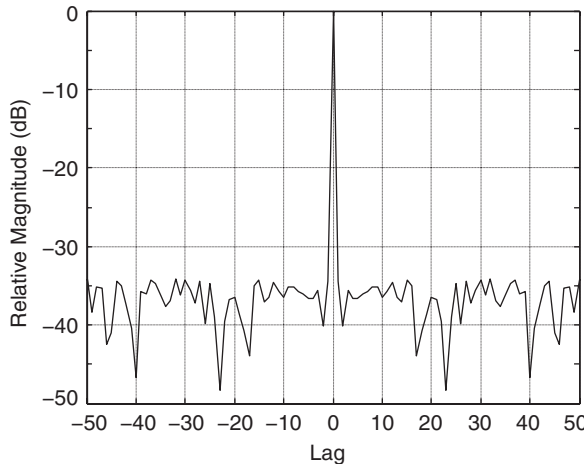


**FIGURE 4.56** Autocorrelation of an  $N = 51$  polyphase Barker code.

*Polyphase Barker codes* are polyphase codes that exhibit a maximum sidelobe peak level of 1. The phases of a length- $N$  code are either unrestricted, or restricted to a  $P$ th root of unity,  $\phi_n = 2\pi p_n/P$  for some integers  $p_n$  and  $P$  and  $n \in [0, N - 1]$ . Figure 4.56 shows the discrete autocorrelation of a polyphase Barker code having  $N = 51$ ,  $P = 50$ , and the following  $\{p_n\}$  sequence:

$$\begin{aligned} &0, 0, 4, 4, 18, 20, 27, 25, 25, 26, 24, 15, 15, 14, 9, 32, 36, \\ &2, 21, 17, 9, 27, 46, 49, 19, 29, 9, 32, 7, 45, 21, 46, 22, 47, \\ &18, 35, 0, 22, 9, 31, 44, 5, 29, 21, 4, 49, 33, 24, 9, 49, 29 \end{aligned}$$

The PSL is  $-34.2$  dB, significantly better than the  $-24.6$  dB for the 51-point MPS code in Table 4.2.

#### 4.10.3 Mismatched Phase Code Filters

The sidelobe structure of phase-coded waveforms can be improved with the use of *mismatched filters*, just as is done with stepped frequency and FM waveforms to improve their sidelobe structures. For phase-coded waveforms, this implies correlating the code sequence with another discrete-time sequence, not necessarily restricted in the amplitudes or phases of its coefficients, such that some metric of the sidelobe structure is optimized. Mismatched filters can be designed to minimize the output PSL, minimize the output integrated sidelobe level (ISL) (sum of the squares of all the sidelobe values of the discrete correlation of the code and filter, divided by the square of the peak), or to shape the output sidelobe response, for instance to enforce particularly low near-in sidelobes at the expense of higher distant sidelobes. The filter order  $L$  is usually larger than the code length. In many cases the design of the mismatched filter coefficients can be formulated as the solution of a weighted least squares problem, for which many numerical algorithms are available. Other optimization techniques, such as  $L^1$  minimization using convex optimization algorithms, can also be employed.

Figure 4.57 illustrates two examples of mismatched filter design. In both cases, the waveform phase code was the same  $N = 64$  MPS biphase code. The peak sidelobe of the matched filter output for this length is 4, giving a PSL in dB of  $20 \log_{10}(4/64) = -24.1$  dB.

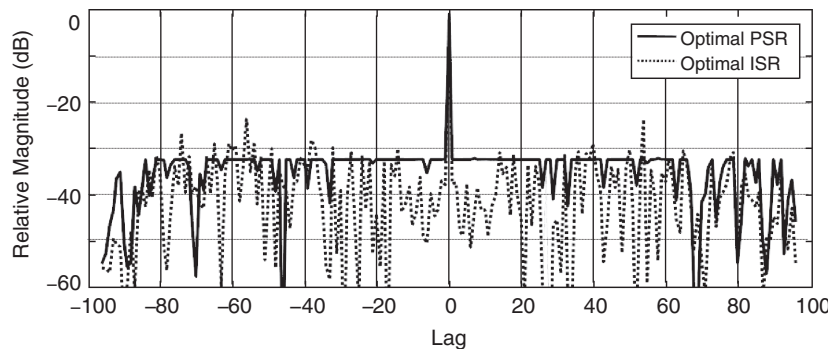


**FIGURE 4.57** Autocorrelation of two  $L = 130$  mismatched filters for the same  $N = 64$  MPS code. Solid line: Optimal PSR filter response. Dotted line: Optimal ISR filter response. (After Keel and Baden, 2012.)

The ISL for the matched filter is  $-6.7$  dB. The solid line in the figure is the result of a mismatched filter of length  $L = 130$  designed to minimize the PSL. The filter impulse response is normalized to have the same energy as the code and its matched filter impulse response, namely 64. This filter achieves a PSL of  $-31.4$  dB, an 8.3 dB improvement compared to the matched filter. The ISL is  $-9.8$  dB, an improvement of about 3.1 dB. However, there is now an LPG of 1.11 dB relative to the matched filter.

The dotted line is the result of an  $L = 130$  filter designed to minimize the ISL and also normalized to an energy of 64. The PSL is now about  $-23.1$  dB, 1 dB worse than the matched filter and 7.3 dB worse than the minimum-PSL filter. However, the ISL is now  $-12$  dB, 5.3 dB better than the matched filter and 2.2 dB better than the minimum-PSL filter. The LPG is 0.85 dB relative to the matched filter, a 0.26 dB improvement compared to the minimum-PSL filter.

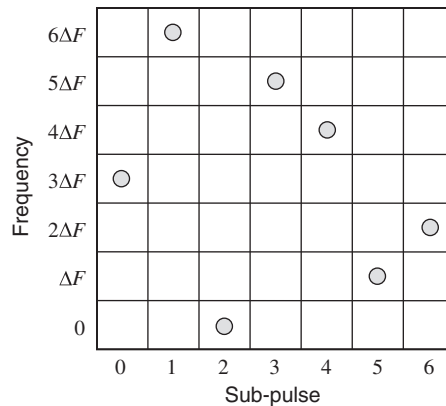
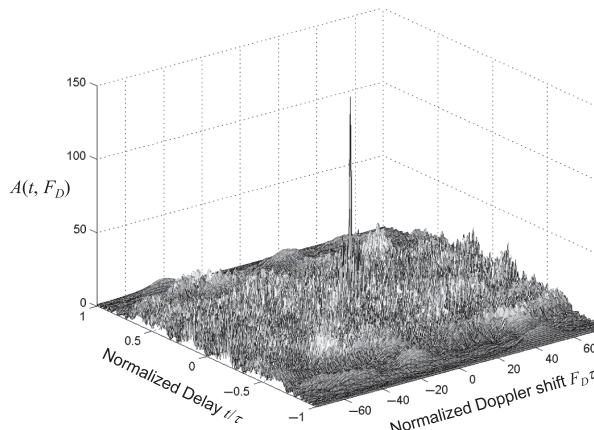
## 4.11 Costas Frequency Codes

*Costas* waveforms are a class of pulse compression waveforms having aspects of both phase-coded and stepped frequency pulse burst waveforms (Costas, 1984). A Costas waveform is similar to a polyphase waveform in that it is a single pulse waveform divided into  $N$  subpulses. It is similar to the linearly stepped frequency waveform in that, rather than maintaining a constant frequency and altering the phase of each subpulse, it alters the subpulse frequencies, stepping through a set of  $N$  frequencies that differ by  $\Delta F$  Hz. Unlike the stepped frequency pulse burst, however, the Costas waveform does not step through the frequencies in linear order. The Costas pulse can be expressed as

$$x(t) = \sum_{n=0}^{N-1} x_n(t - \eta\tau_c) \\ x_n(t) = \begin{cases} \exp(jc[n] \cdot \Delta F \cdot t), & 0 \leq t \leq \tau_c \\ 0, & \text{elsewhere} \end{cases} \quad (4.140)$$

where the sequence  $c[n]$  denotes the ordering of the stepped frequencies.

Figure 4.58 shows the frequency sequence for a typical low-order Costas waveform. With proper design of the frequency step sequence, the Costas waveform can be designed

FIGURE 4.58 Frequency sequence for Costas waveform with  $N = 7$ .FIGURE 4.59 Ambiguity function for a Costas waveform with  $N = 15$ .

to have a more thumbtack-like ambiguity function than the linearly stepped waveform. Figure 4.59 illustrates the ambiguity function of a Costas waveform with  $N = 15$ ; the frequency step sequence was  $c[n] = \{1, 7, 8, 11, 3, 13, 9, 14, 12, 6, 5, 2, 10, 0, 4\}$ . Note the generally low and relatively uniform sidelobe structure throughout the delay-Doppler plane. The construction and properties of Costas waveform are discussed and more examples given in Levanon and Mozeson (2004).

## 4.12 Continuous Wave Radar

All of the preceding discussion in this chapter, and indeed in virtually this entire text, is centered on pulsed radar. Pulsed radars are capable of very long-range application, can easily measure range and velocity, and can achieve fine-resolution imaging. However, pulsed radars require high peak powers in order to achieve good average power and suffer eclipsing and blind zones.

Continuous wave (CW) radar is another class of radar system that transmits and receives continuously. They do not necessarily require as complex a transceiver as does a pulsed system. Because transmission is continuous, the average power equals the peak power, a situation more amenable to the use of solid-state or other peak-power-limited transmit sources. Solid state sources in particular enable the development of very low-cost radar systems. This also means that good average power can be achieved without high peak powers, which is helpful when a low probability of intercept is desired. Eclipsing does not occur, making CW systems superior for short-range measurements. Furthermore, CW systems do not suffer blind zones in range or velocity. Given these characteristics, CW radar is popular for a variety of low-power, short-range applications, especially those involving velocity measurements. Common examples include police and sports "speed guns," radar altimeters and fuzes, missile seekers, meteorology, and automotive cruise control and collision avoidance radar. There are also many more complex or unusual applications such as short-range synthetic aperture imaging, RCS measurements, and storage tank level measurements.

Like pulsed radar, CW radar can be operated with different waveforms, many of them analogous to pulse waveforms. These include constant-frequency, linear and nonlinear FM, biphase and polyphase coding, and frequency coding, as well as techniques less common in pulsed radar such as frequency shift keying (FSK), sinusoidal modulation, and noise modulation. The most common CW waveform is the linear FM, usually called FMCW.

An excellent overview of CW radar configurations, design, waveforms, and applications is available in Piper (2014). A comparative discussion of CW, FMCW, and FSK waveforms in the context of automotive radar is given in Rohling and Kronauge (2012).

## References

- Born, M., and E. Wolf, *Principles of Optics*. Pergamon Press, London, 1959.
- Carrara, W. G., R. S. Goodman, and R. M. Majewski, *Spotlight Synthetic Aperture Radar*. Artech House, Norwood, MA, 1995.
- Cook, C. E., and M. Bernfeld, *Radar Signals: An Introduction to Theory and Application*. Artech House, London, 1993.
- Costas, J. P., "A Study of a Class of Detection Waveforms Having Nearly Ideal Range-Doppler Ambiguity Properties," *Proceedings of the IEEE*, vol. 72(8), pp. 996–1009, Aug. 1984.
- De Witte, E., and H. D. Griffiths, "Improved Ultra-Low Range Sidelobe Pulse Compression Waveform Design," *Electronics Letters*, vol. 40, no. 22, pp. 1448–1450, 2004.
- Felhauer, T., "Design and Analysis of New  $P(n, k)$  Polyphase Pulse Compression Codes," *IEEE Transactions on Aerospace and Electronic Systems*, vol. 30, no. 3, pp. 865–874, Jul. 1994.
- Gini, F., A. De Maio, and L. Patton (eds.), *Waveform Design and Diversity for Advanced Radar Systems*. Institution of Engineering and Technology (IET), London, 2012.
- Jonsson, B. E., "A Survey of A/D Converter Performance Evolution," *Proceedings 17th IEEE Intl. Conf. Electronics, Circuits, and Systems (ICECS)*, pp. 766–769, 2010.
- Kay, S. M., *Fundamentals of Statistical Signal Processing, Vol. II: Detection Theory*. Prentice Hall, Upper Saddle River, NJ, 1998.
- Keel, B. M., "Fundamentals of Pulse Compression Waveforms," Chap. 20 in M. A. Richards, J. A. Scheer, and W. A. Holm (eds.), *Principles of Modern Radar: Basic Principles*. SciTech Publishing, Raleigh, NC, 2010.
- Keel, B. M., and J. M. Baden, "Advanced Pulse Compression Waveform Modulations and Techniques," Chap. 2 in W. L. Melvin and J. A. Scheer (eds.), *Principles of Modern Radar: Advanced Techniques*. SciTech Publishing, Edison, NJ, 2012.
- Levanon, N., "The Periodic Ambiguity Function—Its Validity and Value," *Proceedings 2010 IEEE International Radar Conference*, pp. 204–208, Arlington, VA, 2010.
- Levanon, N., and E. Mozeson, *Radar Signals*. Wiley, New York, 2004.

- Lewis, B. L., F. K. Kretshcmer, Jr., and W. W. Shelton, *Aspects of Radar Signal Processing*. Artech House, Canton, MA, 1986.
- Nathanson, F. E., (with J. P. Reilly and M. N. Cohen), *Radar Design Principles*, 2d ed. McGraw-Hill, New York, 1991.
- Oppenheim, A. V., and R. W. Schafer, *Discrete-Time Signal Processing*, 3rd ed. Pearson, Englewood Cliffs, NJ, 2010.
- Papoulis, A., and S. U. Pillai, *The Fourier Integral and Its Applications*, 6th ed. McGraw-Hill, New York, 2002.
- Peebles, P. Z., Jr., *Radar Principles*. Wiley, New York, 1998.
- Piper, S. O., "Continuous Wave Radar," Chap. 2 in J. A. Scheer and W. L. Melvin (eds.), *Principles of Modern Radar: Radar Applications*. SciTech Publishing. to appear, 2014.
- Price, R., "Chebyshev Low Pulse Compression Sidelobes via a Nonlinear FM," URSI National Radio Science meeting, Seattle, WA, June 18, 1979.
- Raney R. K., "A New and Fundamental Fourier Transform Pair," *Proceedings of the IEEE 12th International Geoscience & Remote Sensing Symposium (IGARSS' 92)*, pp. 26–29, 106–107 May, 1992.
- Richards, M. A., "Time and Frequency Domain Weighting of LFM Pulses," unpublished technical note, Sep. 29, 2006. Available at <http://www.radarisp.com>.
- Rihaczek, A. W., *Principles of High-Resolution Radar*. Artech House, Boston, MA, 1996.
- Rohling, H., and M. Kronauge, "Continuous Waveforms for Automotive Radar Systems," Chap. 7 in F. Gini et al. (eds.), *Waveform Design and Diversity for Advanced Radar Systems*. Institution of Engineering and Technology (IET), London, 2012.

## Problems

1. Consider a stationary radar transmitting a simple square pulse (modulation only, not including the carrier term) of duration  $\tau$ :

$$x(t) = \begin{cases} 1, & 0 \leq t \leq \tau \\ 0, & \text{otherwise} \end{cases}$$

The receiver uses a causal matched filter with  $T_M = \tau$ , so  $h(t) = x^*(\tau - t)$ . The pulse is transmitted with the leading edge being emitted at time  $t = 0$ . An echo is received from a stationary target at a range of  $R$  meters. At what time  $t_{\text{peak}}$  will the peak output of the matched filter be observed? Show all work.

2. Consider the same pulse and matched filter used in the previous problem. Assume that now the target is at range  $R$  meters when the pulse hits it, but is moving with a radial velocity toward the radar of  $k\lambda/2\tau$  m/s, where  $k$  is any integer (except  $k \neq 0$ ). The received signal (again, after the carrier is removed) can be modeled as

$$r(t) = x\left(t - \frac{2R}{c}\right) \exp\left(j2\pi F_D\left(t - \frac{2R}{c}\right)\right)$$

where  $F_D$  is the Doppler shift in hertz. Find the output waveform of the causal matched filter. What is its value at  $t = 2R/c + \tau$  seconds?

3. Suppose the ambiguity function of some waveform  $x(t)$  of duration  $\tau = 1$  millisecond is given by

$$A(t, F_D) = \exp\left\{-\left[\left(\frac{t}{3\tau}\right)^2 + (2F_D\tau)^2\right]\right\}$$

(Note: This is not a possible AF because it is not time-limited to  $\pm\tau$  seconds duration in the delay coordinate, but it will do for this problem.) Suppose there are two targets in the radar's line of sight, one at  $R = 10$  km and one at  $R = 10.1$  km. Also assume that both have the same RCS and ignore the effect of the small range difference on the received echo power. The radar and the first target are stationary. The second target is traveling toward the radar at 100 m/s. The radar is operating at 1 GHz. What is the Doppler shift of the echo from the second target, in hertz? If the matched filter output is sampled at a time delay corresponding to the range to the first target ( $= 2 \times (10 \text{ km})/c = 66.67 \mu\text{s}$ ), the sample will contain contributions from both the first and second targets. Use  $A(t, F_D)$  to determine the relative amplitude of the contribution from the second target compared to that of the first target. Express the answer in dB.

4. Consider a simple pulse burst waveform with  $M = 30$  pulses, each of  $10 \mu\text{s}$  duration, and a PRI of  $T = 100 \mu\text{s}$ . Assuming no weighting functions are used, what are the range resolution, Doppler resolution, unambiguous range, and unambiguous Doppler shift of this waveform?
5. Consider a linear FM waveform that sweeps from 9.5 to 10.5 GHz over a pulse length of  $20 \mu\text{s}$ . What is the bandwidth  $\beta$ ? What is the time-bandwidth product? What will be the Rayleigh resolution (peak to first null) of the matched filter output in meters? What would be the Rayleigh resolution in meters of a square pulse of the same energy (assuming both have the same amplitude)?
6. Continuing with the same LFM waveform as in the previous problem, what will be the frequency in hertz of the first zero of the zero delay cut of the ambiguity function? (This will be the Doppler resolution, or Doppler sensitivity, of the pulse.)
7. Consider an LFM waveform of bandwidth  $\beta = 1 \text{ MHz}$  and pulse length  $\tau = 1 \text{ ms}$ . Suppose an echo is received from a target at a true range of 10 km that is Doppler shifted by 1 kHz. What will be the apparent range of the target, i.e., what will be the range corresponding to the time at which the matched filter output peaks?
8. Consider an LFM pulse with  $\beta = 50 \text{ MHz}$  and  $\tau = 1 \text{ msec}$ . Compute the Doppler shift required to displace the matched filter output by three Rayleigh range resolution cells. No windowing for sidelobe control is used. At 10 GHz, compute the radial velocity associated with that value of Doppler shift. Compute the loss in peak amplitude due to the Doppler shift in dB.
9. Suppose a radar uses a simple rectangular pulse of duration  $\tau$  seconds and processes it through the corresponding matched filter. Assume the matched filter output is sampled at a rate equal to its Rayleigh bandwidth. What is the worst-case straddle loss in dB? Repeat for an LFM waveform with a sufficiently large BT product so that its spectrum is well-approximated by a rectangle of width  $\beta \text{ Hz}$ . Assume no weighting for sidelobe control is used with either waveform.
10. Consider an LFM pulse of duration  $\tau = 1 \text{ ms}$ . Suppose that a range window of only 1.5 km extent is of interest, so it is decided to use stretch processing. The range window is centered on a nominal range of 100 km (think of this as "zooming in" on targets in the vicinity of 100 km). A range resolution of 1.5 meters is required. What is the required bandwidth  $\beta$ ? What will be the  $\beta\tau$  product of the LFM pulse? What will be the bandwidth of the stretch mixer output?
11. Continue with the same scenario and LFM waveform as in the previous problem. Suppose that a beat frequency of 100 kHz is observed at the mixer output. What is the range of the target, relative to the 100 km center of the range window? Ignore any delay in the matched filter.

12. Consider a stationary X-band (10 GHz) radar transmitting a  $\beta = 500$  MHz LFM waveform and using stretch processing in the receiver. The pulse length is  $\tau = 10 \mu\text{s}$ . A radar is often considered “narrowband” if the percentage bandwidth, defined as  $\beta$  divided by the RF frequency, is less than 10 percent; otherwise it is “wideband.” Is this radar narrowband or wideband? What is the expected range resolution in meters?
13. Continuing with the same LFM waveform, suppose a Hamming window is applied to the signal at the output of the stretch mixer, before the FFT is performed. What will be the new value for the expected range resolution, based on the Rayleigh definition of resolution? (*Hint:* The peak-to-null width of the DTFT of a Hamming window of length  $\tau$  seconds is  $2/\tau$  Hz; for a rectangular window it is  $1/\tau$  Hz.) What bandwidth  $\beta$  would be required to achieve 0.3 m resolution if the Hamming window is used to keep the range sidelobes low?
14. Continuing with the same radar and 500 MHz LFM pulse as in the previous two problems, suppose the stretch processor is set up for a nominal range (center of the range window) of  $R_0 = 200$  km and a range window of 300 m ( $200 \text{ km} \pm 150 \text{ m}$ ). However, suppose the reference LFM signal is only  $\tau = 10 \mu\text{s}$  seconds long, i.e., it is not lengthened to allow for signals arriving from the leading or trailing edges of the range window. The reference signal is timed to overlap exactly with the echo from a target at range  $R_0$ . What will be the duration at the mixer output of the beat frequency tone between the echo from a scatterer at the leading edge of the range window ( $200 \text{ km} - 150 \text{ m}$ ) and the LFM reference? Assuming a rectangular window (i.e., no Hamming window), what will be the range resolution at the leading edge of the window?
15. It was stated that range skew at the output of a stretch processor could be corrected with a filter having the frequency response  $H(\Omega) = \exp(-j\Omega^2\tau/2\beta_\Omega)$  where  $\beta_\Omega = 2\pi\beta$  is in radian frequency units. Show that the group delay function  $d_g(\Omega)$  of this filter meets the stated requirement, namely  $d_g(-\beta_\Omega \cdot \delta t_b / \tau) = -\delta t_b$  seconds. Group delay in seconds is defined as  $d_g(\Omega) \equiv -d\Phi(\Omega)/d\Omega$ , where  $\Phi(\Omega) = \arg [H(\Omega)]$ .
16. Assuming a sampling rate of  $F_s$  samples per second at the stretch mixer output, convert the analog frequency response  $H(\Omega)$  of the previous problem to an equivalent discrete-time frequency response  $H(\omega)$ . Also give the expression for  $H(\omega)$  in the particular case when  $F_s$  is chosen to match the stretch mixer output bandwidth of Eq. (4.111).
17. Explicitly compute the loss in processing gain  $LPG$  and the processing loss  $PL$  as a function of  $K$  for a triangular window of odd length  $K + 1$  (so  $K$  is even) defined according to

$$w[k] = \begin{cases} 2k/K, & 0 \leq k \leq K/2 \\ 2 - 2k/K, & K/2 \leq k \leq K \\ 0, & \text{otherwise} \end{cases}$$

Numerically evaluate the result for  $K = 4$  and  $K = 20$  and give the answers in dB. What are the asymptotic values in dB for  $LPG$  and  $PL$  as  $K \rightarrow \infty$ ? The following facts may be useful (be careful about the limits):

$$\sum_{k=1}^n k = n(n+1)/2, \quad \sum_{k=1}^n k^2 = n(n+1)(2n+1)/6$$

(*Hint:* sum just the first half of the triangle, then use symmetry to get the sum of the whole function. Be careful not to double-count any samples.)

18. Consider the array steering factor  $E(\theta_0)$  of Eq. (4.123) and use the weights given in Eq. (4.124) with  $|a_n| = 1$  for all  $n$ . Assume the phases of the weights are computed for a wavelength  $\lambda_0$  and steering angle  $\theta_0$ , but the waveform bandwidth is approximately 10 percent of the nominal frequency so that the effective wavelength varies over the range of  $(1 \pm 0.05)\lambda_0$ . Derive an equation that gives the new angle  $\theta$  at which  $E(\theta)$  will be maximum in terms of  $\lambda_0$ ,  $\theta_0$ , and the actual wavelength  $\lambda$ . When the actual wavelength is 5 percent larger than  $\lambda_0$  and the design steering angle is  $\theta_0 = 10^\circ$ , what will be the actual steering angle (angle of the maximum of  $E(\theta)$ )? Repeat for  $\theta_0 = 30^\circ$  and  $70^\circ$ .
19. Compute the integrated sidelobe ratios for the Barker codes in Table 4.1.
20. Determine the chip length and pulse length of a biphase-coded waveform for a pulsed radar to meet the following requirements:
- Rayleigh range resolution = 0.3 meter.
  - Pulse compression gain > 15 dB.
  - Maximum allowable blind range within first range ambiguity = 50 meters.
  - Less than one-quarter cycle of Doppler phase rotation across the pulse for Doppler shifts up to 2000 Hz.
- One or both parameters may have a range of allowable values. Give the full range if this is the case.
21. Consider Barker, MPS, and pseudorandom biphase codes. State whether each code type can meet the requirements of the previous problem. If not, state the reason; if so, state at least one specific length that will work.
22. Compute explicitly the  $N = 4 = 2^2$  Frank code. What is the sequence of phases  $\phi_n$  in the code (expressed as an angle in radians, e.g., 0,  $\pi/3$ , etc.)? Compute the autocorrelation function of the detected code sequence  $\exp(j\phi_n)$  explicitly by hand. Sketch the magnitude of the autocorrelation function. What is the peak sidelobe level, relative to the peak of the autocorrelation function, in dB?
23. Repeat the previous problem for an  $M = 4$  P4 code. (Be sure to use the complex autocorrelation function.)
24. Equation (4.134) expressed the continuous autocorrelation function  $s_x(t)$  of a phase-coded waveform for  $t = k\tau_c + \eta$  as a linear interpolation between the possibly complex discrete autocorrelation values  $s_A[k]$  and  $s_A[k + 1]$  of the code sequence  $s_A[k]$ . Show that this linear interpolation of the complex values also linearly interpolates the real and imaginary parts of  $s_A[k]$  and  $s_A[k + 1]$ , but that the magnitude of the interpolated value is not the linear interpolation of the magnitudes of  $s_A[k]$  and  $s_A[k + 1]$ .
25. Some waveform/matched filter pairs are more sensitive to Doppler mismatch ("less Doppler tolerant") than others. Consider three different waveforms, all using pulses of length  $\tau$  seconds: a single simple pulse, a single LFM pulse with  $\beta\tau = 1000$ , and a pulse burst composed of 30 simple pulses of length  $\tau$  with a PRI of  $10\tau$  seconds. Denote the time of the peak matched filter output when there is no Doppler shift as  $t_{\max}$ . Suppose a target with a Doppler shift of  $F_D = 1/\tau$  Hz is present. The matched filter does not compensate for this Doppler shift. For each waveform, what will be the magnitude of the matched filter output waveform at  $t = t_{\max}$  compared to the value at  $t_{\max}$  when there is no Doppler shift? Which of these waveforms is most Doppler tolerant in this case? Which is least Doppler tolerant?

